

Construction and Performance of a Triple GEM as Amplification Device for the ND280m TPC Detector at the T2K Experiment

Master Thesis by Nicolas Abgrall
Under the Direction of Prof. Alain Blondel

July 2005 - February 2006



Département de Physique Nucléaire et Corpusculaire
Université de Genève

Abstract

R&D for a GEM based TPC for the ND280m detector at the T2K experiment has been started by the collaboration of the Institutes from Geneva, Barcelona and Bari. A prototype of the amplification device has been designed, developed and constructed. It was operated at CERN and a first performance study has been produced. The preliminary results show that a GEM based TPC would fulfil the T2K physics requirements. This thesis reports the R&D activities of the collaboration and presents the first results.

Acknowledgements

There is a certain number of persons I would like to thank and persons to thank on behalf of the different groups involved in this work.

First I would like to thank Prof. Alain Blondel for giving me the opportunity to work in his group and follow the complete developement of the project, from the building of the detector to the data analysis. Within his group I could get my first experience of experimental particle physics and I learned so much of it. I also thank him for giving quite soon the members of his group, non-negligible responsibility in the management of the projects.

To start with the neutrino group of Geneva, I would like to thank Raphaël Schröter for his support from the beginning and his crucial role in the orientation of my studies. Then I would like to warmly thank Anselmo Cervera for helping me so much in the software part of this master thesis, being so kind and patient. I warmly thank these two friends for sharing so much and making these last eight months a wonderful experience.

From Bari, I would like to thank Emilio Radicioni for sharing so naturally his knowledge with us, his enthusiasm and involvement, and giving me an example to follow in experimental particle physics.

From the group of Barcelona, I would like to express all my gratitude to Thorsten Lux for his reading of this thesis, his advice and kindness. I learned a lot working on his side and I thank him again for making these long days in the control room an experience I will never forget. I would like also to warmly thank Federico Sánchez for his explanations and precious help for the analysis, and keeping the moral of the group so good.

It was a real pleasure for me to work with these people, and I am really proud to be part of this collaboration. I am sincerely grateful for all I learned from them.

On behalf of the collaboration I would like to thank the technical team of Geneva for its involvement and all the work that has been achieved. Another person to thank is Luciano Musa for his precious help and advice concerning the readout electronics.

I had a few lines here to thank all the people that I might have forgotten and that contributed to the achievement of this work. And more particularly, I would like to warmly thank my parents and grand-parents for their support, and Christine for her continuous encouragement.

Finally, the collaboration would like to thank Manora for keeping its doors opened after 10pm even on sunday evenings.

Contents

1	Introduction	1
I	Overview of the T2K Experiment	2
2	Neutrino Oscillation Physics	3
2.1	The Oscillation Phenomena	3
2.2	A Window over new Physics	4
3	Experimental Setup	6
3.1	A Long Baseline Experiment	6
3.2	The ND280m Detector	7
4	Physics Goals	9
II	R&D for a T2K TPC with GEM Readout	10
5	The Time Projection Chamber	11
5.1	Theoretical Background	11
5.1.1	Description	11
5.1.2	Energy Loss of Heavy Charged Particles	12
5.1.3	Physics Measurements	15
5.1.4	Transport of Electrons and Ions in Gases	17
5.1.5	Future Directions for TPCs	19
5.1.6	GEM Foils versus Multi-wire Planes	19
5.2	The HARP TPC	20
5.2.1	Introduction	20
5.2.2	The Field Cage	20
5.2.3	The Magnet	22
5.2.4	The Gas System	23
5.2.5	The Flanges	24
5.2.6	Modifications	26
5.3	The Trigger System	27

6	The GEM Module	29
6.1	The GEM Foils	29
6.1.1	Description	29
6.1.2	Amplification and Transfer Properties	30
6.1.3	Operating GEMs in magnetic fields	35
6.1.4	Advantages of the GEMs	36
6.2	The GEM Tower	37
6.2.1	The Frames of GEMs	37
6.2.2	The Guard Ring	39
6.2.3	The Pad Plane	40
6.2.4	The PCB support	41
6.2.5	The PVC Spacers	41
6.2.6	High Voltage Connections	42
6.2.7	The Gas System	44
6.3	The Electronics	45
6.3.1	The Electronic Modules	45
6.3.2	The Readout	48
6.3.3	The Low Voltage Supply System	49
6.3.4	The Cabling	50
6.3.5	Analogue and Digital Signals Isolation	52
6.3.6	The Grounding	52
6.3.7	The Cooling System	53
6.3.8	Debugging the Electronics	54
7	Building Operations	55
7.1	The GEM Foils	55
7.1.1	Testing Procedures	55
7.1.2	Preparation of the Foils	56
7.2	The Frames	57
7.2.1	Preparation of the Frames	57
7.2.2	High Voltage Test	58
7.3	Glueing Operations	58
7.3.1	Glueing the Pad Plane	58
7.3.2	Glueing the GEM Foils	58
7.3.3	Glueing the Guard Ring	61
7.4	High Voltage Connections	62
7.4.1	Protections	62
7.4.2	Inner Connections	63
7.5	Stacking the Tower	64
7.6	Mounting the Flanges	66
7.6.1	Mounting the Tower on the Detector Flange	66
7.6.2	Mounting the Detector on the HARP Chamber	67
8	Run Conditions	69
8.1	First Run Conditions	69
8.1.1	Gas Choice	69
8.1.2	Measurement Conditions	71
8.1.3	First Results	73
8.2	Second Run Conditions	76

8.2.1	A Solution to Field Distortions	76
8.2.2	Gas Choice	78
8.2.3	Nominal settings	79
8.2.4	Measurements with the Iron Source	80
8.2.5	The Breakdown	80
8.2.6	Improvements of the Testing Procedure	82
8.3	Third Run Conditions	83
8.3.1	General conditions	83
8.3.2	Improvements	83
III	Performance Study	84
9	Overall Framework	85
9.1	The HARP Software	85
9.1.1	The HARP TPC Simulation Software	85
9.1.2	HARP Software and Prototype Simulation	86
9.2	The Data Acquisition System, DAQ	87
9.2.1	Building the DAQ	87
9.2.2	The Detector Monitoring	88
9.2.3	Data Acquisition Operation	89
9.3	The Data Reconstruction	90
9.3.1	The Reconstruction Chain	90
10	Data Analysis	93
10.1	Basic Distributions	93
10.2	Drift Velocity Measurements	94
10.2.1	P5 Measurements	94
10.2.2	$ArCO_2$ Measurements	95
10.3	Tracks Parameters	96
10.4	Charge Attenuation	98
10.5	Analysis	100
10.5.1	Resolution Determination Methods	100
11	Conclusion	111
A	The TPC	113
A.1	The HARP Gas System	113
A.2	Technical Drawings	113
B	The Electronics	122
B.1	Mapping File	122
C	Analysis	125
C.1	The Likelihood Function	125

List of Figures

3.1	View of the long baseline experiment.	6
3.2	Overview of the JPARC facility (Left), the T2K beamline (Right).	7
3.3	Energy spectra for off-axis angle of 2 degrees (black-solid line), 2, 5 degrees (red-dashed line) and 3 degrees (blue-dotted line) (Left), energy spectra and oscillation probability (Right). The blue line shows the overlap for an off-axis angle of 2 degrees.	7
3.4	The ND280 detector design.	8
3.5	The ND280 tracking section design.	8
5.1	Schematic diagram of a time projection chamber.	12
5.2	dE/dX for different particles and materials, [1].	13
5.3	Energy loss distribution of a 1GeV proton in a thin silicon absorber.	14
5.4	$\frac{dE}{dx}$ measurements in the PEP-4 detector, [1].	16
5.5	The HARP experimental area.	20
5.6	HARP TPC field cage zy cross section.	21
5.7	Outer barrel before the assembly (Left), outer barrel with mounted sets of strips (Right).	21
5.8	The set of mylar strips (Left), high voltage connections of the first three inner copper strips (Right).	21
5.9	Magnet of the HARP experiment.	22
5.10	Axial (Left) and radial (Right) components of the magnetic field simulated with TOSCA. The dotted line refers to the position of the downstream end of the chamber. [2]	23
5.11	Gas regulation system (Left), Gas distribution (Right).	24
5.12	Extraction and support structure of the chamber.	25
5.13	Transport operation of the chamber.	25
5.14	Dismantling the HARP flange (Left), fixing the adaptative ring (Right).	26
5.15	Set of scintillators on top of the chamber (Left), positioning of the scintillators (Right).	27
5.16	Trigger system in the control room.	28
6.1	A GEM foil typical geometry (Left), the double-conical geometry (Right).	30
6.2	Typical triple GEM setup.	30
6.3	Fields and currents setup.	32
6.4	The ratio X/C for different hole diameters and shape (Left), simulation of the extraction and collection efficiencies for several GEM voltages (Right).	33

6.5	Electric field strength in GEM hole for different voltages and external fields (Left), simulated C and X efficiencies compared to their parametrisations (Right).	33
6.6	Measured extraction efficiency for electrons compared to simulation (Left), measured collection efficiency for electrons compared to simulation (Right).	34
6.7	Measured primary and secondary extraction efficiency for ions compared to simulation (Left), measured collection efficiency for ions compared to simulation (Right).	34
6.8	Garfield simulation of drift lines in a GEM hole in a 4 T magnetic field.	35
6.9	Anode current versus magnetic field.	36
6.10	Effective gain for single, double and triple GEM structure.	36
6.11	Charge amplification (Left), respective signals on the pads (Right).	37
6.12	Ion feedback and electron transparency as functions of the drift field.	37
6.13	Frame (Left) and GEM foil (Right) for the COMPASS experiment.	38
6.14	Schematic diagramme of a frame.	38
6.15	Cathode face of a frame (Left), anode face of a frame (Middle), detail of the service area of the anode face (Right).	38
6.16	Frame layer (Left), detail of the junction (Right).	39
6.17	Frame with spacers conceptual design (Left), GEM foil glued on a frame with spacers (Right).	39
6.18	Copper coated cathode face of the guard ring.	40
6.19	Schematic side view of the pad plane.	40
6.20	Pad plane view (Left), pad side (Middle) and connector side (Right) drawings.	41
6.21	Pad plane and first GEM layer mounted on the PCB support (Left), view of the connector side (Right).	42
6.22	The GEM tower mounted on the PVC spacer (grey frame).	42
6.23	The High Voltage Box fixed on the magnet (Left), connections to the detector (Right).	43
6.24	Complete gas distribution on the readout (Left) and cathode (Right) sides of the chamber.	44
6.25	Complete gas distribution (Right), gas inlets for the upper GEM module (Left).	45
6.26	Protection card (Left), and its schematic (Right).	45
6.27	Inverter card.	46
6.28	Front End Card.	46
6.29	The PASA response function (Left), the ALTRO chip block diagramme (Right).	47
6.30	Front-end electronics basic components.	47
6.31	Schematic side view of the electronic module.	48
6.32	USB to FEC interface.	49
6.33	Termination card.	49
6.34	The low power supply system.	50
6.35	Inverters connected via a connector chain (Left), and via voltage distribution bars (Right).	51
6.36	Complete cabling of the detector.	51
6.37	Connections to the digital ground.	53
6.38	Ground connections of the electronic modules.	53
6.39	Pump of the cooling system (Left), cooling pipes (Right).	54
7.1	Global view of the clean room (Left), laminar flux (Middle), dry boxes used to store the GEMs (Right).	56
7.2	High voltage test bench.	56

7.3	The frame is placed on the luminous table (Left), adjustment of the foil on the aluminum frame (Right).	59
7.4	The GEM foil is stretched on the aluminum frame (Left), setting marks on the foil for the alignment (Right).	59
7.5	The roller is passed many times in the glue (Left), the glue is spread on the frame with the roller (Right).	60
7.6	Alignment and glueing of the GEM foil on the frame (Left), a roller is used to provide a uniform glueing (Right).	60
7.7	The GEM is let for drying with weights on the aluminum frame.	61
7.8	Detail of the glueing seen with the microscope. A few traces of glue can be seen on the very edge of the inactive area.	61
7.9	Test of the GEM glued on its frame (Left), storage in dry boxes (Right).	62
7.10	Spreading glue on the guard ring (Left), drying with weights (Right).	62
7.11	Cutting the kapton foil (Left), guard ring after the glueing (Right).	63
7.12	Soldering protection resistors.	63
7.13	Cutting of the kapton foil (Left), placing and glueing the copper strip (Middle), soldering the high voltage cable on the strips (Right).	64
7.14	Testing the high voltage contacts (Left), the two-part conductive glue (Right).	64
7.15	Pad plane and PCB support (Left), first GEM placed on the pad plane (Right).	65
7.16	First layer on the pad plane (Left), piling up (Right).	65
7.17	Second layer (Left) and complete stack (Right).	65
7.18	Testing the tower (Left), test of the tower with the guard ring (Right).	66
7.19	The tower is fixed on the detector flange.	66
7.20	Complete stacking of the detector.	67
7.21	Transporting the detector to CERN.	67
7.22	HARP chamber with the endcap (Left), the field cage (Middle), fixation of the detector flange (Right).	68
7.23	The high voltage connectors (Left), checking gas leakages with the sniffer (Right).	68
8.1	Drift velocity in $[\text{cm}/\mu\text{s}]$ (Left) and transverse diffusion in $[\mu\text{m}/\sqrt{\text{cm}}]$ vs the electric field at 0.2 T for different mixtures of ArCO_2 [3].	69
8.2	Drift velocity in $[\text{cm}/\mu\text{s}]$ (Left) and transverse diffusion in $[\mu\text{m}/\sqrt{\text{cm}}]$ vs the electric field for P5 at 0.2 T.	70
8.3	Transverse diffusion in $[\mu\text{m}/\sqrt{\text{cm}}]$ vs the electric field for P5 at 0.2 T.	70
8.4	Nominal geometrical setting.	71
8.5	Field distortions in the xy plane.	74
8.6	S-shaped tracks in the xy plane (Left), C-shaped tracks in the z direction (Right).	74
8.7	Potential (Left) and electric field simulations (Right).	75
8.8	Potential simulations adding a new reference plane (Left). Detail of the simulation (Right).	76
8.9	The shield (Left) and its support structure fixed on the detector flange (Right).	77
8.10	Top view of the tower with the shield (Left), GEMs are protected before transport to CERN (Right).	77
8.11	Drift velocity in $[\text{cm}/\mu\text{s}]$ (Left) and transverse diffusion in $[\mu\text{m}/\sqrt{\text{cm}}]$ (Right) vs electric field for ArCO_2 (90 : 10) at 0.2 T.	78
8.12	Longitudinal and transverse diffusion in $[\mu\text{m}/\sqrt{\text{cm}}]$ vs electric field at 0 T for ArCO_2 (90 : 10).	78
8.13	The suspicious GEM on the left sector of the pad plane (Left), test of the GEM in the test bench (Right).	80

8.14	View of the anode face of the GEM with the microscope (Left), detail (Right).	81
8.15	Pad plane without GEMs (Left), detail of a damaged pad (Right).	81
8.16	Protection resistors in the high voltage box.	83
8.17	The external edge of the shield insulated.	83
9.1	Schematic overview of the HARP software.	86
9.2	Schematic diagram of the HARP simulation chain.	87
9.3	The zero-suppression scheme. The glitch filter and number of pre- and post-samples are set in the <i>equipementlist_TEST.c</i> file.	88
9.4	Schematic overview of the detector monitoring.	89
9.5	Different views of the new implemented geometry of the readout plane in the HARP TPC.	91
10.1	Mean RMS per channel on board 0 (Left) and board 14 (Right). The channels without signals are grounded channels.	94
10.2	Typical pulses in a two pad cluster (Left), saturation of the signal in an event with high ionisation.	94
10.3	Number of hits per pad for the lower sector of the prototype over the run 1369.	94
10.4	Particle showers resulting possibly from the interaction of a proton in the iron yoke of the magnet.	95
10.5	Side view of the chamber with a double-track event (Left), front view with the emission of a δ -electron (Middle), front view with the visible signal of the iron source in the middle of the pad plane (Right).	95
10.6	ADC counts distribution in time for different boards.	96
10.7	Energy spectrum of the iron source from the P5 measurements.	96
10.8	z distribution of the clusters with a 75 μ s delay (Left) and a 85 μ s delay of the trigger.	97
10.9	Distributions of the number of clusters per track (Left), number of hits per cluster (Middle) and total charge per track (Right).	97
10.10	Tracks distributions for the θ (Left) and ϕ (Middle) angles. χ^2 distribution (Right).	98
10.11	Ratio between the numbers of 2 pad clusters and 1 pad clusters as a function of the drift distance.	98
10.12	Total charge as a function of the drift distance.	99
10.13	Attenuation in mm (Left) and charge at zero drift (Right) as functions of the run number.	99
10.14	The centroid position does not reflect the true position of the charge cloud.	100
10.15	Correction function of the reconstructed centroid position for different values of σ .	101
10.16	Correction function for every z (Left), residuals over a pad width after the correction (Right).	102
10.17	Resolution as a function of z for runs 1362 to 1369 (Left) and runs 1517 to 1538 (Right). In red is the 1 pad cluster resolution, in black the 2 pad cluster resolution and the line is the RMS for the 2 pad cluster resolution.	102
10.18	The charge per pad is fitted for 2 pad and 3 pad clusters configurations.	103
10.19	Residual distributions for three different values of the sigma of the charge cloud between 300 and 400 mm.	103
10.20	Residual distributions for three different values of the sigma of the charge cloud between 500 and 600 mm.	104
10.21	x resolution (mm) vs the sigma of the charge cloud for two different z-slices: 100 to 200 mm (Left) and 300 to 400 mm (Right).	104

10.22x resolution vs the sigma of the charge cloud for two different z-slices: 500 to 600 mm (Left) and 700 to 800 mm (Right).	104
10.23Cluster width (mm) as a function of the drift distance.	105
10.24Residual distributions after the centroids correction for clusters between 300 and 400 mm (Left), 400 and 500 mm (Middle) and 500 and 600 mm (Right).	106
10.25Residuals over a pad width before (Left) and after (Right) correction of the centroids.	106
10.26x resolution as a function of the drift distance.	107
10.27The square of the charge cloud width as a function of the drift distance as it is obtained from the likelihood fit. The mean values come from the gaussian fit and are fitted with a second order polynomial. Runs 1362 to 1399 (Left), 1517 to 1538 (Middle) and 1592 to 1640 (Right).	109
10.282 pad cluster resolution obtained with the PRF method (black) and the likelihood method (red). For both cases, the geometric mean of the fitted sigma to the residuals is shown for runs 1362 to 1399 (Left), 1517 to 1538 (Middle) and 1592 to 1640 (Right).	109
10.291 pad cluster resolution obtained with the PRF method (black) and the likelihood method (red). For both cases, the geometric mean of the fitted sigma to the residuals is shown for runs 1362 to 1399 (Left), 1517 to 1538 (Middle) and 1592 to 1640 (Right).	109
10.303 pad cluster resolution obtained with the PRF method (black) and the likelihood method (red). For both cases, the geometric mean of the fitted sigma to the residuals is shown for runs 1362 to 1399 (Left), 1517 to 1538 (Middle) and 1592 to 1640 (Right).	110
A.1 HARP gas system. In black is represented the system used for the prototype.	114
A.2 Interface flange.	115
A.3 PCB reinforcement.	116
A.4 PCB drilling map.	117
A.5 Guard ring design.	118
A.6 Module of 2 frames.	119
A.7 Tetraboard.	120
A.8 Complete stacking.	121
B.1 Mapping file.	123

List of Tables

5.1	Excitation and ionisation characteristics of various gases.	15
5.2	Operating channels and voltages of the photo-multipliers.	27
6.1	Channels and respective outputs.	43
8.1	Nominal voltage setting in <i>Data taking</i> working point for P5.	72
8.2	Nominal fields setting in <i>Data taking</i> working point for P5.	72
8.3	Nominal voltage setting in <i>Pedestal run</i> working point for P5.	73
8.4	Nominal fields setting in <i>Pedestal run</i> working point for P5.	73
8.5	Nominal voltage setting in <i>Data taking</i> working point for $ArCO_2$	79
8.6	Nominal fields setting in <i>Data taking</i> working point for $ArCO_2$	79
8.7	Nominal voltage setting in <i>Pedestal run</i> working point for $ArCO_2$	79
8.8	Nominal fields setting in <i>Pedestal run</i> working point for $ArCO_2$	80

Chapter 1

Introduction

This master thesis reports the common R&D work of the groups of the Département de Physique Nucléaire et Corpusculaire of the University of Geneva, the Institut de Física d'Altes Energies, Universitat Autònoma de Barcelona and the INFN (Bari), concerning the use of a triple GEM structure as amplification device for TPC of the ND280m detector at the T2K experiment. This work was mainly undertaken at CERN, using the previous facilities of the HARP experiment in parallel sessions with the groups of Dapnia, CEA-Saclay, performing similar studies for the Micromegas option. The first part of this thesis gives a short overview of the T2K long baseline experiment and of the various interests in the study of neutrino physics. The second part is a complete review of the R&D activities: first a brief description of the Time Projection Chamber is given, followed by a detailed presentation of the GEM module and the building of the prototype. Finally the different run conditions are summarised. The third part of the thesis is dedicated to the data analysis and to the presentation of the performance obtained with the prototype. The conclusion finally summarises the aims of this R&D work and stresses out the possibility for a GEM based TPC at the ND280m detector.

Part I

Overview of the T2K Experiment

Chapter 2

Neutrino Oscillation Physics

2.1 The Oscillation Phenomena

Neutrino oscillations can be described in a quite straightforward way, when considering a model in which the weak eigenstates of the neutrinos ν_l are defined as a mixture of the mass eigenstates ν_i :

$$|\nu_l\rangle = \sum_i U_{li} |\nu_i\rangle \quad (2.1)$$

where U_{li} is called the Maki-Nakagawa-Sakata-Pontecorvo (MNSP) mixing matrix, and can be written in the case of three Dirac neutrinos, as:

$$U_{ij} = \begin{pmatrix} 1 & 0 & 0 \\ 0 & c_{23} & s_{23} \\ 0 & -s_{23} & c_{23} \end{pmatrix} \begin{pmatrix} c_{13} & 0 & s_{13}e^{i\delta} \\ 0 & 1 & 0 \\ -s_{13}e^{-i\delta} & 0 & c_{13} \end{pmatrix} \begin{pmatrix} c_{12} & s_{12} & 0 \\ -s_{12} & c_{12} & 0 \\ 0 & 0 & 1 \end{pmatrix}$$

where, $c_{ij} = \cos\theta_{ij}$, $s_{ij} = \sin\theta_{ij}$, and where the angles θ_{ij} parametrise the three possible rotations between the neutrino states. Then, during the propagation of a ν_l state created in a weak interaction process, if the masses of the ν_i states are different, they will acquire a relative phase difference. The decomposition of their superposition back to the ν_l states may then result in the appearance of a different flavour than the initial one. This phenomenon is commonly called *neutrino oscillations*. In the case where only two of the mass states dominate the oscillations in vacuum, we find the usual formula that governs the appearance of one flavour (i.e. ν_e) in an initially pure beam of another flavour (i.e. ν_μ) is given by [4]:

$$P(\nu_\mu \rightarrow \nu_e) = \sin^2 2\theta \sin^2\left(\frac{1.27 \Delta m^2 L}{E}\right) \quad (2.2)$$

where θ is the angle contributing to the mixing, L is the distance from the source to the detector, E is the energy of the neutrino, and $\Delta m^2 = m_j^2 - m_i^2$. The numerical constant is valid for L given in [km], E in [GeV] and Δm^2 in [eV^2]. Taking the results from solar neutrinos plus KamLAND data together with the results from Super-Kamiokande constrains the values of two of the mixing angles from the MNSP matrix (θ_{12} and θ_{23}), the value and the sign of Δm_{12}^2 , and the value of Δm_{23}^2 . There are then still three undetermined parameters in the MNSP matrix: the angle θ_{13} , the sign of Δm_{23}^2 and the value of the CP-violating phase δ .

The current knowledge of neutrino oscillations shows a strong domination of the two oscillations

measured with solar and atmospheric neutrinos. From constraints given by other experiments, the angle θ_{13} is already known to be small, and thus, the determination of this parameter should be related to small corrections of the main oscillations. A clear understanding of these sub-dominant effects requires to go beyond the 2-neutrino formula and investigate the formula taking into account the complete 3-neutrino mixing matrix:

$$\begin{aligned}
P(\nu_\mu \rightarrow \nu_e) = & 4C_{13}^2 S_{13}^2 S_{23}^2 \Phi_{31} \times (1 + \frac{2a}{\Delta m_{31}^2} (1 - 2S_{13}^2)) \\
& + 8C_{13}^2 S_{12} S_{13} S_{23} (C_{12} C_{23} \cos\delta - S_{12} S_{13} S_{23}) \cos\Phi_{32} \sin\Phi_{31} \sin\Phi_{21} \\
& - 8C_{13}^2 C_{12} C_{23} S_{12} S_{13} S_{23} \sin\delta \sin\Phi_{32} \sin\Phi_{31} \sin\Phi_{21} \\
& + 4S_{12}^2 C_{13}^2 (C_{12}^2 C_{23}^2 + S_{12}^2 S_{23}^2 S_{13}^2 - 2C_{12} C_{23} S_{12} S_{23} S_{13} \cos\delta) \sin^2\Phi_{21} \\
& - 8C_{13}^2 S_{13}^2 S_{23}^2 (1 - 2S_{13}^2) \frac{aL}{4E_\nu} \cos\Phi_{32} \sin\Phi_{31}
\end{aligned} \tag{2.3}$$

where $\Phi_{ij} = \Delta m_{ij}^2 L / 4E$. Though quite complex, this expression is an approximation where the matter effects (coming through the parameter a) are calculated in the case of a constant density. It contains the three unknown parameters θ_{13} , the sign of Δm_{23}^2 (through a) and the CP-violating phase δ . The constraints on the oscillation parameters given by other experiments also allow to write an approximative form:

$$\begin{aligned}
P(\nu_\mu \rightarrow \nu_e) \approx & \sin^2 2\theta_{13} \sin^2 2\theta_{23} \sin^2 \Delta \\
& \pm \alpha \sin 2\theta_{13} \sin \delta \cos \theta_{13} \sin 2\theta_{12} \sin 2\theta_{23} \sin^3 \Delta \\
& - \alpha \sin 2\theta_{13} \cos \delta \cos \theta_{13} \sin 2\theta_{12} \sin 2\theta_{23} \cos \Delta \sin 2\Delta \\
& + \alpha^2 \cos^2 \theta_{23} \sin^2 2\theta_{12} \sin^2 \Delta
\end{aligned} \tag{2.4}$$

where $\alpha = \Delta m_{21}^2 / \Delta m_{31}^2$ and $\Delta = \Delta m_{31}^2 L / 4E$.

2.2 A Window over new Physics

The standard model predicts massless neutrinos, making them essentially different from the other fermions such as the charged leptons and the quarks, that are known to be massive. Many popular scenarios of physics beyond the standard model were closely related to the masslessness of the neutrino. Actually, from a theoretical point of view, the masslessness of the neutrino is not satisfactory: the standard model does not really predict massless neutrinos, it is built in such a way that it does, since no right handed neutrino field (ν_R) is introduced in the fermion content. But actually, there is no fundamental reason, no symmetry principle to rely on for doing it this way.

One of the major aim of particle physics is unification of the fundamental interactions, and this provides extra motivations for massive neutrinos, since many models predict neutrino mass at some level. For example, the supersymmetrised standard model naturally predicts massive neutrinos, unless a lepton number symmetry is artificially imposed on it.

Once we know that the neutrinos are massive, another fundamental theoretical question is to understand the smallness of this mass compared to the masses of the charged fermions even in a single family. A good theory of neutrino mass should also throw some light on this point. Another question concerning the neutrino mass is its fundamental nature, that is whether neutrinos are Dirac or Majorana particles.

Neutrinos are opening a wide range of questions and neutrino oscillations are still to be clearly understood and investigated. For example, another possible consequence of neutrino mixing is that the mixing matrix could also be complex, and this would imply CP-violating phenomena in the leptonic sector as well.

Chapter 3

Experimental Setup

3.1 A Long Baseline Experiment

The T2K long baseline experiment is based on adding a beamline to redirect the proton beam from the 50 GeV synchrotron (initially limited to 40 GeV) currently under construction at the new JPARC facility in Tokai, Japan, in order to produce an intense neutrino beam.



Figure 3.1: View of the long baseline experiment.

The JPARC proton beam is a high power beam of 0,75 MW in phase I (4 MW expected in phase II in 2015), that will produce the most intense neutrino beam ever built. The neutrino beam will be characterised by a set of detectors located 280 m from the pion production target, and then propagate underground for 295 km to the Super Kamiokande detector, which will distinguish ν_e and ν_μ in the neutrino beam by observing the Cherenkov radiation from μ 's and e 's produced by charged current interactions in its 50 kton water target.

The design of the T2K facility is based on the fact that the neutrino beam will be directed in such a way that it actually misses the Super Kamiokande detector. This configuration results in a considerable improvement in the quality of the beam for the ν_e appearance experiment.

As the off-axis angle increases, the energy peak narrows and moves lower in energy. By selecting the correct angle, this narrow peak can be near on the maximum oscillation probability at the far detector (see Figure 3.3).

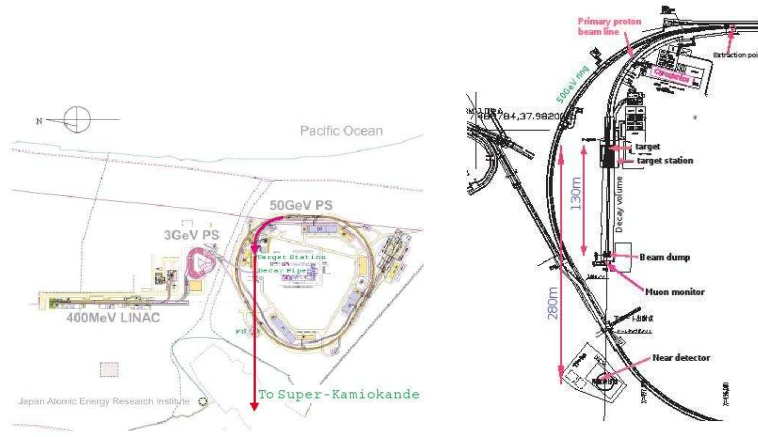


Figure 3.2: Overview of the JPARC facility (Left), the T2K beamline (Right).

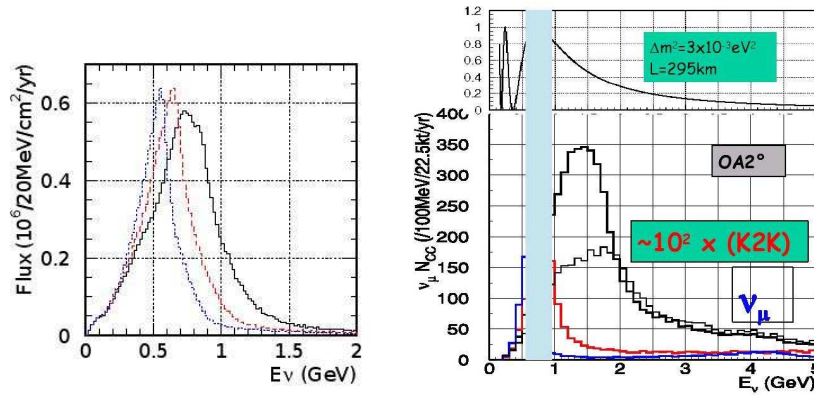


Figure 3.3: Energy spectra for off-axis angle of 2 degrees (black-solid line), 2, 5 degrees (red-dashed line) and 3 degrees (blue-dotted line) (Left), energy spectra and oscillation probability (Right). The blue line shows the overlap for an off-axis angle of 2 degrees.

3.2 The ND280m Detector

The near detector should consist in a few scintillators and tracking sections, preceded along the beamline by a dedicated neutral pion detector (see Figure 3.4). The thick scintillators will serve as target and proton tag, the tracking section will measure the muons and pions and the neutral pion detector will track converted photons.

The tracking section will mainly consists in three successive TPCs, with Fine Grained Detector (FGD) modules inserted in between, as shown in Figure 3.5. This master thesis is dedicated to the study of the readout plane of these TPCs.

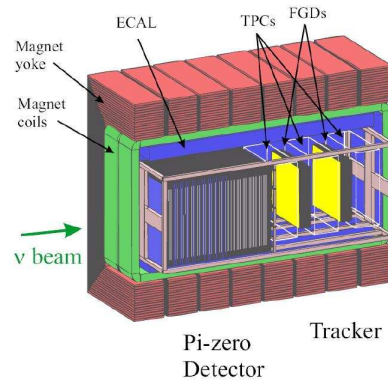


Figure 3.4: The ND280 detector design.

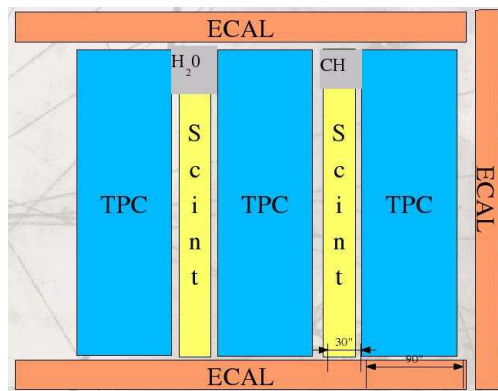


Figure 3.5: The ND280 tracking section design.

Chapter 4

Physics Goals

The main physics goals of the T2K experiment are:

- A precision measurement of the neutrino oscillation parameters ($\sin^2 2\theta_{23}$, Δm_{23}^2) by observing $\nu_\mu \rightarrow \nu_x$ disappearance.
- The determination of $\sin^2 2\theta_{13}$ by the measurement of the $\nu_\mu \rightarrow \nu_e$ appearance signal.
- Confirmation of $\nu_\mu \rightarrow \nu_\tau$ by the measurement of neutral current events.

For these goals to be successfully achieved, the ND280m detector should provide precise informations on the neutrino spectrum and intensity for the SK flux prediction. These informations mainly consist in:

- Understanding of the basic background processes for the oscillation measurements, that is, charged background for ν_μ disappearance, neutral background for ν_e appearance and intrinsic ν_e contamination of the beam.
- Understanding of neutrino-nucleus interactions, including nuclear reinteractions.
- Giving an absolute normalisation and neutrino energy flux shape for SK flux prediction, and an absolute normalisation for electron neutrinos and neutral current π^0 .

Part II

R&D for a T2K TPC with GEM Readout

Chapter 5

The Time Projection Chamber

5.1 Theoretical Background

5.1.1 Description

A Time Projection Chamber (TPC) provides a complete three-dimensional picture of the ionisation deposited in a gas (or liquid) volume by a traversing charged particle. The TPC's 3D localisation makes it the most powerful tracking system for charged particles in a high track density environment, and its high ability for ionisation energy loss measurements makes it one of the most efficient identification system.

The TPC was invented by Dave Nygren at the Lawrence Berkeley Laboratory in the late 1970s. The first major application of the TPC was in the PEP-4 detector which studied 29 GeV e^+e^- collisions at the PEP storage ring at SLAC. Then TPCs have been used mainly to study e^+e^- collisions (PEP, TRISTAN collider, KEK laboratory, LEP), and also in a certain number of experiments involving heavy ions collisions (RHIC) or even in non-accelerator experiments (ICARUS). Here we give a rough description of a standard TPC, using the example of a typical geometry. The TPC makes use of ideas of both the Multi-Wire Proportional Chamber (MWPC) and drift chamber. The detector is essentially a large gas-filled cylinder with a thin high voltage electrode at the center (sometimes also placed at the end of the chamber like in the HARP TPC). When voltage is applied, a uniform electric field directed along the axis of the chamber is created thus making the free ionisation electrons drift towards the endcaps. Those ones are covered by sector arrays of proportional anode wires arranged as shown in Figure 5.1. A cathode strip cut up into rectangular segments called *pads* is placed parallel to each wire. This system of wires and pads provides the position of a space point projected onto the endcap plane, where one coordinate is given by the position of the firing anode wire while the second is obtained from the signals induced on the row of cathode pads along the wire (center of gravity method). The third coordinate along the cylinder axis is given by the drift time of the ionisation electrons. This method yields many space points for each track allowing a full reconstruction of the particle trajectory. The problem of transverse (and longitudinal) diffusion due to relatively long drift distances in the chamber is remedied by applying also a magnetic field parallel to the electric field, thereby confining the electrons to helical trajectories around the drift direction.

The ions created in the avalanches during amplification tend to drift back towards the cathode, possibly yielding to space charges in the drift volume and thus to distortions of the electric field. This problem is prevented by placing a wire grid at ground potential just before the anode wires, thereby capturing the ions backflow.

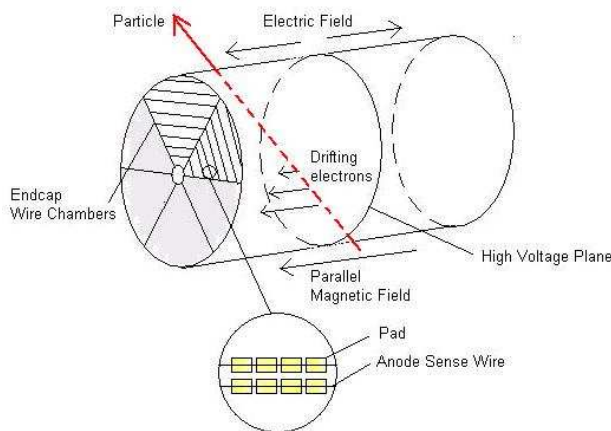


Figure 5.1: Schematic diagram of a time projection chamber.

The particle identification ability of the TPC is evidently related to the resolution in the $\frac{dE}{dx}$ measurement that can be obtained. For this point, many different factors have to be considered requiring careful thought, e.g., wire gain variations in position and time, calibration of the wires, saturation effects, choice of gas and operating pressure, attachment of electrons, etc.

5.1.2 Energy Loss of Heavy Charged Particles

Average Energy Loss per Unit Path Length, dE/dx

The inelastic collisions with the atomic electrons of the material are almost solely responsible for the energy loss of heavy particle in matter. Elastic scattering from nuclei can also contribute but only in the case where the mass of the incident particle is not negligible compared to the mass of the nuclei (i.e. α particles). Other processes such as Cherenkov radiation or Bremsstrahlung are mostly negligible compared to the collisional energy loss (Bremsstrahlung is moreover negligible for particles heavier than the electron).

The inelastic collisions are statistical in nature, but their number per macroscopic length is usually large and the fluctuations in the total energy loss are small. This enables to work with the average energy loss per unit path length, or simply called dE/dx . The *Bethe-Bloch formula*, derived from quantum mechanics, is the basic expression used for energy loss calculations:

$$-\frac{dE}{dx} = 2\pi N_a r_e^2 m_e c^2 \rho \frac{Z}{A} \frac{z^2}{\beta^2} \left[\ln\left(\frac{2m_e \gamma^2 v^2 W_{max}}{I^2}\right) - 2\beta^2 - \delta - 2\frac{C}{Z} \right] \quad (5.1)$$

where r_e and m_e are the classical radius and mass of the electron, I is the mean excitation potential, Z and A are the atomic number and weight of the absorbing material, ρ is the density of the absorbing material, z is the charge of the incident particle in units of e , δ is the *density effect* correction at high energy, C is the *shell* correction at low energy, and W_{max} is the maximum energy transfer in a single collision, which is given by the kinematics (head-on collision) for an incident particle of mass M :

$$W_{max} = \frac{2m_e c^2 \eta^2}{1 + 2s\sqrt{1 + \eta^2} + s^2} \quad (5.2)$$

where $s = \frac{m_e}{M}$ and $\eta = \beta\gamma$. This expression is simplified as $W_{max} \approx 2m_e c^2 \eta^2$ when $M \gg m_e$. It is common to introduce the reduce length $X = \rho x$ to express the dE/dx in units of mass thickness:

$$\frac{dE}{dX} = \frac{1}{\rho} \frac{dE}{dx} \quad (5.3)$$

The dE/dX appears to be roughly independent of the material type. Actually, for not too different Z, the ratio Z/A varies little and the dependence of I in Z (which has been empirically) does not matter a lot, since it appears in the logarithm.

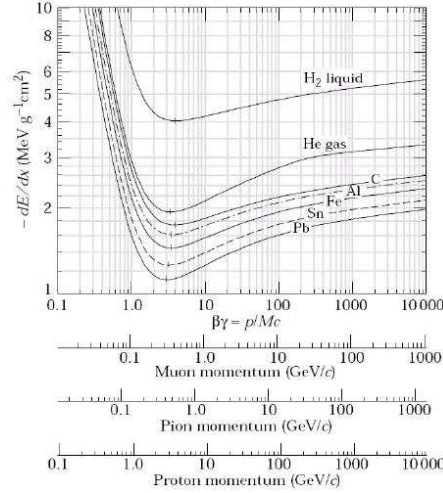


Figure 5.2: dE/dX for different particles and materials, [1].

The energy dependance of the $\frac{dE}{dx}$ is such that the minimum value is almost the same for all particles of the same charge. As the energy increases beyond this point, the term $\frac{1}{\beta^2}$ becomes almost constant and the rise due to the logarithmic dependance is cancelled by the density correction, thus reaching the *Fermi plateau* (see Figure 5.2).

Energy Loss Distribution

For relatively thick absorbers where the number of collisions is large, the energy loss distribution is shown to be gaussian in form:

$$f(x, \Delta) \propto \exp\left(-\frac{(\Delta - \bar{\Delta})^2}{2\sigma^2}\right) \quad (5.4)$$

where x is the thickness of the absorber, Δ is the energy loss in the absorber and $\bar{\Delta}$ is the mean energy loss. The standard deviation has been calculated by Bohr for non-relativistic particles:

$$\sigma_0^2 = 4\pi N_A r_e^2 (m_e c^2)^2 \rho \frac{Z}{A} x \quad (5.5)$$

and is extended to relativistic particles by:

$$\sigma^2 = \frac{(1 - \frac{1}{2}\beta^2)}{1 - \beta^2} \sigma_0^2 \quad (5.6)$$

In the case of gases (or thin absorbers in general), where the number of collisions is small, the distribution becomes complicated to calculate, especially because of the possibility of large energy transfer in a single collision. These type of events, though rare, are sufficiently probable to add a long tail to the high energy side of the distribution. The mean energy loss is then slightly displaced and no longer coincide with the most probable energy loss (see Figure 5.3).

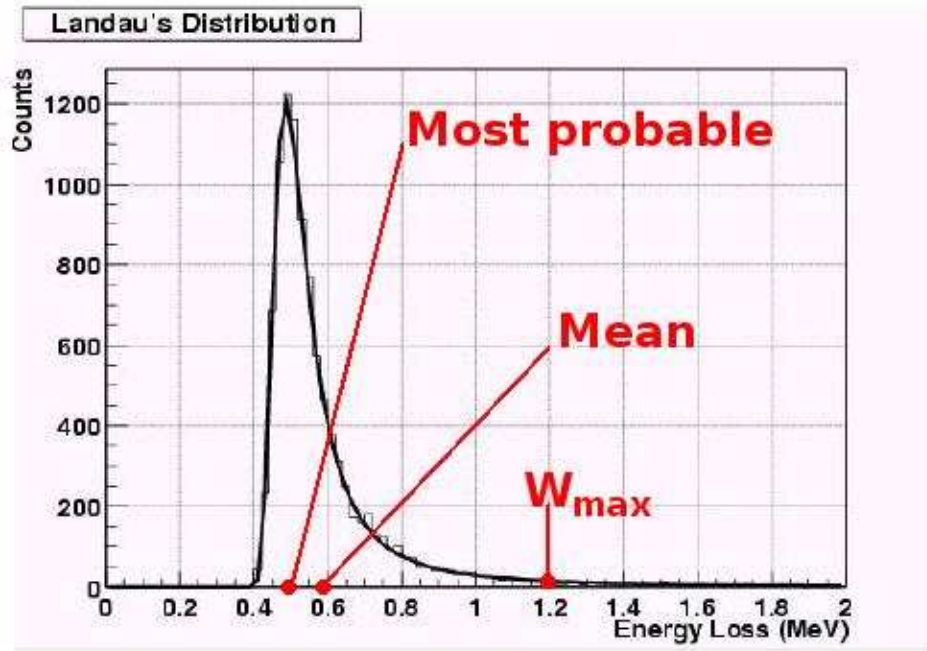


Figure 5.3: Energy loss distribution of a 1 GeV proton in a thin silicon absorber.

Basic theoretical calculations of this distribution have been performed by Landau, Symon and Vavilov, and can be found in more detail in [5].

Mean Number of Ionisations

The statistical nature of the ionisation reactions allows to define the average number of electron-ion pairs created for a given energy loss. It should be pointed out that this value is not simply the total energy loss divided by the ionisation potential of the medium, since excitations also contribute to the energy loss of the particle. In the case of gases, it turns out to be in the order of 1 electron-ion pair per 30 eV of lost energy (100 electron-ion pairs for a 3 keV particle), and does not seem to be strongly dependent of the particle and gas types (see Table 5.1.2).

For a deposited energy, E , one would expect on the average $J = E/w$ ionisations and the Poisson statistics of ionisation and excitation would then give the variance as $\sigma^2 = J$. The energy resolution would then be given by :

$$\frac{\sigma_E}{E} \propto 2.35 \frac{\sqrt{J}}{J} = 2.35 \sqrt{\frac{w}{E}} \quad (5.7)$$

the 2.35 coming from the fact that σ_E is taken at the FWHM of the distribution. In the case where the full energy of the radiation is absorbed in the detector, the energy deposited is a fixed

Gas	Excitation potential [eV]	Ionisation potential [eV]	Mean energy, w , for ion-electron pair creation [eV]
H_2	10.8	15.4	37
N_2	8.1	15.5	35
O_2	7.9	12.2	31
Ne	16.6	21.6	36
CO_2	10.0	13.7	33
Ar	11.6	15.8	26
CH_4		13.1	28

Table 5.1: Excitation and ionisation characteristics of various gases.

value, and Poisson statistics is not applicable anymore. Instead, Fano showed that $\sigma^2 = FJ$, where F is known as the *Fano factor*, and is an intrinsic constant of the medium taking into account the various processes of energy transfer in the detector. Thus, for example, for a 5,9keV photon coming from a ^{55}Fe source in Argon ($w = 26eV$ and $F = 0,2$) the theoretical energy would be given by:

$$\frac{\sigma_E}{E} \approx 2,35 \sqrt{\frac{Fw}{E}} \approx 0,069 \quad (5.8)$$

5.1.3 Physics Measurements

Tracking and Identification of Particles

- The 3D tracking is made by the precise spatial localisation of the deposited ionisation charges in the drift volume. The localisation in the xy plane is provided by the location of the pads on which a signal is measured and the localisation in the z direction, along the axis of the chamber, is provided by the time information and the measurement of the drift velocity.
- The identification of the particles is provided by the ionisation energy loss measurements. For energies below the minimum ionising value ($v \approx 0.96c$), each particle exhibits a $\frac{dE}{dx}$ curve which, in most cases, is distinct from the other particle types. This is the characteristic exploited for identifying particles in this energy range. The usual way is to plot the $\frac{dE}{dx}$ of the particle as a function of its momentum. An example of $\frac{dE}{dx}$ measurements in the PEP-4 detector is shown in Figure 5.4.

Spatial and Momentum Resolutions

The determination of the particle momentum is provided via the parameters of a helical fit to the reconstructed tracks, which are curved in the drift volume under the influence of the magnetic field in the z direction. The radius of curvature and the momentum component perpendicular to \vec{B} are related by:

$$pcos\lambda = 0,3zBR \quad (5.9)$$

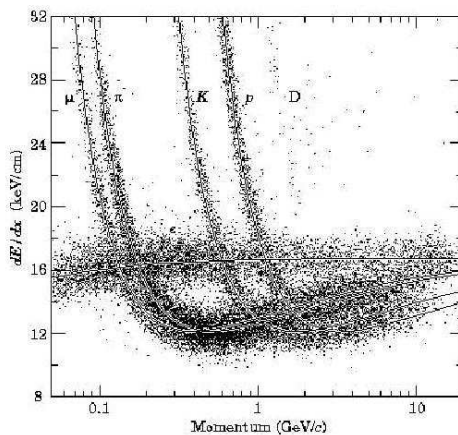


Figure 5.4: $\frac{dE}{dx}$ measurements in the PEP-4 detector, [1].

where λ is the pitch angle, z is the charge of the incident particle in units of e , B is in Tesla, R is in meters and p is in GeV/c . The curvature is defined as $k = \frac{1}{R}$ and its distribution is approximately gaussian. The curvature error for a large number of uniformly spaced measurements on the trajectory of a charged particle in a uniform magnetic field, can be approximated by:

$$(\delta k)^2 = (\delta k_{res})^2 + (\delta k_{ms})^2 \quad (5.10)$$

where δk_{res} is the curvature error due to finite measurement resolution, and δk_{ms} is the multiple scattering contribution given by:

$$\delta k_{ms} \approx \frac{(0,016)(GeV/c)z}{Lp\beta\cos^2\lambda} \sqrt{\frac{L}{X_0}} \quad (5.11)$$

where L is the total track length, and X_0 is the radiation length of the scattering medium in units of length (see [1]).

If many (≥ 10) uniformly spaced position measurements are made along the trajectory, then:

$$\delta k_{res} = \frac{\epsilon}{L'^2} \sqrt{\frac{720}{N+4}} \quad (5.12)$$

where N is the number of points measured along the track, L' is the projected length of the track onto the bending plane and ϵ is the measurement error for each point, perpendicular to the trajectory. This can also be formulated in a relative way as :

$$\frac{\delta k_{res}}{k} = \frac{p\cos\lambda}{0,3zB} \frac{\epsilon}{L'^2} \sqrt{\frac{270}{N+4}} \quad (5.13)$$

The momentum resolution is thus directly dependent of the spatial resolution. The latter can be determined through the *residuals method*, which will be further explained in the *Data Analysis* section of the second part of this thesis. The spatial resolution depends on many different factors such as geometrical factors (e.g. pads size, drift distance) and gas properties (diffusion coefficient and attachment of charges). Neglecting the terms related to pad-to-track angle effects (not relevant for square pads in first approximation), the position resolution in TPCs can usually be expressed as:

$$\sigma^2 = \sigma_0^2 + D \cdot \frac{L_d}{N_{el}^{tot}} \quad (5.14)$$

where D is the diffusion coefficient, L_d is the drift length and N_{el}^{tot} is the number of primary ionisation electrons along the track collected on a pad. σ_0^2 is the intrinsic resolution of the detector measured in the region close to the pad plane. This term is dominated by the charge sharing (pad size vs charge spread) and by the signal to noise ratio (determined by the gas gain and the noise of the electronics).

5.1.4 Transport of Electrons and Ions in Gases

Electrons and Ions Diffusion

In the absence of an electric field, the electrons and ions liberated by a passing radiation, diffuse uniformly outward from their point of creation. They come quickly in thermal equilibrium with the gas because of the multiple collisions they undergo with the gas molecules or atoms. The velocities of the charges are then described by the Maxwell distribution which gives a speed of:

$$v = \sqrt{\frac{8kT}{\pi m}} \quad (5.15)$$

where k is the Boltzmann's constant, T the temperature and m the mass of the particle. This expression shows why electrons are much faster than ions (10^6 cm/s at room temperature). The linear distribution of charges after a time of diffusion t, is given by a gaussian:

$$\frac{dN}{dx} = \frac{N_0}{\sqrt{4\pi Dt}} \exp\left(\frac{-x^2}{4Dt}\right) \quad (5.16)$$

where N_0 is the total number of charges, x is the distance from the point of creation and D is the diffusion coefficient of the gas. The RMS spread in x is then given by $\sigma_x = \sqrt{2Dt}$. The diffusion coefficient can be calculated from kinetic theory and is shown to be $D = \frac{1}{3}v\lambda$, where λ is the mean free path of the electron or ion in the gas. For a classical ideal gas:

$$\lambda = \frac{1}{\sqrt{2}} \frac{kT}{\sigma_0 p} \quad (5.17)$$

where p is the pressure of the gas and σ_0 is the collision total cross section with a gas molecule or atom.

Drift of Charges in an External Electric Field

In the presence of an electric field, electrons and ions are accelerated along the field lines towards the anode and cathode respectively. The average velocity attained by the charges, called the *drift velocity*, u, is a dynamical equilibrium between the acceleration due to the drift field and the stopping due to the collisions with the gas atoms. It is useful to define the *mobility* of a charge as $\mu = \frac{u}{E}$.

For positive ions, the drift velocity is found to depend linearly on the ratio E/p, up to relatively high electric fields. For ideal gases where the moving charges remain in thermal equilibrium, the mobility is related to the diffusion coefficient by the Einstein relation:

$$\frac{D}{\mu} = \frac{kT}{e} \quad (5.18)$$

The diffusion in x is then given by:

$$\sigma(x) = \sqrt{2Dt} = \sqrt{\frac{2kT}{eE}}x \quad (5.19)$$

The mobility for electrons is much greater and is found to be a function of E (mostly because of the *Ramsauer effect*). The gain in velocity of the electrons can affect the diffusion rate if the mean energy of the electrons exceeds thermal energies. The factor kT in the Einstein relation is then replaced by this mean energy and this increases the diffusion coefficient. Thus, to get a small σ_x at high drift fields, small electron energies are required. In pure Argon, for example, a field of 1 V/cm already produces electron energies larger than the thermal energy; this is why Argon is called *hot gas*. On the contrary, in CO_2 , which is called *cold gas*, this behaviour occurs at fields of 2 kV/cm.

Influence of a Magnetic Field

The drift of electrons will be modified when a magnetic field is added to the electric field. In the TPC, the magnetic and electric fields are parallel. When the electron trajectory is deviated from the electric field lines direction because of a collision with a gas atom, the trajectory will be constrained on an helix around the straight previous trajectory. The projection of the trajectory onto the plane perpendicular to the fields then becomes a circle, and the mean free path projection ($D = \frac{1}{3}v\lambda$) is therefore smaller than the value without a magnetic field. As the magnetic field does not modify the longitudinal component, the projection of the trajectory along the field lines is not affected. The main result of these observations is that the longitudinal diffusion is independent of the magnetic field, whereas the transverse diffusion is reduced according to:

$$\frac{D_T(\omega)}{D_T(0)} = \frac{1}{1 + \omega^2\tau^2} \quad (5.20)$$

where $\omega = (eB)/m$ is the cyclotron frequency and τ is the microscopic average time between collisions ($\vec{u} = (e\vec{E}/m)\tau$), which can be related to the total collision cross-section with the gas atoms.

Electron Attachement

It is important that the ion-electron pairs created through ionisation, remain in a free state long enough in order to be collected. Two processes can hinder this requirement: recombination and electron attachement. Recombination of ion-electron pairs is not important in the case of the TPC, since it is predominant in the absence of an external electric field. Electron attachement involves the presence of electronegative atoms to form negative ions according to:



These are atoms that have an almost full outer electron shell, so that the addition of an extra electron actually results in the release of energy. Well known electronegative gases are, for example, O_2 , CO_2 , CCl_4 and SF_6 . On the contrary, noble gases have negative electron affinities. As far as water is concerned, it increases the effect of oxygen if it is present at the same time. The quantitative effect of a fraction, p , of electronegative atoms in the gas can be described as an attenuation of charges:

$$n(x) = n_0 e^{-\frac{x}{\lambda_c}} \quad (5.22)$$

where n is the number of electrons from an initial cloud of n_0 electrons at the distance x from the creation point, and λ_c is the mean free path for the electron capture:

$$\lambda_c = \sqrt{\frac{m_e}{2E}} \frac{u}{N h p \sigma(E)} \quad (5.23)$$

where $N = (\rho N_A)/A$ is the number of gas molecules per unit volume, and h is the attachment probability, and $\sigma(E)$ is the electron capture cross section.

5.1.5 Future Directions for TPCs

The time projection chamber has developed into a mature technology that is used in many fields. Over the past 25 years, the TPC, constantly following the progress of its inner technologies, has proven to be an extremely adaptive tool, which is a necessary quality in an ever-changing work environment.

Since only a few years, major technological developments concerning the electron amplification appeared in gaseous TPCs. Two new technologies issued of the successful development of Micro Pattern Gas Detectors (MPGD) could now play the role of wire chambers: the Gas Electron Multipliers (GEM) and the Micromesh Gaseous structure chambers (Micromegas). Both GEMs and Micromegas have a somewhat lower gain than wire chambers but in the case of the GEMs, two or three layers of them can easily be cascaded by placing the foils on top of each other, thereby multiplying the gains.

These two technologies are just starting to replace wire chambers in some experiments (COMPASS) and are still mainly in R&D for future detectors such as the near detector (ND280m) of the T2K experiment.

5.1.6 GEM Foils versus Multi-wire Planes

A conventional TPC using a multi-wire plane for charge amplification is limited by $\vec{E} \times \vec{B}$ effects in the region close to the wires. In the case of measurements with strong magnetic fields, this leads to a broadening of the charge cloud and a worsening of the resolution.

The wires are intrinsically defining a preferred direction and the reconstructed hits location is thus dependent of the projected angle between the track and the wires.

Another problem worth mentioning in these conventional TPCs is that the readout is done by the detection of induced signals and not by the drifting charges themselves. These signals are much slower and broader and this limits the granularity of the TPC as well as the double track resolution.

In the case of the GEMs, this problem does not occur, since the pads directly detect the electron cloud which results in a fast and narrow charge signal. Moreover, the slow ion tail is cut off since the ion cloud does not reach the induction region.

By construction, a GEM foil does not show a preferred direction of amplification and thus, any $\vec{E} \times \vec{B}$ effects would be isotropic. This effect is anyway considerably reduced for GEMs since the hole pitch is around 0.140 mm compared to the 2 mm pitch between wires.

Finally, the fact that very different electric fields can be set in front and behind the GEM is largely suppressing the back drift of ions produced in the GEM holes, especially in the drift volume. This property seems advantageous with respect to the use of an additional gating grid.

5.2 The HARP TPC

5.2.1 Introduction

The Hardware part of this master took place mainly at CERN in the experimental hall of the HARP experiment (Figure 5.5), which was dismantled at the beginning of the year 2003. The HARP TPC was approximately designed in the same way as we described in the previous section. The high voltage cathode was situated at the end of the chamber and MWPCs were placed above a complete pad plane divided in six sectors of 662 pads each. Some facilities remained at our disposal and the prototype was mounted on the HARP TPC via some modifications of the set up.



Figure 5.5: The HARP experimental area.

This part is not intended to be a complete description of the HARP TPC which is already well documented in the literature (MWPCs, pad plane, electronics, etc). We focused our attention on the main relevant elements for the operating of the detector.

5.2.2 The Field Cage

The Cage Design

The complete structure of the field cage is directly mounted on the inner surface of the outer stesalite barrel of the TPC. This barrel is a cylinder of inner and outer diameters of 800 mm and 820 mm respectively, and 2010 mm length. The electric field inside the drift volume is defined by the high voltage applied between the endcap cathode and the anode (GEMs + shield) and by three sets of circular strips mounted on the barrel as shown in Figure 5.6.

A kapton foil, coated with 10 mm wide copper strips separated by a step of ≈ 3 mm on both sides and fixed on the inner surface of the barrel, constitutes the first two sets of strips with an offset of half a period.

The third set is constituted of 11 mm wide aluminised mylar strips separated by a step of 1 mm and mounted on the inner surface of the barrel via 24 rods, called *baguettes*, glued on the surface with araldit. This set has an offset of half a period with respect to the set of copper strips which has direct view in the chamber.

The rods have two functions: they are the mechanical support of the mylar strips and the central one plays the role of a voltage divider. Actually, an appropriate circuit printed on the rod, together with a resistors chain, delivers the high voltage to the different sets, thereby fixing

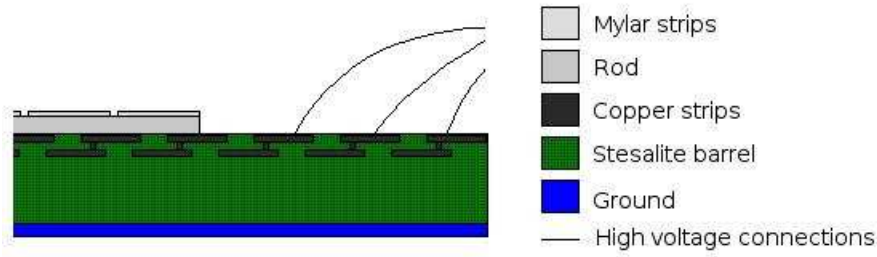


Figure 5.6: HARP TPC field cage zy cross section.

the potential of each strip. Details of the configuration of the sets are shown in Figure 5.7 and Figure 5.8.

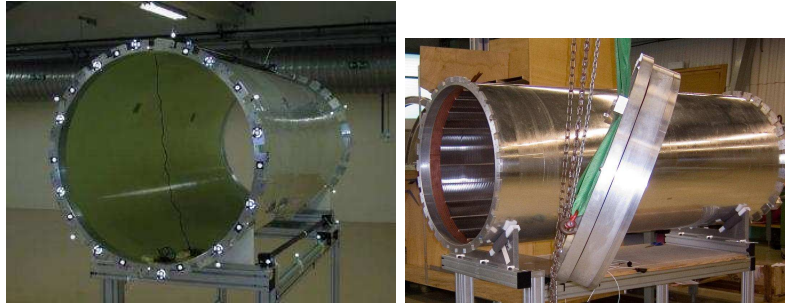


Figure 5.7: Outer barrel before the assembly (Left), outer barrel with mounted sets of strips (Right).



Figure 5.8: The set of mylar strips (Left), high voltage connections of the first three inner copper strips (Right).

The set of mylar strips fixes the axial field in the chamber whereas the inner and outer copper

sets provide field uniformity near the barrel inner surface and avoid field ejection ¹ respectively.

The High Voltage Supply System

The voltage which defines the field in the chamber is delivered by two different power supplies. The first one is directly connected to the endcap cathode and delivers a voltage of 25 kV for approximately 300 μA , which are then divided among the sets of strips (the upper limit of the power supply is 30 kV and was restricted to 25 kV to avoid any permanent damage of the field cage). A second power supply is connected to the last three copper strips with respect to the anode plane, and delivers a voltage of 3 kV. In this configuration, the sum of the two currents should be around 430 μA . The second power supply is necessary to define correctly the potentials near the anode plane and avoid field distortions. This point is more detailed in the subsection 5.2.6.

5.2.3 The Magnet

The field cage is inserted in a solenoid magnet of 900 mm diameter and 2250 mm length, shown in Figure 5.9. The magnet itself consists of a set of solenoid copper coils surrounding an iron return yoke. A maximal magnetic field of 0.7 T can be reached, providing a current of 889 A to the coils.



Figure 5.9: Magnet of the HARP experiment.

The chamber of the TPC is 1500 mm long, that is 750 mm shorter than the magnet; this geometry and an iron endcap closing the magnet at the readout plane side, provide the homogeneity of the axial magnetic field with a ratio $\frac{B_T}{B_L} < 1\%$ at 0.7 T. Figure 5.10 shows a Monte Carlo simulation of the axial and radial components of the field as a function of the position along the axis of the solenoid and for different distances from the central axis.

The magnet is equipped with a water cooling system, which consists basically in a set of cold water pipes surrounding the coils.

¹Due to the proximity of conductive surfaces in the detector or in the chamber, the fringe field of the cylinder can eventually cause ionisation in the gas, thus yielding to sparks or field distortions.

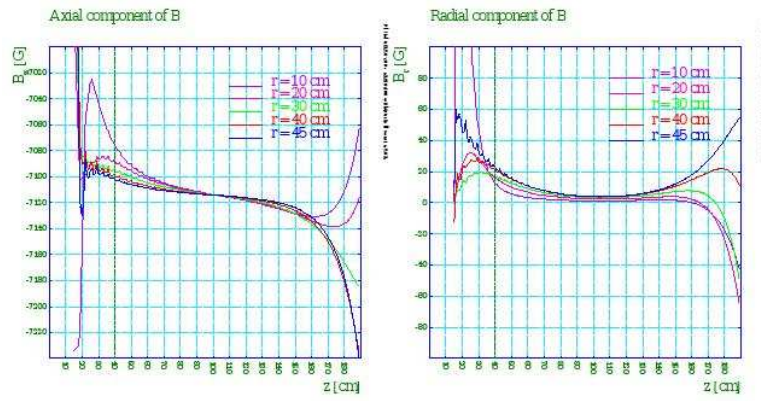


Figure 5.10: Axial (Left) and radial (Right) components of the magnetic field simulated with TOSCA. The dotted line refers to the position of the downstream end of the chamber. [2]

5.2.4 The Gas System

The Gas Distribution

The gas system is schematically constituted of three different parts: the gas source, the flow regulation and the chamber. The gas source is usually a bottle of 150 bars directly connected to the entrance of the system.

The flow regulation starts immediately after the source with a set of two pressure regulators that make the pressure drop from 150 bars to 500 mbars overpressure, which is the expected value at the beginning of the system. A flow regulator then sets the flow in the chamber up to 60 L/h. A set of gates is used to bypass the chamber thereby enabling the purge of the drift volume towards the exhaust during the change of the gas bottles.

The chamber itself has a volume of 750 L and has to be completely filled at least three times which represents a day and a half with the previous setting. Then, depending on the choice of the gas, two to five more days are necessary to get a good homogeneity in the chamber and minimise oxygen and other gases contaminations. Before the entrance of the chamber is a safety bubbler which automatically regulates the pressure below a threshold of +10 mbars overpressure. At the end of the exhaust line of the chamber is another bubbler which enables to see directly whether the chamber is under overpressure or not. This bubbler and the chamber are bypassed after the change of a gas bottle during a few minutes.

A set of Is and Ts and 6 mm diameter pipes are used to make the gas flow in the chamber via two connections on the HARP flange and two connections to the exhaust on the cathode plane. A complete description of the gas system is given in Appendix A and partly described in Figure 5.11.

The Gas Tightness

One of the main problem in gaseous TPCs is the absorption of primary charges due to the presence of oxygen in the drift volume. The gas tightness is thus a crucial point for this kind of detectors, and one has to avoid all the possible sources of gas leakages. Concerning the gas distribution of the chamber, two points have to be carefully checked: the pipes connections and the connections of the mechanical pieces themselves. Gas leakages and their intensity can be detected with a gas sniffer.

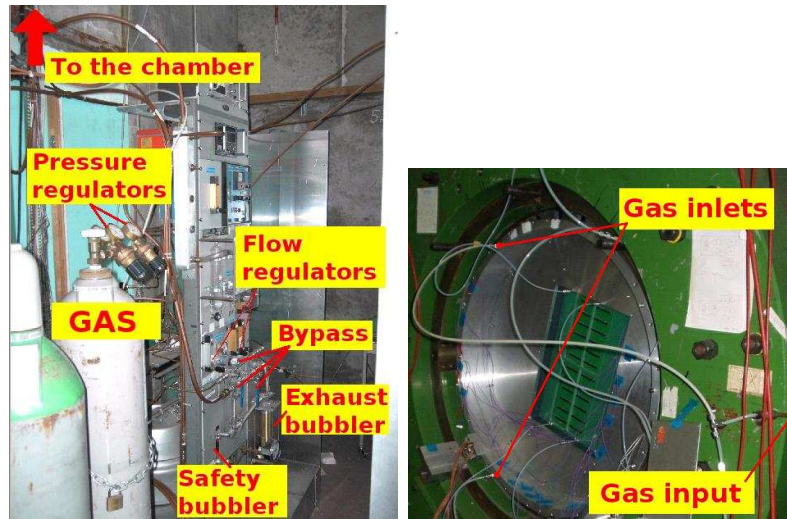


Figure 5.11: Gas regulation system (Left), Gas distribution (Right).

For the first point, CERN standard gas connectors are used. These are a type of one-way connections where the tightness is mechanically achieved when screwing the system. Moreover, teflon tape is winded round the threads when the connectors have to be screwed on the HARP flange.

For the tightness between the mechanical pieces of the detector, o-rings and vacuum grease are used. The o-rings, covered with grease, are pressed between the pieces when the latter are screwed together.

The presence of a hole in the HARP flange, enabling the passage of high voltage wires to the first copper strips, also requires attention and gas tightness is obtained by the use of silicon paste.

A final point to take care of, is that under operating conditions, nothing is pressing on the chamber and could eventually create a little space for oxygen contamination.

5.2.5 The Flanges

On the anode side of the chamber, a set of three aluminum flanges is supporting the detector.

- The *HARP flange* is the external ring which is directly mounted on the stesalite barrel of the chamber. This is the only flange which has direct connections with the inside of the chamber: the two gas entries and one hole enabling the passage of high voltage wires to the first copper strips.
- An *Adaptative flange* is needed to fix the detector on the chamber. It is another ring with two circular grooves where 4 mm diameter o-rings are placed (see Figure 5.14). The ring is screwed from inside on the HARP flange in such a way that one o-ring is facing the latter and the other one is facing the *Detector flange* which is to be screwed from outside on the ring. To mount the adaptative ring, the chamber has been extracted from the magnet and transported in a clean room where the HARP flange could be dismantled under proper conditions (see Figure 5.12).

The stesalite barrel of the chamber weights around 200 kg; needless is to say that these transport operations are very delicate and require a lot of care and attention while handling

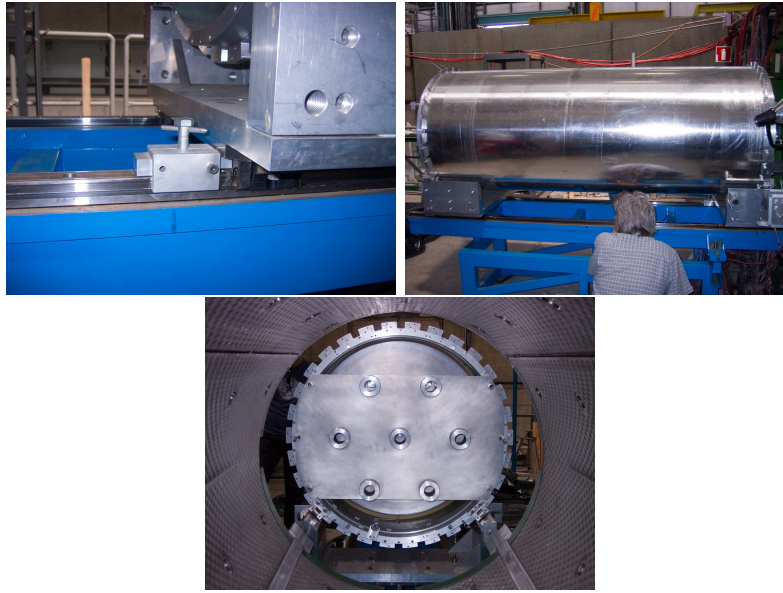


Figure 5.12: Extraction and support structure of the chamber.

the chamber with a crane.



Figure 5.13: Transport operation of the chamber.

- The Detector flange has a 800 mm diameter and a rectangular apperture centered in the vertical position but translated of 210 mm in the horizontal position in order to have the sensitive part of the detector centered in the chamber. All along the apperture is a groove

to lodge an o-ring for the gas tightness with the detector.



Figure 5.14: Dismantling the HARP flange (Left), fixing the adaptative ring (Right).

- An aluminum endcap has been manufactured to close the chamber during the opening operations (see Figure 7.22). A more detailed description of the flanges can be found in Appendix A.

5.2.6 Modifications

- The first modification dealt with the compatibility of the mechanical support of the detector and of the chamber itself. The detector can not be mounted directly because of the HARP flange which supported the previous readout structure. The adaptative flange was then designed as an intermediate step between the two flanges.
- The second modification was applied to the field cage. The mechanical support of the detector is designed in such a way that the guard ring of the GEMs tower arrives at the level of the middle of the second mylar strip in the chamber once the detector flange is mounted. High voltage wires were then soldered on the first three copper strips in order to equalise the potentials of the guard ring and the respective mylar strip to get electric field uniformity. The solder was then covered with blue tape (or a kind of varnish) to avoid sparks with other pieces of the detector close to the strips. The wires are then passed through a hole in the HARP flange and connected to the high voltage box.
- A resistive chain between these last strips was then added in the high voltage box in order to extend the voltage divider and thus degrading the potentials in a more proper way over the short distance (approximately 50 mm) between the anode plane and the detector ground (flange). This resistive chain also prevents a too high current backflow in power supply of the strips.
- The gas distribution system of the chamber was modified to incorporate another bypass system and the gas distribution of the GEMs. Actually, an Oxysorb cartridge is mounted on the gas system before the chamber. It can eventually be used after changing a gas

bottle, when flushing the chamber for the first hours to avoid oxygen introduction. The disadvantage of this method is that the gas flow is then dropping to 15 to 25 L/h, but in case the gas quality is fine, one should permanently run with it.

5.3 The Trigger System

The trigger system of the chamber is composed of 7 scintillators, coming both from Geneva (S2, S4, S6) and Saclay (A, B, P1, P2): 3 are placed on top of the magnet and 4 below as shown in Figure 5.15. All are wrapped in a thick black fabric to minimise the light contamination. The upper scintillators are placed in such a way that two of them are covering the first part of the chamber and the last one is centered on the cathode plane, whereas the lower scintillators are covering almost the whole chamber. This configuration was chosen to allow the drift velocity measurement by observing tracks crossing the endplate cathode.

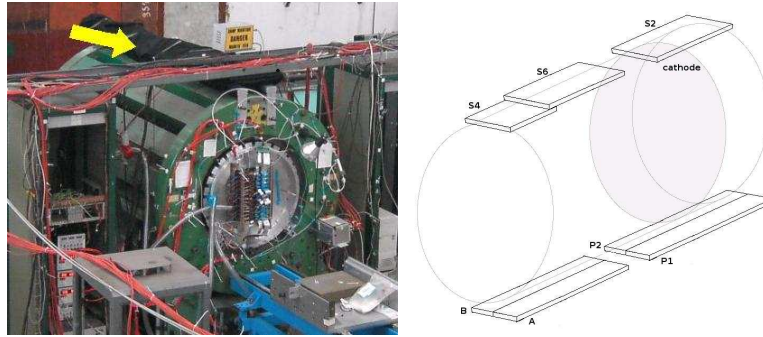


Figure 5.15: Set of scintillators on top of the chamber (Left), positioning of the scintillators (Right).

The voltage for the photo-multipliers is delivered by a standard CAEN Mod. SY127 (40 channel HV system) equipped with modules Mod. A431 which can deliver 8 kV for 200 μ A. The operating voltages are given in Table 5.3.

PM	Channel	Voltage [V]
P1	0	1950
P2	2	1900
A	3	2070
B	7	2200
S2	8	2600
S6	9	2400
S4	10	2600

Table 5.2: Operating channels and voltages of the photo-multipliers.

The logic circuit (see Figure 5.16) uses NIM standard logic units such as discriminators (with fixed threshold and width), fan-out units to split the signals between the scalers and the rest of the logic, fan-in units that sum the signals for bottom and top scintillators (or a predefined set of scintillators when triggering just on half of the chamber for example), a fast coincidence unit

and a time unit to delay the overall trigger when needed. For electronic tests, the trigger was generated by a NIM clock module.

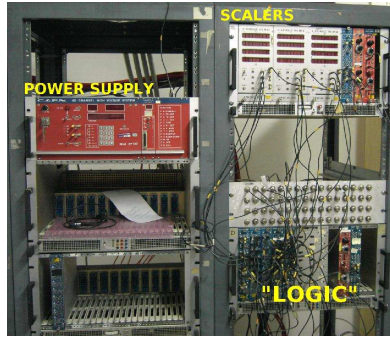


Figure 5.16: Trigger system in the control room.

When triggering over the whole chamber, the coincidence rate was about 7 Hz and the random coincidence rate was about 1 Hz. During the $ArCO_2$ measurement session, it was not possible to see the end of the chamber in the first 960 time bins. Therefore, the trigger was delayed by a NIM time module to divide the chamber in two time slices.

Chapter 6

The GEM Module

6.1 The GEM Foils

6.1.1 Description

The concept of the Gas Electron Multiplier (GEM) was developed in 1997 at CERN in the Gas Detector Development Group of F.Sauli. The fabrication technology was established by the CERN Surface Treatment Service ¹ which produced a large number of GEMs of various shapes and geometries.

The GEM is basically a thin metal-coated polymer foil (kapton), perforated with a high density of holes (between 50 and 100 holes/ mm^2). The typical geometry is shown in Figure 6.1 and consists of a 5 μm copper coating on a 50 μm kapton foil with 70 μm diameter holes at a 140 μm pitch. If the GEM size exceeds a certain value, one of the faces is divided into sectors (six in our case), to reduce the capacity.

A voltage difference of typically a few hundred volts is applied between the two conducting sides, thereby generating electric fields in the order of 80 kV/cm inside the holes, where the gas amplification of the drifting electrons occurs.

The pattern of holes is first engraved by conventional photolithography on the metal of both sides of the foil. The channels are then opened with a kapton specific solvent, using the pattern itself as a mask. The unprotected polymer is dissolved from both sides, thus giving rise to holes that have a double conical shape, with the diameter in the center of the insulator slightly smaller than at the metal surfaces; this helps improving the dielectric rigidity. To obtain a good manufacturing quality, avoiding potentially dangerous under-etching, the maximum hole diameter is usually limited to about two thirds of the pitch, and to prevent charging-up of the walls, the inner diameter should be as close as possible to the outer. For the device to work properly, a good insulation between the grid electrodes is required, with no sharp edges, metallic fragments or deposits in the channels; this has been obtained by careful optimisation of the etching and cleaning procedures.

The hexagonal arrangement of the holes is geometrically optimal and allows to have a pitch, P , two times bigger than the diameter of the holes, D . The *optical transparency* of the GEM, ratio of open to total area, assuming cylindrical holes, is given by [6]:

$$\tau = \frac{\pi D^2}{2\sqrt{3}P^2} \quad (6.1)$$

¹Technology developed by A.Gandi, R.De Oliveira and L.Mastrostefano.

which is around 0,23 in the standard geometry.

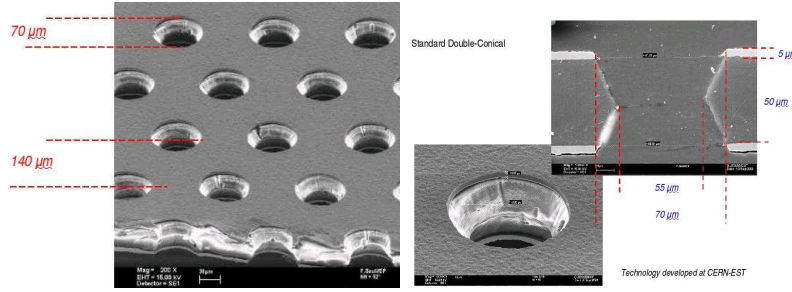


Figure 6.1: A GEM foil typical geometry (Left), the double-conical geometry (Right).

6.1.2 Amplification and Transfer Properties

Definitions

The GEMs are physically characterised by a few charge transfer coefficients. Let us first give some global useful definitions when considering a GEM setup as shown in Figure 6.2.

- The GEMs are labelled in such a way that the first GEM is considered to be the GEM with direct view in the chamber, and the last one to be the GEM above the pad plane.
- The faces of the GEMs that have view in the chamber are called *cathode* faces and the opposite faces are called *anode* faces.
- The field in the drift volume is called *Drift field*. The fields between the GEMs are called *Transfer fields* and the field between the last GEM and the pad plane is called *Induction field*.

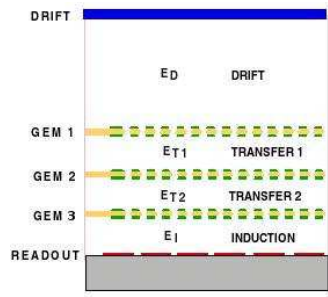


Figure 6.2: Typical triple GEM setup.

When optimising a GEM readout plane, three intrinsic parameters should be taken into account:

- The *electron transparency*, T_{elec} , i.e. the fraction of primary ionisation that experiences amplification, should be near to 100 %.

- The *effective gain*, G_{eff} , i.e. the number of electrons reaching the anode pads per primary electron, should be sufficiently high.
- The *ion feedback*, B_{ion} , i.e. the fraction of ions that reach the cathode plane, should be minimal.

To study the amplification and transfer properties of a GEM foil, charge transfer coefficients are commonly introduced in many studies (see [7], [8] or [6] for example):

- The *collection efficiency*, $C^{-(+)}$, i.e. the fractions of electrons (ions) collected into the GEM holes per number of arriving electrons (ions).

$$C^{-(+)} = \frac{\#e^-(I^+) \text{ collected in hole}}{\#e^-(I^+) \text{ arriving}} \quad (6.2)$$

Actually, the electrons collected in the hole being generally multiplied, their absolute quantity can not be measured but instead, its product with the gain, G . It is then common to introduce the *relative collection efficiency*, normalised by the maximal measured value:

$$C_{rel}^- = \frac{C^- \cdot G}{C_{max}^- \cdot G} \quad (6.3)$$

- The *gain*, G , i.e. the multiplication factor inside the GEM holes.

$$G = \frac{\#e^- \text{ produced in hole}}{\#e^- \text{ collected in hole}} \quad (6.4)$$

Here also, because of the multiplication, these two quantities can not be measured independently and an *effective gain* is often introduced as:

$$G_{eff} = \frac{\#e^- \text{ extracted from the GEM}}{\#e^- \text{ arriving}} = C \cdot G \cdot X \quad (6.5)$$

Thus, the current detected on the anode and the current of primary ionisation are related by:

$$I_{Anode} = I_{prim} \prod_{i=1}^{N_{GEMs}} C_i G_i X_i \quad (6.6)$$

- The *extraction efficiency*, $X^{-(+)}$, i.e. the fraction of electrons (ions) extracted from the GEM holes into the drift volume per number of electrons (ions) produced in the holes.

$$X^{-(+)} = \frac{\#e^-(I^+) \text{ extracted from the GEM}}{\#e^-(I^+) \text{ produced in the hole}} \quad (6.7)$$

- The *secondary extraction efficiency*, X_{sec}^+ , i.e. the fraction of ions extracted from the GEM holes into the drift volume per number of ions which were collected into the holes.

All these transfer coefficients are defined as ratios of charges, but charges being produced and transferred continuously, this are equivalent to the ratios of the respective currents. These currents of drifting electrons and ions (I_D , $I_{T,n}$, $I_{H,n}$ and I_I , see Figure 6.3) can not be measured directly but can be calculated from the currents transferred on the electrodes (I_C , $I_{GEM,n,A/C}$ and I_A),

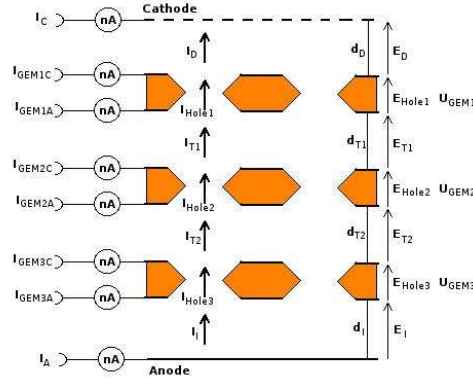


Figure 6.3: Fields and currents setup.

taking into account that every current has an electron and an ion component when calculating the coefficients for electrons and ions separately.

These calculations can become quite complex and more details can be found in [9]. Just to give an idea of the procedure, let us consider the extraction efficiency of GEM3, defined as the fraction of electrons extracted from the GEM holes into the induction region per number of electrons produced in the holes. From the measured currents on the anode face of the GEM and on the anode of the setup, it can be calculated as:

$$X^- = \frac{I_A}{I_A + I_{GEM3A}} \quad (6.8)$$

Simulation and Parametrisation

The charge transfer coefficients, thus calculated from the measured currents that appear on the electrodes of the GEM structure, are determined as functions of the electric field ratio E_{ext}/E_{hole} . Here, E_{ext} is defined as $E_{ext} = \Phi_{ext}/A_{ext}$, where Φ_{ext} is the flux onto an electrode (anode or cathode) of area A_{ext} , and E_{hole} is defined as $E_{hole} = \Phi_{hole}/A_{hole}$, where Φ_{hole} is the flux onto a hole of section A_{hole} . Actually, considering a model of the electric flux for one GEM hole in an asymmetric field configuration ([7]), it appears that both the collection and extraction efficiencies vary with the ratio between the external flux and the flux through the GEM hole. These considerations lead to the relation:

$$\frac{X}{C} = \frac{\Phi_{ext}}{\Phi_{hole}} = \frac{E_{ext}A_{ext}}{E_{hole}A_{hole}} = \frac{1}{T_{opt}} \frac{E_{ext}}{E_{hole}} \quad (6.9)$$

where T_{opt} is the optical transparency of the GEM foil. Further considerations give a linear dependency between the logarithms of the collection efficiency C and the field ratio E_{ext}/E_{hole} .

Many numerical simulations of the electric field fluxes (see [7]) allow the prediction of all these variables and the previous considerations lead to a parametrisation of the simulated results:

$$C = \begin{cases} 1 & \text{for } E_{ext}/E_{hole} \leq r^{1/s}, \\ r(E_{ext}/E_{hole})^{-s} & \text{for } E_{ext}/E_{hole} > r^{1/s}. \end{cases}$$

$$X = \begin{cases} \frac{1}{T_{opt}} (E_{ext}/E_{hole}) & \text{for } E_{ext}/E_{hole} \leq r^{1/s}, \\ \frac{r}{T_{opt}} (E_{ext}/E_{hole})^{1-s} & \text{for } E_{ext}/E_{hole} > r^{1/s}. \end{cases}$$

where $r, s \in \mathbb{R}^+$ are free parameters.

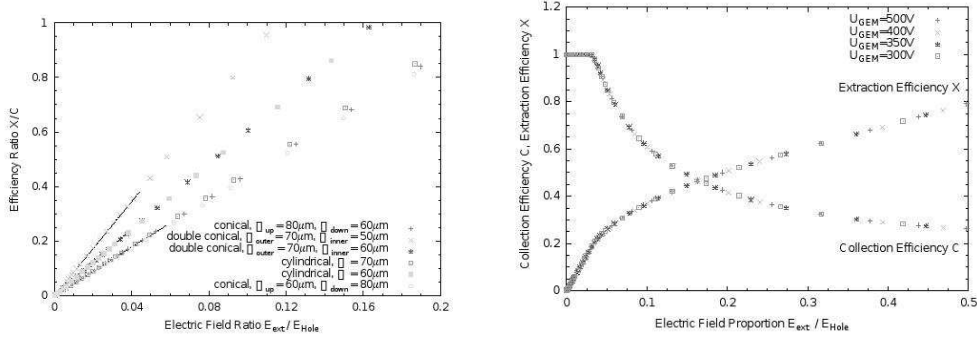


Figure 6.4: The ratio X/C for different hole diameters and shape (Left), simulation of the extraction and collection efficiencies for several GEM voltages (Right).

In these formulae, E_{hole} , the mean electric field inside a GEM hole, is itself the most important parameter of a GEM structure. It is defined from the integral of the electric field over the area of the hole, A :

$$E_{hole} = \frac{\int_A \vec{E} \cdot \vec{n} d^2r}{\int_A d^2r} \quad (6.10)$$

and is dependent on the geometry of the GEM, the voltage across the foil and the electric fields above and below the GEM (external fields E_D and E_I). The simulation suggests the following linear parametrisation:

$$E_{hole} = aU_{GEM} + b(E_D + E_I) \quad (6.11)$$

where the parameters a and b depend on the GEM geometry only.

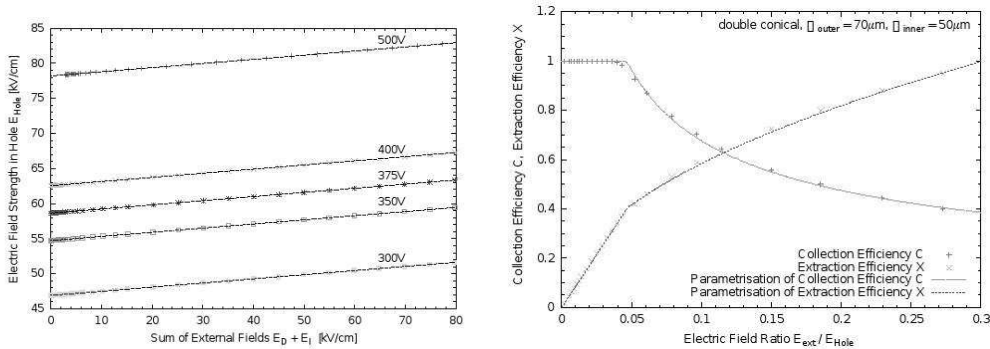


Figure 6.5: Electric field strength in GEM hole for different voltages and external fields (Left), simulated C and X efficiencies compared to their parametrisations (Right).

An almost perfect agreement between these parametrisations and the simulation results is observed over the entire range of the field ratio (see Figure 6.4 and Figure 6.5).

The next figures show the comparison between measurements and the parametrisation obtained from the electrostatic simulations. In this particular study ([7]), measurements were made in a chamber with $10 \times 10 \text{ cm}^2$ GEM foils, $\text{Ar} : \text{CO}_2$ (82:18) without magnetic field, P5 ($\text{Ar} : \text{CH}_4$, 95:5) with magnetic field, and a 0.1nA accuracy on the currents measurements; the simulation was done with P5.

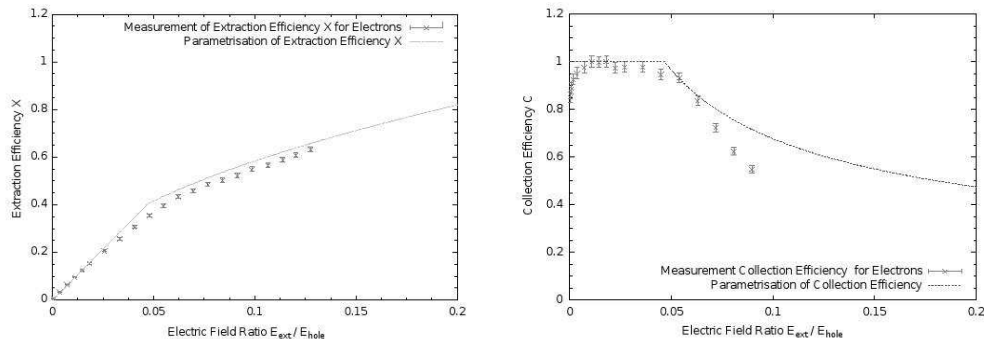


Figure 6.6: Measured extraction efficiency for electrons compared to simulation (Left), measured collection efficiency for electrons compared to simulation (Right).

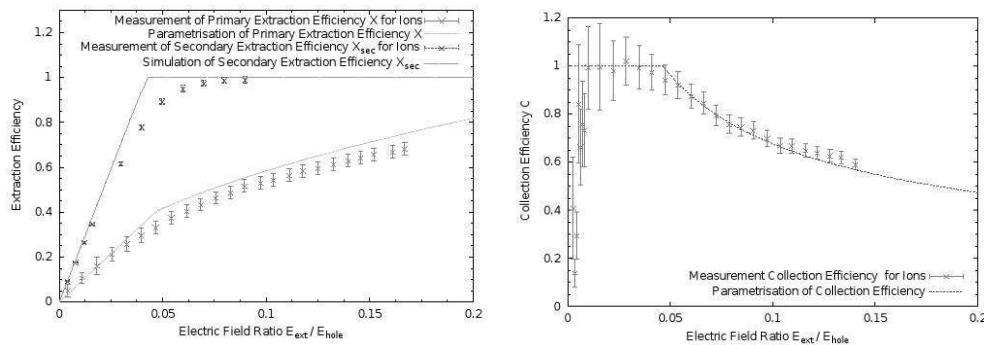


Figure 6.7: Measured primary and secondary extraction efficiency for ions compared to simulation (Left), measured collection efficiency for ions compared to simulation (Right).

Except for the electron collection efficiency, all data follow the simulation and this leads to the important conclusion that the charge transfert coefficients are mainly governed by the electrostatic conditions in the chamber and not by gas effects such as diffusion. This is also shown by the fact that the electrons and ions extraction efficiencies are equal within their respective errors. The differences between measurements and simulation are mostly explained by charge recombination problems (collection efficiencies for very low field ratio) and discrepancies between the ideal geometry of the GEM model and the real GEMs. Through the previously described parametrisation of the charge transfer coefficients, the ion feedback and effective gain can be determined (the current on the anode and the current of primary ionisation are related by the product of the charge transfer coefficients). The ion feedback is defined as $I_{FB} = I_{\text{Cathode}}/I_{\text{Signal}}$ and the effective gain as $G_{\text{eff}} = I_{\text{Signal}}/I_{\text{prim}}$ and since the charge amount in the ion back drift

is more or less in the same order as the primary ionisation, it comes that $I_{FB} \approx G_{eff}^{-1}$. Thus, for a typical effective gain of 10^4 , a minimal ion feedback of 10^{-4} should be expected.

In [8], a study leads to the following setting of the triple GEM structure for minimising the ion feedback: the voltages across GEM1 and GEM2 have few influence and enable variation of the gain without varying the ion feedback; E_{Trans1} should be minimal, whereas E_{Trans2} , U_{GEM3} and E_{Ind} should be maximal.

Finally, the previous study shows that the minimal ion feedback seems to be independant of the effective gain and that the goal of 10^{-4} seems difficult to reach.

6.1.3 Operating GEMs in magnetic fields

In the same study that was referred to in the previous section, further investigations were undertaken to understand the influence of magnetic fields on the charge transfer coefficients. Actually, the *Langevin formula* describing the motion of a charged particle in a magnetic field gives:

$$\vec{v}_{Drift} \propto \hat{E} + \omega\tau(\hat{E} \times \hat{B}) + \omega^2\tau^2(\hat{E}\hat{B})\hat{B} \quad (6.12)$$

where \hat{E} and \hat{B} are unit vectors of the fields and $\omega = \frac{e}{m}B$ is the cyclotron frequency. The term proportional to B^2 gives the contribution along the magnetic field lines and could easily cause a drop in the collection efficiency for high values of magnetic field. Using Garfield, drift lines have been calculated in the vicinity of a GEM foil with a 4 T magnetic field. The effect of the *Lorentz term* is clearly visible on the electrons (see Figure 6.8) but in the contrary, no contribution to the drift velocity along the field lines is observed.

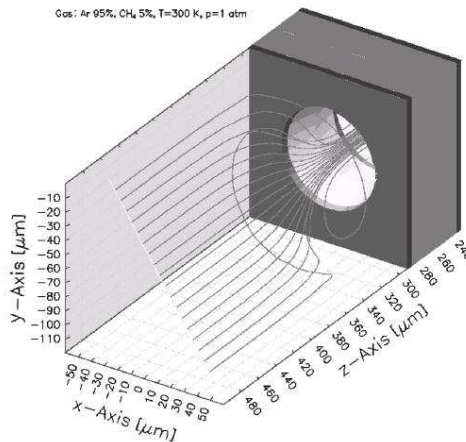


Figure 6.8: Garfield simulation of drift lines in a GEM hole in a 4 T magnetic field.

A quantitative analysis was done in [8] with a serie of currents measurements in a test chamber with a magnetic field up to 2 T and the main observation was an unexpected increase of the current on the anode. This behaviour is explained by an improved extraction efficiency for high magnetic fields, compensating for a hardly visible drop in the collection efficiency (see Figure 6.9). The results of this study show that the operation of a triple GEM structure is highly possible in a 2 T magnetic field.

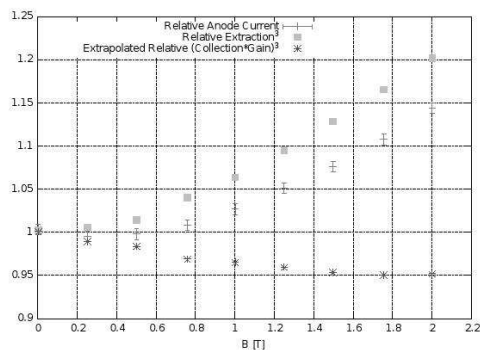


Figure 6.9: Anode current versus magnetic field.

6.1.4 Advantages of the GEMs

The GEMs show many advantages that make them particularly suitable for the readout of a TPC.

- It is a homogenous system and does not suffer from $\vec{E} \times \vec{B}$ effect.
- Cascaded GEMs allow larger gains and safer operation in harsh environments. Actually, as shown in Figure 6.10, for a same gain, the triple GEM structure considerably decreases the operation voltages of the GEMs, thereby giving a high stability to the system (reducing sparks probabilities).

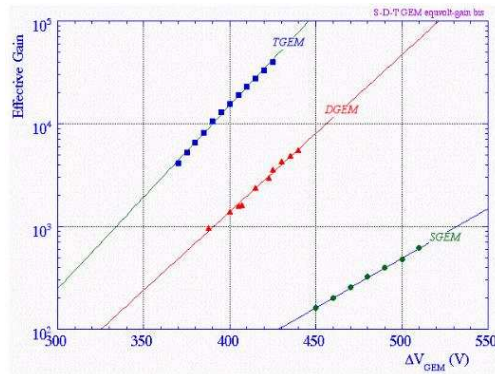


Figure 6.10: Effective gain for single, double and triple GEM structure.

- Due to the modularity of the electrostatic configuration of the triple GEM structure, ions do not penetrate the induction region and this automatically suppresses the ion tail. This results in very fast signals ($\Delta T \approx 20$ ns) and allows good multi-tracks ($\Delta V \approx 1\text{mm}^3$ instead of 1cm^3 for standard MWPC TPC) and time resolution.
- The ion feedback is highly suppressed without gating. It is a common observation to many studies that the ratio between the cathode and the anode signals is around 2% in standard TPC operating conditions ($E_{\text{Drift}} \approx 200$ V/cm). This is illustrated for a double GEM structure in Figure 6.12.

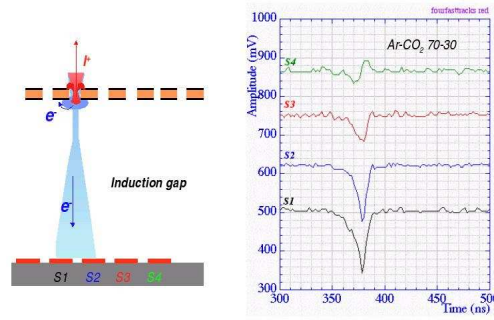


Figure 6.11: Charge amplification (Left), respective signals on the pads (Right).

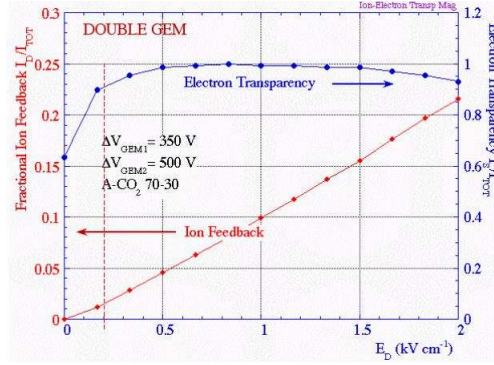


Figure 6.12: Ion feedback and electron transparency as functions of the drift field.

6.2 The GEM Tower

6.2.1 The Frames of GEMs

The GEM tower is basically a stack of three GEM foils, and the prototype consists in two adjacent towers mounted on a single pad plane. For this reason, two GEM foils on the same plane will be referred to as a GEM layer. The GEM foils are glued on vetronit frames. These frames were designed and manufactured by the technical team of the University of Geneva and are mostly an adaptation of the frames used in the COMPASS experiment ($315 \times 315 \text{ mm}^2$ active area), shown in Figure 6.13. The technical drawings of the frames are given in Appendix A.

The frames used for the prototype are schematically represented in Figure 6.14. They have dimensions of $215 \times 300 \text{ mm}^2$ with an active area of $200 \times 240 \text{ mm}^2$ to fit to the LHCb GEM foils. 8 frames with a width of 4 mm and 12 with a width of 2 mm have been produced.

The bottom side of the frames is 50 mm wide and contains services: on the cathode face, it is covered by the kapton foil where the resistors and the high voltage connections are soldered; on the anode face it is respectively equipped with a longitudinal groove, where the resistors of the previous frame are going to lodge when stacking the tower. By the same mechanism, it is also equipped with six small grooves (3×2) to lodge the high voltage connections of the previous frame (see Figure 6.15). It has also one hole on the external border to allow the high voltage connection of the guard ring.

The anode face of the frames are also equipped with two gas inlets (small grooves) on the external

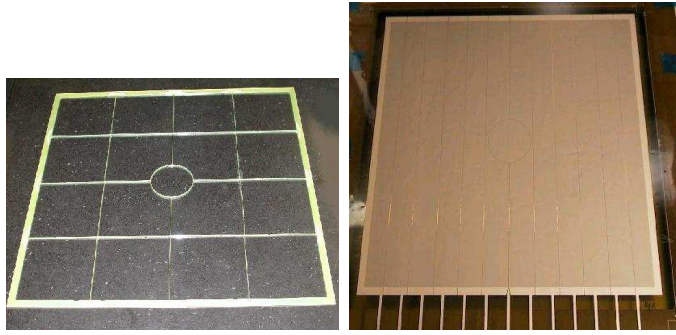


Figure 6.13: Frame (Left) and GEM foil (Right) for the COMPASS experiment.

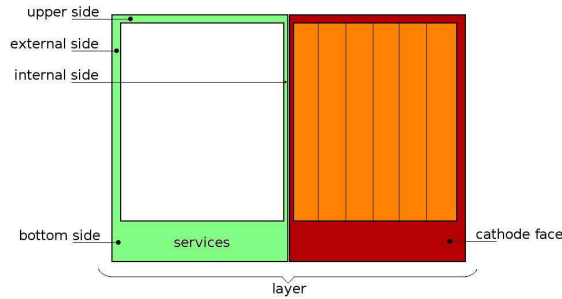


Figure 6.14: Schematic diagramme of a frame.

side (side on the border of the pad plane) for the gas distribution of the GEMs. Each frame has five fixation holes (thread of 2.5 mm diameter) to be fixed on the pad plane, one in each corner and one centered on the external side.



Figure 6.15: Cathode face of a frame (Left), anode face of a frame (Middle), detail of the service area of the anode face (Right).

The upper and external sides of the frames are 8 mm wide. The width of the internal side (the side adjacent to the other frame on the pad plane) has been carefully optimised to 4 mm. This value is still enough to get a sufficiently high rigidity to resist to mechanical and stress constraints, and enables to minimise the total dead area between the two frames to 8 mm only, which is the respective dimension of a pad on the pad plane. This internal side is equipped with two 2 mm diameter holes to lodge positioning plastic pins during the stacking (see Figure 6.16).

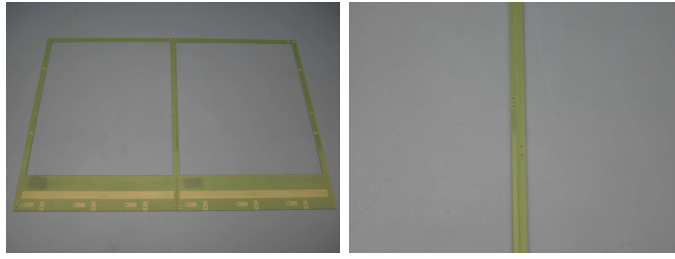


Figure 6.16: Frame layer (Left), detail of the junction (Right).

At the beginning, the frames were designed with spacers. These are very thin (0.5 mm width) vetronit bars left during the manufacturing of the frames, and forming a grid of six rectangular sectors over the GEM anode face. The two vertical spacers are located in the dead areas due to the sectorisation of the cathode face, and the horizontal spacer is centered on the frame, resulting in a very thin dead line on the active area. The purpose of this grid is to maintain the foil in its original position when the tower is under voltage and is commonly used in GEM detectors (see COMPASS frames).

In the final design, for different reasons, the frames were produced without spacers. First of all, this additional structure is a real manufacturing complication, and requires a much longer time of production for the frames. Second, a simple approximated calculation showed that the electrostatic force experienced by each foil is negligible with our foils dimensions and electrostatic configuration. Third, the first glueing tests demonstrated that the foils are sufficiently stressed on the frames, and finally, the decision to use the 4 mm width frames was the last argument to simplify the production.

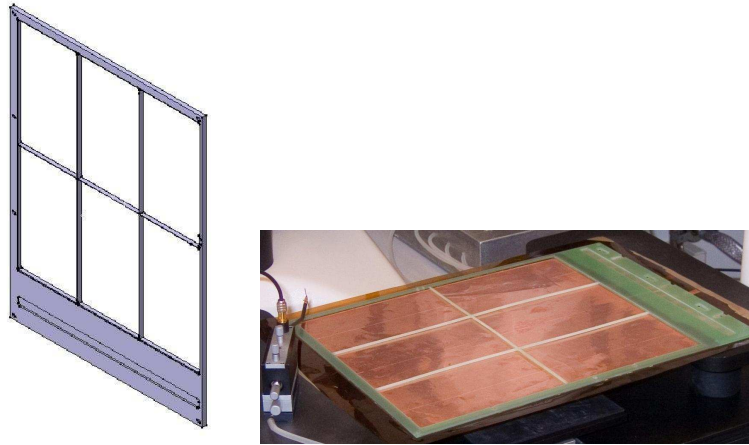


Figure 6.17: Frame with spacers conceptual design (Left), GEM foil glued on a frame with spacers (Right).

6.2.2 The Guard Ring

The guard ring is a 11 mm width PVC frame of dimensions $413 \times 300 \text{ mm}^2$ (see technical drawings in Appendix A), which is perfectly covering the contours of a frame layer. As for the frames, the

anode face of the guard ring is equipped with various grooves to lodge the services of the last GEM layer. The cathode face is entirely covered with a thin kapton foil coated with copper on one side (see Figure 6.18).

The guard ring has two functions in the tower; first, its mechanical function is to press the GEM tower from the top to have the all tightly fixed on the pad plane. Its second function is to properly define the electric potential, so that to get a homogeneous field between the cathode and the GEM surface.

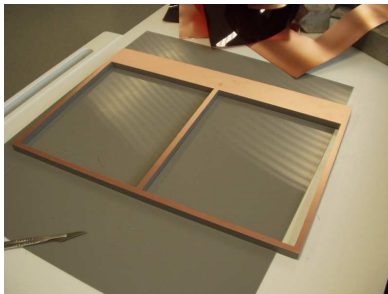


Figure 6.18: Copper coated cathode face of the guard ring.

6.2.3 The Pad Plane

In the prototype, the two GEMs sectors are fixed on a single pad plane. It has the same dimensions as the frame layer and is a compressed stack of 2 mm width, made of three layers of FR4² (see Figure 6.19).



Figure 6.19: Schematic side view of the pad plane.

On the upper layer (the cathode side of the pad plane), which is coated with $35\ \mu\text{m}$ of copper and $0.2\ \mu\text{m}$ of gold, are engraved (photo-chemical process) the two sectors containing each 732 pads. The pads have dimensions $8.3 \times 8\ \text{mm}^2$ with a pitch of 0.25 mm, and form rows of 30 and 31 pads. Two adjacent rows are shifted by half a pad. This design is referred to as staggered design. Each sector is made of 24 rows, intrinsically divided in six groups of four rows, one for each electronic module (see Figure 6.20).

The inner layer provides the gas tightness, so that there is no straight (from top to bottom) connections between the pads and the connectors. Every pad is connected to the respective pin of a connector via copper paths on the top of the last layer. Actually, the upper face of the intermediate layer is also coated with 4 large copper strips per sector to introduce charges in

²mix of epoxy and glass fiber

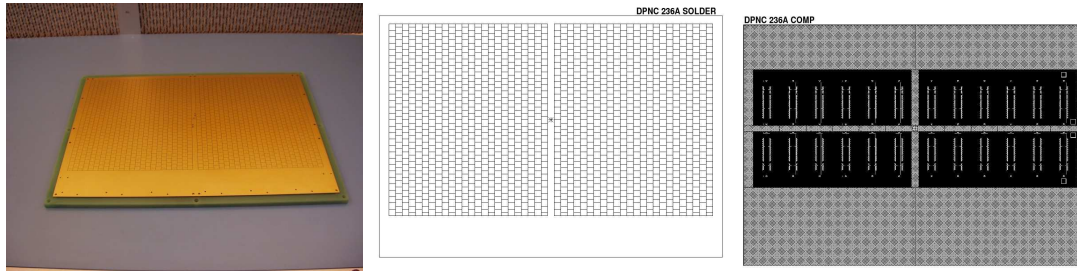


Figure 6.20: Pad plane view (Left), pad side (Middle) and connector side (Right) drawings.

order to test the two sectors of pads; but this function has not been used for the moment and will certainly be modified (for example by replacing the copper coated areas by sufficiently thin copper strips so as to test the pads row by row) in a future pad plane design. Finally, the bottom face of the last layer is also coated with copper and gold and acts like support for the connectors of the electronic modules and for a grounded grid (four connections are directly visible and allow soldering a cable to ground).

There are two connectors per module and six modules per sector, so this means 12 connectors per sector. Actually, 4 rows per module are read, that is 122 channels but we have two 64 pins connectors per module. This means that 6 channels are not read and directly put to ground. For practical reasons these channels are distributed as follows: 2 pins on the left connector and 4 pins on the right (left and right referring to the pad plane seen from outside the chamber in the vertical position, see Figure 6.21). Technical drawings and the drilling map of the pad plane are available in Appendix A.

6.2.4 The PCB support

The PCB support is a vetronit frame of 10 mm width and dimensions $326 \times 455 \text{ mm}^2$, that is a little bit larger than the pad plane to enable the fixation on the detector flange (technical drawings in Appendix A). This piece is designed to be a reinforcement for the whole structure (the tower is fixed on it), and especially in the central region of the pad plane, where it is shaped as a matrix to allow the fixation of the electronic modules on the connectors (see Figure 6.21).

6.2.5 The PVC Spacers

To get a good field uniformity, the guard ring has to be centered on one of the mylar strips which define the axial electric field in the chamber. Once the tower is mounted with the 4 mm frames, for the guard ring to be aligned in the middle of the second mylar strip, the all tower has to be shifted of 29 mm in the z direction. This is done by fixing the PCB support on a PVC spacer, which is a rectangular frame of 29 mm width and same dimensions as the PCB support.

There is a groove along the edge of the spacer to lodge an o-ring for the gas tightness. Actually, a second spacer of 6 mm width has been designed in the case where the 2 mm frames could be used, but this option has never been used until now.

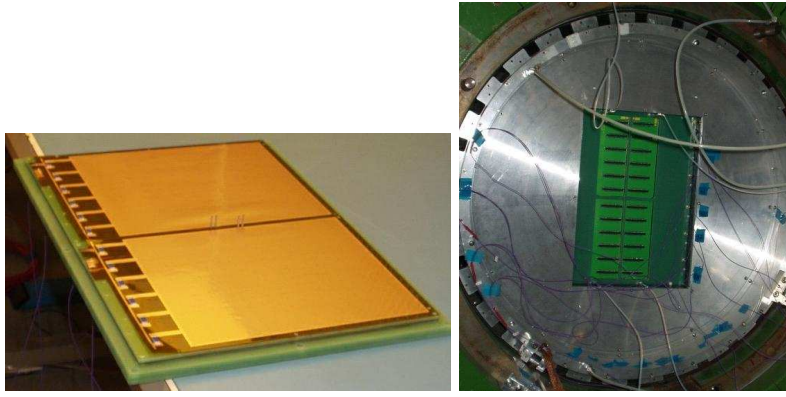


Figure 6.21: Pad plane and first GEM layer mounted on the PCB support (Left), view of the connector side (Right).

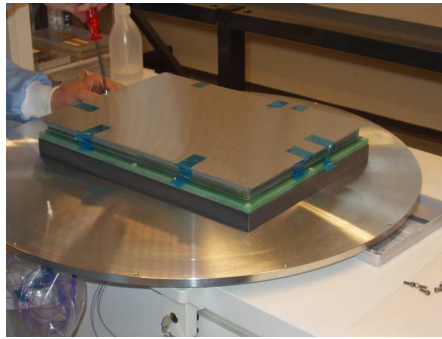


Figure 6.22: The GEM tower mounted on the PVC spacer (grey frame).

6.2.6 High Voltage Connections

Inner Connections and Protections

All the high voltage connections are made within the service area of the GEM tower, that we described in the frame section. Thus, every conductive parts are inside the tower with no direct view in the chamber. Each GEM layer has four high voltage connections, two for the anode faces and two for the cathode faces of the foils. Each foil is also equipped with six protection resistors on the cathode face in front of each sector. The only connection that has direct view in the chamber is the high voltage connection for the guard ring.

The High Voltage Box

The high voltage box, shown in Figure 6.23, is located next to the magnet and grounded to the general security ground. It consists of an aluminum box with SHV connectors on one wall, enabling soldering cables inside, thereby making the link between the power supply system and the detector. A set of 7 CERN standard high voltage cables are coming from the GEMs power supply system: three cables for the anode faces and three for the cathode faces respectively. The last one is for the shield and is not connected to the box but directly on the detector flange.

Another cable is coming from the field cage power supply system and is connected to the first copper strips via the box.

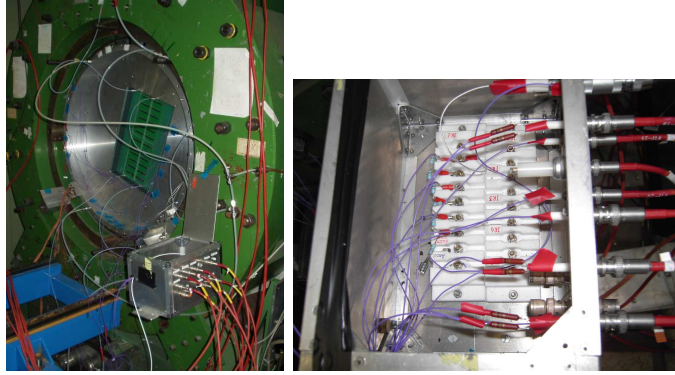


Figure 6.23: The High Voltage Box fixed on the magnet (Left), connections to the detector (Right).

The high voltage is delivered to the GEM tower layer by layer. Actually, the two cables of the anode faces of the same layer are soldered together before the high voltage box, and then soldered to a third cable connected to the SHV connector of the box. Connections are made in the same way for the cathode faces and protected with a special insulator black tape. The high voltage is directly delivered to the first copper strip via the box and then distributed to the two other strips by a resistive chain.

The Power Supply System

As for the photo-multipliers, a standard CAEN (40 channels HV system) Mod.SY127 is used, equipped with the Mod.A431. As it was explained before, the voltage is delivered layer by layer to the GEM tower; this requires 6 channels. Another channel is required for the guard ring, and a last one for the additional shield (that we will discuss in section 8.2.1). The channels and their respective outputs are summarised in Table 6.2.6, where, for example, 1A stands for the **A**node face of the first layer of GEMs on the pad plane.

Channel	Output	Channel	Output
0	1A	4	3A
1	1C	5	3C
2	2A	6	Guard ring
3	2C	7	Shield

Table 6.1: Channels and respective outputs.

The power supply can be monitored by computer via a RS232 connection. At the beginning, we used the MiniCom program, which allows to set individually the voltage and current limits for each channel. It is also possible to set the trip time (0.2 s correspond to 2 on the SY127) and the ramping up and down velocities. Afterwards we used another program called XTC (graphic interface) from the ILC (International Linear Collider) TPC Group Aachen, which has been slightly modified to fit the GEM configuration of the prototype. The inputs are the operating

voltages of the GEMs, the values of the drift, transfer and induction fields, the ramping up/down velocities for GEMs and fields and the number of restart you allow after a trip before stopping the process. The program then calculates the voltages to apply to each channel. There is also have the possibility to define working points with respective parameters, so a *Data taking* working point, a *Pedestal run* working point and an *Off* working point (to set all fields and voltages to zero) were defined. It is finally possible to register the values of the previous parameters in time in a data file, in order to get stability plots. Trip and current parameters can not be set with XTC but are kept in memory after the initial setting with MiniCom.

6.2.7 The Gas System

The Gas Distribution

The gas distribution of the chamber has been modified to incorporate the gas distribution of the GEMs. This is schematically illustrated in Figure 6.24. There are two gas inlets per sector, directly pierced through the PCB support, and which are in direct view with the respective grooves on the external side of the frames.

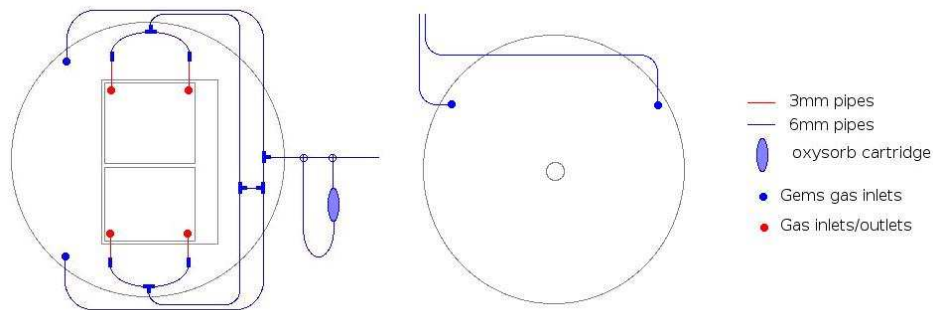


Figure 6.24: Complete gas distribution on the readout (Left) and cathode (Right) sides of the chamber.

Two 6 mm diameter pipes are coming from a T to each sector, and are then splitted in two by two other Ts, to join the two gas inlets of each sector. The gas distribution of the GEMs requires 3 mm diameter pipes and a kind of I is used to connect the 6 mm and 3 mm diameter pipes before the gas inlets. Because of a manufacturing mistake on the PCB support, the holes for the gas connectors were too close to the PVC spacer, and the connectors could simply not be screwed in. They were finally screwed on an adaptation aluminum pipe (see Figure 6.25).

The Gas Tightness

The connection of the 6 mm diameter pipes to the 3 mm diameter pipes are carefully wrapped with teflon tape, which is then covered with many layers of red tape. For the aluminum pipes, the threads are also covered with teflon tape before being screwed in the PCB support.

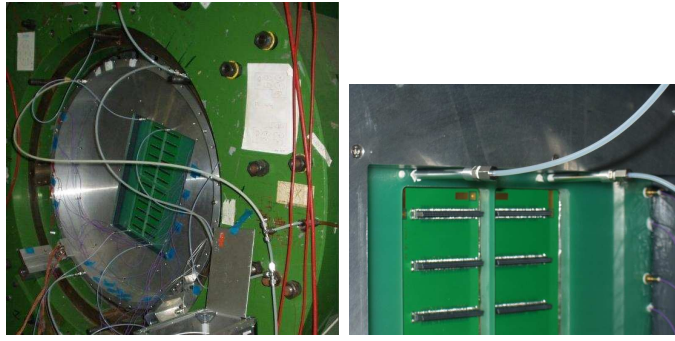


Figure 6.25: Complete gas distribution (Right), gas inlets for the upper GEM module (Left).

6.3 The Electronics

6.3.1 The Electronic Modules

The electronic modules are composed of a protection card, an inverter card and a front end card from the ALICE experiment [10]. The protection and inverter cards are directly plugged together and the inverter and the front end cards are connected with six kapton flex cables.

The Protection Cards

The protection cards are the first cards connected to the pad plane and are so referred to as *interface cards*. It consists in a set of two diodes and one capacitor of 100 pF per channel and protect the Altro chip in case of a discharge to the pad plane.

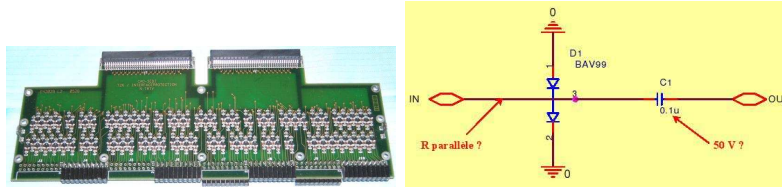


Figure 6.26: Protection card (Left), and its schematic (Right).

This protection was originally designed for the Micromegas prototype, but given the low additional noise generated (around $40 e^-/pF$), it appeared to be also advantageous for the GEM prototype.

The Inverter Cards

Unlike the conventional TPC with multi-wire proportional readout chambers, where the positive signal induced by the ions on the pad plane is read, with micro-pattern gas detectors are directly read the negative signal of the electron clouds. Inverter cards are therefore necessary to convert this negative signal into a positive signal. The original reason is that the ALICE TPC is using wires. The noise of the inverters is around $700 e^-/\text{channel}$ (for 0 pF).

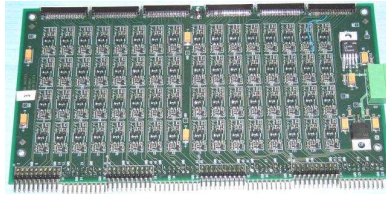


Figure 6.27: Inverter card.

The Front End Cards (FECs)

The FECs used for the readout electronics, are part of the front end electronics (FEE) developed for the ALICE experiment. A FEC accommodates 128 channels and a single channel is comprised of three basic functional units:

- A charge sensitive amplifier/shaper with a semi-gaussian response (190 ns FWHM).
- A 10 bit 25MSPS ADC.
- A data processor with a multi-acquisition buffer. The ADC and the data processor, for 16 channels, are implemented in a custom mixed-signal chip, called the ALICE TPC Readout or ALTRO chip.

The signal flow starts at the end of the detector, the analogue signal passes through the protection and inverter cards, and is transported through the six flex cables and connectors of the FEC. The preamplifier/shaper (PASA, see Figure 6.28) has very short connections to these connectors in order to minimise the cross talk caused by the fast input signal of the ALICE experiment.

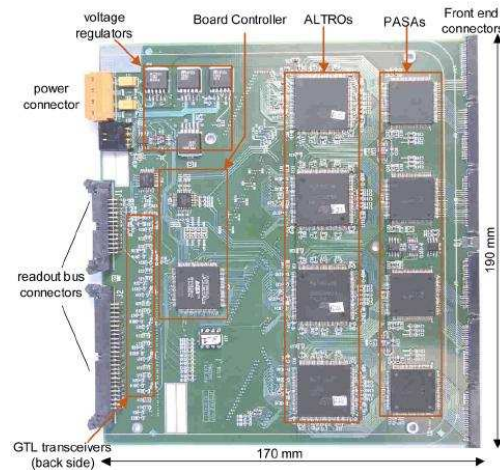


Figure 6.28: Front End Card.

The charge collected by a pad is amplified and integrated in the PASA, which has a low input impedance amplifier, followed by a semi-gaussian pulse shaper (fourth order gamma function of the ratio between the starting time and the relaxation time). These analogue functions are realised by a custom integrated circuit which contains 16 channels with a power consumption of 11 mW per channel. The circuit has a conversion gain of 12 mV/fC and an output dynamic

range of 2 V with a differential non-linearity of 0,2%. It produces a pulse with a rise time of 120 ns with a shaping time of 190 ns (see Figure 6.29). A single channel has a noise value below 570 e^- (r.m.s) and a channel-to-channel crosstalk below -60 dB.

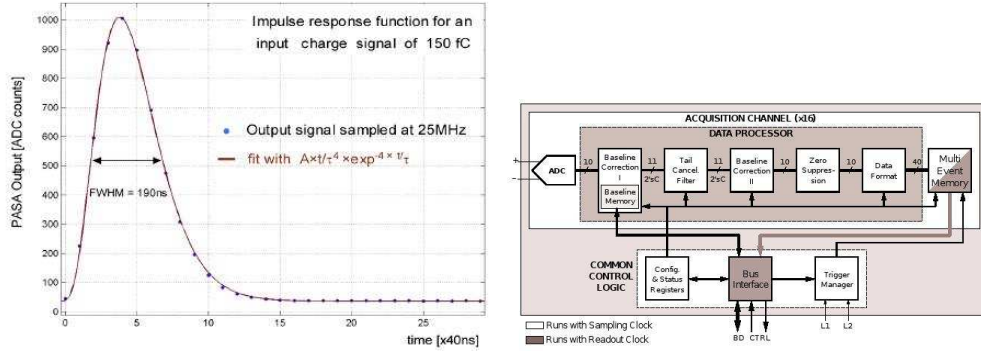


Figure 6.29: The PASA response function (Left), the ALTRO chip block diagramme (Right).

Afterwards, the ALTROs are directly connected to the PASAs using differential signals. With the ALTROs the analogue part of the FEC is ending, and the digital part is starting. The ALTRO chip integrates 16 channels, each of them consisting of a 10 bit 25MSPS ADC, a pipelined digital processor and a multi-acquisition data memory (see Figure 6.29).

Immediately after the PASAs, the ADCs sample the signal at a rate of 10 MHz. An important point is that, the ADC sampling frequency and the readout speed are independent, so that the readout frequency does not depend on the bandwidth of the input signal being acquired. The digitised signal is then processed by the set of circuits that perform the baseline subtraction, the tail cancellation and zero-suppression, formatting and buffering (more details in the *Data Acquisition* section).

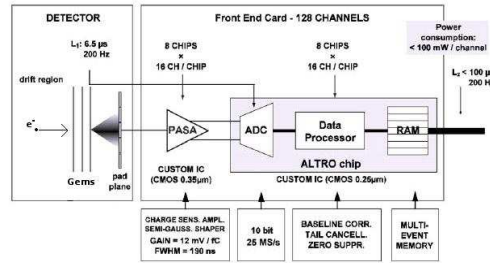


Figure 6.30: Front-end electronics basic components.

In total, the FEC has a maximum power consumption of 6W. All the basic components of the FEC are schematically described in Figure 6.30. When a Level-1 trigger is received, a predefined number of samples is temporarily stored in a data memory and the FEC has to be amplifying, shaping, digitising, processing and buffering during the Level-2 trigger latency (period over which the latest acquisition is frozen, otherwise it would be overwritten by the following acquisition). Over this period, after the amplification, shaping and digitising, the data processor implements several algorithms that are used to condition and shape the signal: these are the first baseline correction, the tail cancellation, the second baseline correction and the zero-suppression. All

these processing blocks are detailed in [11] and will be further considered in the *Data Acquisition* section. Finally, each non-zero data packet which is produced, is formatted with its time stamp and size information, so that the reconstruction is possible afterwards, and sent to a data memory of 5 Kbyte able to store up 8 full acquisitions. The data can be read out from the chip at a maximum speed of 60 MHz through a 40 bit wide bus.

In the case of the ALICE experiment where the FECs are directly connected to the detector via the flex cables, the length of the path between the pads and the FECs is around 7 – 8 cm and the noise per channel is around $600e^-$ which is about 0.1fC and 0.6 ADC counts. In our case, taking into account the protection and inverter cards and the longer path between pads and FECs (20 – 25 cm), the noise should be roughly larger of, at least, a factor of 3, which is perfectly corroborating the approximative value of 2 ADC counts that was usually observed.

The Electronics Mechanical Support

The support of the electronics is done in two parts: the first part is the structure which forms the electronic modules themselves and the second part is the overall mechanical structure that supports all the modules.

- The structure of the modules is schematically described in Figure 6.31. The cards form a stack and the shield is inserted between the flexes and the FEC. Four aluminum plates are screwed on the sides of the stack (two on the set PC/IC and two on the FEC) and are fixed together by four pilars. The shield is perforated in each corner at the level of the pilars and is kept in place by small plastic pipes surrounding the pilars and that press it against the FEC.

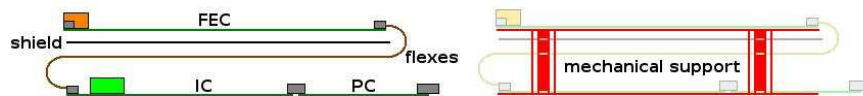


Figure 6.31: Schematic side view of the electronic module.

- Four aluminum *Us* (thick mechanical pieces shaped as a U) are screwed on the detector flange at each corner of the active area. They are connected two by two on each vertical side by PVC bars. These bars are equipped with 12 grooves to lodge the aluminum plates screwed on the FECs; the modules are then slid between the bars until the protection cards are connected on the back of the pad plane, and are thus kept in the horizontal position. Of course, every screws used for the mechanical support should be certified amagnetic.

6.3.2 The Readout

The USB to FEC interface (U2F)

The U2F is the interface card between the PC and the FEC. For the communication with the PC, the U2F supports the USB 2.0 High Speed (480Mbit/s) interface. The communication with the FEC is based on the ALTRO protocols which are described in [11]. The bridge between the U2F and the FEC relies on a micro-sequencer which can sequentially execute a set of pre-loaded instructions. In this way, a large part of the FEC configuration (running with/without zero-suppression, type of zero-suppression, etc.) can be send to an instruction memory, and

then executed with a single command (see section 9.2). The U2F card is equipped with a USB connector and a LEMO connector for the trig-in signal. All the FECs are connected to the U2F via two ribbon cables (equivalent to the bus of ALICE), one of 25 pin connectors and the other with 50 pin connectors. The requirements for the cables are adapted from the requirements of the bus: 7 control lines, 4 dedicated lines for the distribution of the Level-1 and Level-2 triggers, the readout and ADC clock, 40 bi-directional lines for data, addresses and instruction code, and finally a signal frequency up to 40 MHz.

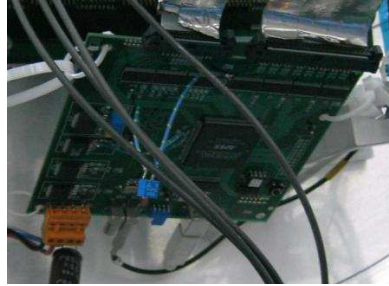


Figure 6.32: USB to FEC interface.

The Termination card

The termination card is connected at the other edge of the two ribbon cables. It has two functions: the first one is to avoid the reflections of the signals along the transfer lines of the cables, and the second is to provide additional 1.5 V to the last cards (otherwise, there could be a voltage drop over the bus cables).

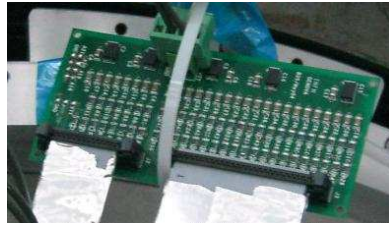


Figure 6.33: Termination card.

6.3.3 The Low Voltage Supply System

Voltage and Current Consumptions

Here we give the power consumption for the different type of cards:

- The inverter cards have two voltage inputs, +7 V and -7 V, and the respective grounds. The required current is 0.1 A on the +7 V input and 0.15 A on the -7 V.
- The FECs have two voltage inputs, +3.3 V and +4.3 V, and the respective grounds. The required current is 1.05 A on the +3.3 V input (current peak could go up to 1.6 A) and 0.55 A on the +4.3 V.

- The U2F have two voltage inputs, +5 V and -5 V, and the respective grounds. The required current is 0.05 A on the +5 V input and 0.55 A on the -5 V.
- The termination card has one voltage input, +1.5 V and the respective ground, and a very low current input.

Power Supplies

The low power supply system consists of five power supplies (see Figure 6.34):

- 3 Programmable DC PSU of type TSX1820P. This type delivers up to 18 V and 20 A on one channel.
- 2 Konstanter LSP of type 33K7(5/2). This type delivers up to 25 V and 1 A on two channels and 7 V for 5 A on a third channel.

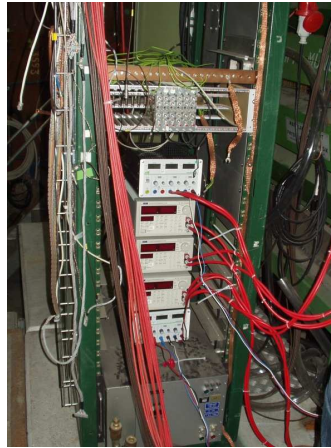


Figure 6.34: The low power supply system.

The two Konstanter LSP are used for the ± 7 V respective inputs of the inverter cards. The power supply used for the +7 V input is also used for the +1.5 V input of the termination card, and the power supply used for the -7 V is also used for the ± 5 V inputs of the U2F. As far as the +3.3 V input is concerned, the FECs are splitted in two groups of six and two of the three programmable DC PSU are used for these inputs. This splitting is due to the fact that the current consumption of the FECs on this particular input is too high to be delivered to the 12 cards by a single power supply. Finally, the third DC PSU is used for the +4.3 V inputs of all the FECs.

6.3.4 The Cabling

Cabling of the Inverters

The cabling of the inverters does not require special cables and standard cables recommended for this kind of application are used. At the beginning, the twelve cards were connected via a connector chain, as shown in Figure 6.35. This option, though simple, did not appear to be very practical. Later this was replaced by voltage distribution bars: these are three copper bars, two for the ± 7 V inputs and one for both grounds (the two grounds are connected at the level of the

connector on the cards), fixed on the electronics support structure. The bars are equipped with holes all along to fix the respective cables for each connector, which are then independent of each other. This configuration has two advantages: it offers more handling freedom and it seems to have a benefic influence on the mean RMS per board, since a slight decrease of the noise during pedestal runs after this modification could be observed.

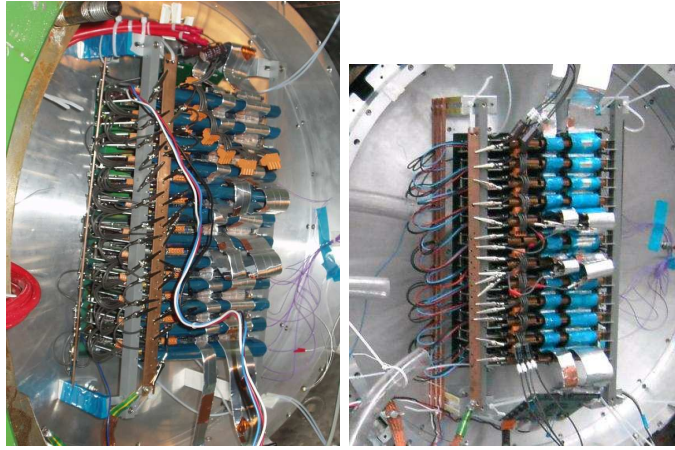


Figure 6.35: Inverters connected via a connector chain (Left), and via voltage distribution bars (Right).

Cabling of the FECs

For the FECs, which are divided into two groups of six, the current consumption are much higher than for the inverters, and the system could not work properly when using standard cables. Instead thick red cables with a copper cross section of 25 mm^2 were used. Of course, this kind of cables requires a little bit of adaptation work to be fixed to the connectors of the cards on one side, and to the power supplies on the other. For the connectors, short standard cables were soldered at the very end of the red cables and then fixed on the six connectors chains. For the power supplies, the copper cross section was partly screwed in banana pins and the junction was then tightly insulated with red tape. Figure 6.36 shows the complete cabling of the all system.

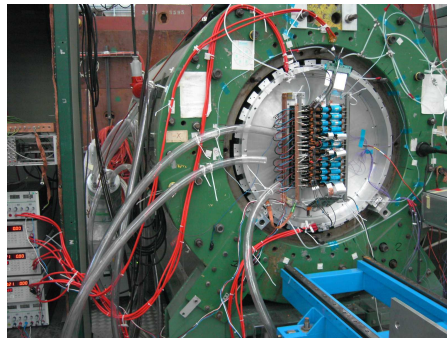


Figure 6.36: Complete cabling of the detector.

6.3.5 Analogue and Digital Signals Isolation

In order to avoid interferences of the analogue signal with the digital signal, these two parts have to be physically isolated from each other. These interferences can occur at three different levels in our setup:

- **At the level of the grounds.** Each type of signal should have a different ground and, in an ideal case, these two grounds should be as far as possible from each other. This point will be further detailed in the following section.
- **At the level of the flex cables used to connect the inverters to the FECs.** Once the electronic module is mounted, these flexes can be directly in contact with the bottom face of the FECs, thus generating interferences with the digital signal. To avoid this situation, a kapton foil coated with 70 μm of copper is inserted between the flexes and the FECs. Actually, in a thick conductive plane, the current density decreases exponentially with the depth, δ , according to:

$$J = J_s e^{-\delta/d} \quad (6.13)$$

where the skin depth, d , is defined as:

$$d = \sqrt{\frac{2\rho}{\omega\mu}} \quad (6.14)$$

where ρ is the resistivity of the material, $\omega = 2\pi f$ is the angular frequency and μ is the absolute magnetic permeability. In our case, the time sampling frequency is of 10 MHz, which gives a skin depth of 21 μm for the copper. The shielding used for the modules is therefore highly sufficient to completely isolate the FECs from the flexes. At the beginning, copper shieldings were also inserted between the electronic modules themselves, but it appeared to have no real benefic influences on the noise.

- **At the level of the bus cables which are connected to all the FECs and can sometimes touch the flexes where these are bended.** To avoid any interferences, the bus cables were first covered with an adhesive aluminum tape. Then, 70 μm width copper pieces were added between the connectors where the bus are really surrounding the flexes, and the all was wrapped with insulating blue tape.

6.3.6 The Grounding

The Digital Ground

The detector ground (which is anyway connected to the general security ground) is the detector flange itself. In order to separate the digital ground from the analogue ground, the digital is connected to the detector ground, whereas the analogue is let floating. The digital ground consists of a copper bar fixed on the electronics support structure and connected to the HARP flange with a copper braid (see Figure 6.37). The digital part of all the FECs is connected to this bar with short cables and crocodile pliers. Two cables per readout cable are also connected to the digital ground in the same way. The pad plane is connected to the detector ground via a cable soldered on the connector side and fixed to the magnet.



Figure 6.37: Connections to the digital ground.

The Analogue Ground

The analogue ground consists also of a copper bar which is fixed on the electronics support structure in such a way that it is completely isolated from the rest of the structure and can be considered as floating. Two cables per module (one for the protection and inverter cards and one for the analogue part of the FECs) are connected to the analogue ground, as shown in Figure 6.38.

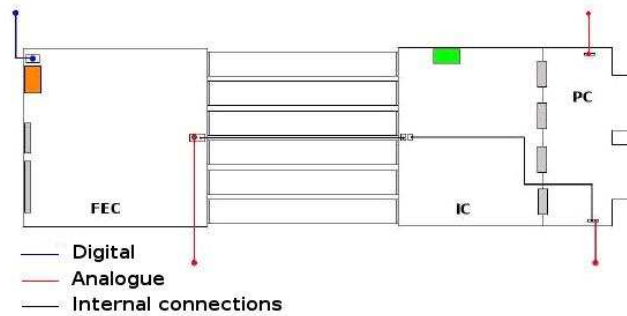


Figure 6.38: Ground connections of the electronic modules.

The shield between the flexes and the FECs is soldered on one of the aluminum plate fixed on the protection card, and is therefore also connected to the analogue ground.

6.3.7 The Cooling System

Due to the high power concentration, a significant heating up can be observed quite soon after switching on the readout electronics. This rise in temperature seems to have an influence on the stability of the data acquisition system. To cool the electronics, an air pump is used, which can blow cold air through a set of large plastic pipes, that were fixed onto the magnet so as to get an air flow between the electronic modules.

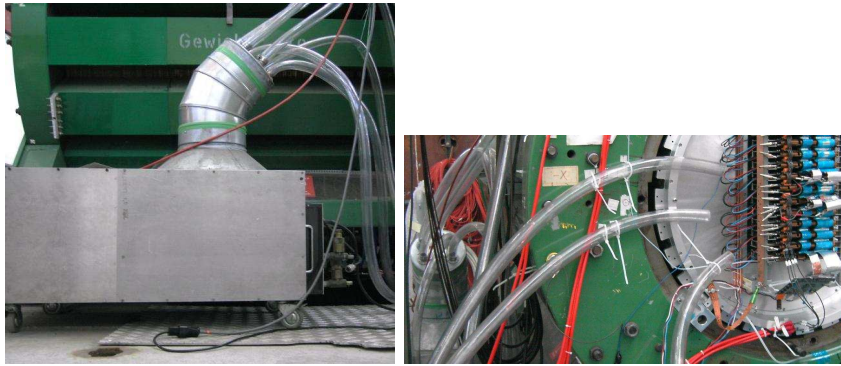


Figure 6.39: Pump of the cooling system (Left), cooling pipes (Right).

In running conditions with magnetic field, the same set of pipes can be introduced near the electronics through rectangular grooves at the edge of the iron endcap.

6.3.8 Debugging the Electronics

In order to have the all system runing, a lot of work has been done on the electronics at different levels:

- **Modifications of the electronics to be read out by flat cables instead of the standard data bus used for the ALICE experiment.** This consists in correctly setting the hardware addresses on the boards by removing and replacing a few resistors, and modifying boards and cables to be able to reset the boards from the U2F. The logic levels in the readout cable were not correctly define because of voltage drops along the reference line. This problem was resolved in reducing the voltage reference (down to 700 mV) from the U2F, by replacing a resistor with a potentiometer.
- **Modifications of the setup to get the system runing with 12 boards.** As explained before, this mainly consisted in setting the proper voltages using these large cross section cables and placing 4.7 mF capacitances at the level of the voltage connectors of the FECs, to avoid jitters when the driven current was large. It also consisted in setting the proper ground connections and shieldings to avoid interferences between analogue and digital signals. The readout could not be done in a stable way when more than six boards were successively connected to the bus cables. This finally led to a configuration of $5 + 2 + 5$ connections, separated with two empty connectors (the cables have 16 connectors).
- **Modifications related to the data acquisition system.** Some modifications were required in order to run the system in push mode. This implies changes in the DAQ code, that has to run asynchronously with respect to the events, and changes in the configuration of the boards.

Chapter 7

Building Operations

7.1 The GEM Foils

7.1.1 Testing Procedures

For the construction of the prototype, a set of 12 GEM foils was retrieved from previous preliminary tests for the LHCb experiment in the year 2002. These foils have an active area of $240 \times 200 \text{ mm}^2$.

A first point worth mentioning is that this set did not pass these quality tests, which is suggesting that it is not a set of first manufacturing quality. This question of quality, although important, was not a crucial point for the decision of building a prototype.

A second point which is to mention, is that the first steps of the testing procedures were done at CERN, in a clean room used for the COMPASS experiment. COMPASS technical notes ([12]) were mainly used to elaborate the testing and glueing procedures of the GEM foils. In a second time, more developed facilities were provided by the Physics section of the University of Geneva, and all procedures were started again from the beginning. Tests and building operations were undertaken in a clean room previously used for the production of the inner silicon tracker of the ATLAS experiment. This spacious room is equipped with a large laminar flux, drying boxes, power supplies, microscopes and many other facilities (see Figure 7.1). In the following sections, we report only the testing and building periods at the University of Geneva.

Optical and Electric Check of the Foils

A first optical check was done by eye on the surfaces of the foils and any visible defect was then more carefully checked under the microscope. At this very first level, criteria for acceptance or rejection of the foils should be clearly defined and are still to be understood at this moment. In the case of the prototype, for practical and time-table reasons, we did not go through this step in the most careful way. A very first electrical test consisted to check the connections of the faces of the GEM foils and, in particular for the cathode face, to check the connections of the six sectors with a multimeter.

High Voltage Tests

During the building of the prototype, many operations (glueing, soldering resistors, preparing high voltage contacts, soldering high voltage cables, assembling) have to be done on the GEM



Figure 7.1: Global view of the clean room (Left), laminar flux (Middle), dry boxes used to store the GEMs (Right).

foils, and after each of these steps, a new high voltage test is necessary to check any damage of the GEMs. In this purpose, a test bench was designed and constructed at the University of Geneva (see Figure 7.2). It consists in a large aluminum box with a plexiglass lid, equipped with SHV connectors on two walls and with one gas inlet and outlet. The box is directly linked to the gas distribution system of the clean room through pressure and flow regulators, thus enabling tests under a flow of nitrogen.

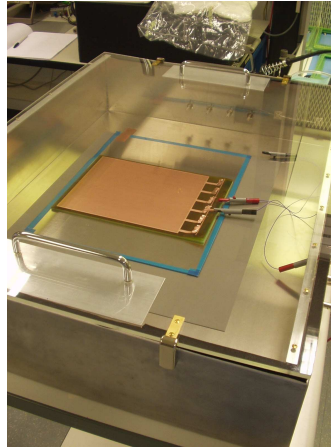


Figure 7.2: High voltage test bench.

7.1.2 Preparation of the Foils

There are three kinds of foils: foils with the cathode and anode strips on the left side, foils with the strips in the middle, and foils with the strips on the right side. The GEMs were labelled and classified accordingly. This distinction is necessary for the building operation: since the GEM layers have to be connected through the pad plane, it is important that each layer has a different position of the connectors.

Before the glueing operation, the GEM foil has to be electrically tested. It is first cleaned under

the laminar flux with an ion gun. This gun ejects nitrogen and is equipped with a cathode which emits electrons when heated. This particular setup is useful to get rid of any electrostatic dusts. The foil is then deposited in the test bench on an aluminum plate, itself on a PVC layer. The aluminum plate is linked to the bottom wall of the box with a strip of copper conductive tape. High voltage is delivered to the box by a NIM module ¹ via a 100 M Ω resistor. The cathode face of the GEM foil is connected to the high voltage and the anode face to the ground (the ground return is done via the box itself). The cathode face being divided in 6 sectors, the voltage is delivered through a common divider (copper strip on the kapton foil along the active area). In this first testing step, the sectors were connected to the divider by little adhesive copper strips (see Figure 7.2).

The test consists in applying a voltage difference of 500 V between the two conductive faces of the foil. This value is much larger than the operating value of the GEMs in the TPC (around 320 V in $ArCO_2$) and was chosen so as to get a large and safe margin of operation. The voltage difference is applied in many steps: first by steps of 50 V between 0 and 300 V and then by steps of 25 V. The criteria of acceptance is that the foil stands this voltage difference for a sufficiently long time without sparks, and with a crossing current less than 5 nA (actually this upper limit has never been reached). Among the set of GEMs, two foils did not pass this first high voltage test and were given back to the CERN STS for cleaning and were finally retrieved.

7.2 The Frames

7.2.1 Preparation of the Frames

The frames are manufactured out of vetronite, which is not an easy material to machine, especially because of the huge quantity of thin little fibres it generates. In particular, these fibres can partially stay along the cuts, and could cause damage in the detector if not removed. This is the reason why the frames have to undergo a special treatment before the GEM foils to be glued on them:

- In a first time, the whole surface of the frame is manually polished with emery paper foils of a very fine grit. A particular care is taken to remove every fibres from the cuts and corners and the frame is blown with compressed air.
- After this operation, in order to completely clean the frame, it is plunged in alcohol in an ultrasonic bath for 5 minutes.
- Finally, to be sure that no sharp piece is left on the frame around the active area of the GEM foils, its surface is covered with a special varnish called *Nuvovern LW Klarlack* (3 : 1) ². It is actually a two-components polyurethane resin-based mixture that has to be mixed with the appropriate hardening product called *Pur Härter LW*. The latter is an aliphatic isocyanates-based mixture in the form of organic solvent. The final mix is then sprayed on the frames with an air pistol and afterwards, the frames are stored for drying a few hours. The appropriate precautions should be taken when handling such products and every operations should be done in an airy room (or outside) or in a room equipped with an airing hood. All the tools used for the varnishing of the frames can afterwards be cleaned with a toluene solution.

¹Power Supply Mod 471 A Caen with nA sensitivity.

²Walter Mäder AG

7.2.2 High Voltage Test

Before the glueing operations, the frames have also to pass a high voltage test. The test consists approximately in the same procedure used for the GEM foils: the frames are placed in the test bench between two aluminum plates, with the bottom plate grounded and the top plate put to a certain potential. It is required that the 4 mm frames should stand a voltage difference of 5 kV and that the 2 mm frames should stand 4 kV. All the 4 mm frames satisfied to the requirements, and it appeared that the 2 mm frames could stand voltages between 3.2 and 4 kV. As for the GEMs, these requirements are much more than expected in the operating conditions of the TPC, and are defined to provide a large margin of operation.

7.3 Glueing Operations

7.3.1 Glueing the Pad Plane

The glueing of the pad plane on the PCB supports also requires different operations. In a first time, the PCB support is also polished with emery paper. The PCB support being much thicker than the frames, this step can be done with an electrical sander with no risks. The support is then cleaned with alcohol. The pad plane is also cleaned and then covered with an electrostatic film to avoid any depositions on the pads.

All the tower is to be fixed from the guard ring in the PCB support with nylon screws of 2.5 mm diameter. The respective threads (5 per frame) have to be inserted in the support before the glueing. This is done with a big manual press after positioning the threads in the most vertical way.

Standard Araldit has been used for all the glueing operations described in this report. It can be found as a two-component package of 24 mL. After mixing the two components, the hardening time is of 90 minutes. The glue is first spread on the respective area of the PCB support with a flat spatula and then with a jagged one in order to get a good uniformity. The pad plane is then carefully placed on the support, and plastic pins are inserted in the central positioning holes and in the threads, to prevent the glue to go inside. Lead weights are deposited on a glass plate that covers the pad plane, and the all is let for drying over one night.

7.3.2 Glueing the GEM Foils

The glueing of the GEM foils on the frames is a delicate operation. From this point on, the GEM foils should be handled in the cleanest conditions as possible, and all operations are undertaken under the laminar flux. Here are described the different steps to follow:

- Clean the frame with alcohol and place it at the center of the luminous table, using blue tape to fix it at each corner to avoid any displacements during the alignment.
- An aluminum frame has been manufactured to act like support for stretching the foils. Clean the foil with the ion gun and place it on the aluminum frame so as to cut the overall kapton foil which is sticking out.
- Stretch the foil on the aluminum frame using blue tape strips. The tape should always be glued successively on one side and the opposite one at the same position so that the foil is stretched as much as possible. It should be checked before doing this, that the foil is in the right position, that is anode face up above the aluminum frame.
- Clean the surround of the active area with alcohol, using appropriate tips.

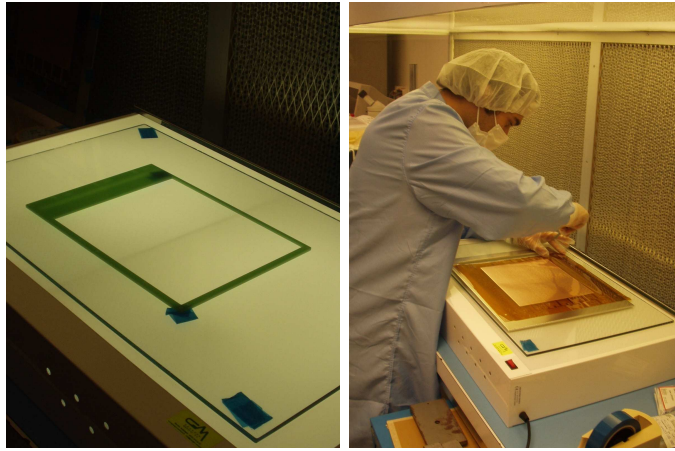


Figure 7.3: The frame is placed on the luminous table (Left), adjustment of the foil on the aluminum frame (Right).

- Superimpose the GEM foil on the frame on the table and mark the position of the fixation holes with a felt pen to help for the alignment.

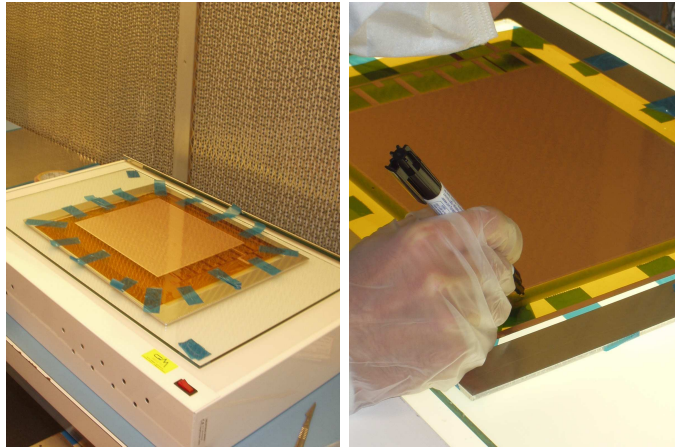


Figure 7.4: The GEM foil is stretched on the aluminum frame (Left), setting marks on the foil for the alignment (Right).

- Pour a small quantity of the two-component glue on a plastic foil and mix it with a little spatula until it gets a homogeneous texture.
- An appropriate roller should be used to spread the glue on the frames. We borrowed the roller used to glue the COMPASS GEMs, which is actually a section of a multi-layer rubber pipe. This conception gives the necessary rigidity and sufficiently preserves the suppleness of the rubber to spread the glue over a thin layer in an efficient way. Pass the roller many times in the glue to have the same amount over all the surface.
- Pass the roller many times on the four borders of the active area until the glue is spread homogeneously. This is easily checked when looking at the frame from the side with the

luminous table off and light coming from the top. A tip soaked with alcohol can be passed all around the inner surface of the frame to remove the eventual surplus of glue.

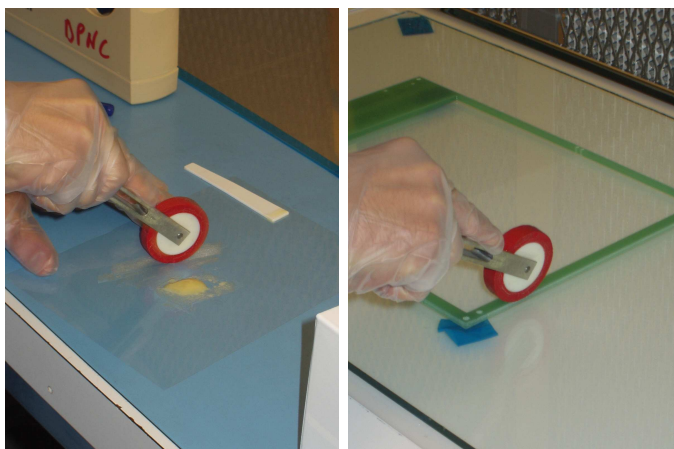


Figure 7.5: The roller is passed many times in the glue (Left), the glue is spread on the frame with the roller (Right).

- The GEM foil has to be aligned on the frame as precisely as possible from the top, avoiding horizontal displacements so that no glue is spread towards the active area of the GEM. This delicate operation is highly facilitated by the use of the luminous table that allows a quite good precision.
- Once the foil is placed on the frame, use another roller (teflon roller) to press on the foil all around the active area to be sure that the glue is uniformly spread.

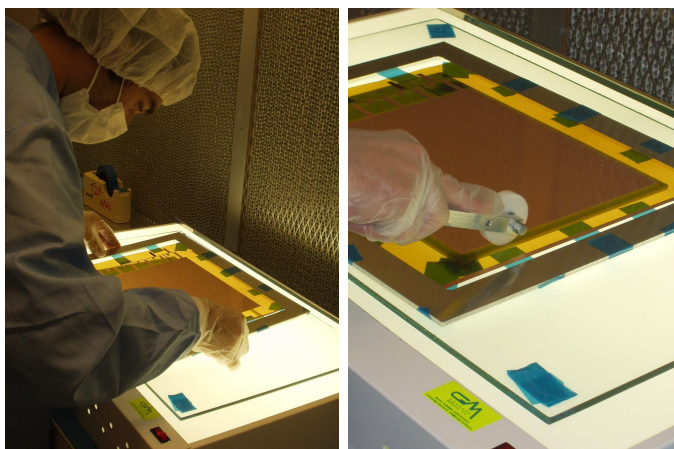


Figure 7.6: Aligement and glueing of the GEM foil on the frame (Left), a roller is used to provide a uniform glueing (Right).

- Place heavy weights on each side of the aluminum frame and let the glue dry for 12 hours. Over this drying time, the luminous table should not be let on: it seems that the dissipated heat tend to remove the blue tape strips that stretch the foil.

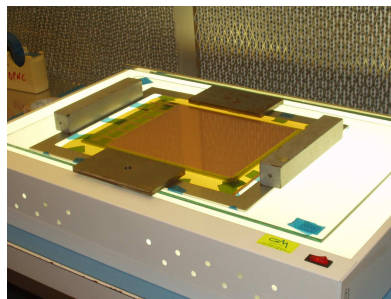


Figure 7.7: The GEM is let for drying with weights on the aluminum frame.

- Afterwards, remove the weights and directly cut the kapton foil all around the frame before removing the blue tape strips. For this operation, use a scalpel with a very sharp blade to avoid getting stuck in the foil and possibly damage the active area.
- The glueing is checked by eye, which is sufficient to see if the foil is stretched enough, and if any glue has been spread along the active area. This last point can occur when slightly aligning the foil once it is placed on the frame. It is recommended that the glue always stands far from the holes, on the inactive area of the GEM, which is about 2 mm wide.

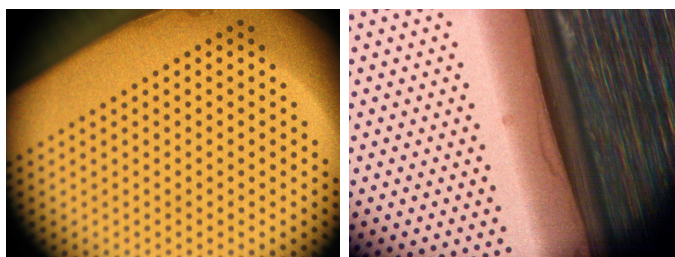


Figure 7.8: Detail of the glueing seen with the microscope. A few traces of glue can be seen on the very edge of the inactive area.

- The GEM foil glued on the frame is then tested again in the test bench and finally stored in a dry box ($T = 20^{\circ}\text{C}$ and 40% humidity) before the next operations.

7.3.3 Glueing the Guard Ring

The upper face of the guard ring was to be covered with copper. This is done by glueing a copper coated kapton foil on it. The guard ring and the kapton face of the foil are first cleaned with alcohol. The glue is then spread with the roller over the surface of the guard ring, and the kapton foil is pressed on it, using lead weights deposited on a glass plate.

After 12 hours drying, the guard ring was turned over, and the foil is cut all around the frame with a scalpel. The fixation holes are also uncovered with the scalpel, taking care of not cutting or unglueing the foil on the thin sides and corners of the frame. Finally, all the edges are polished with emery paper to get surfaces as smooth as possible, and avoid any sharp conductive pieces in the chamber.

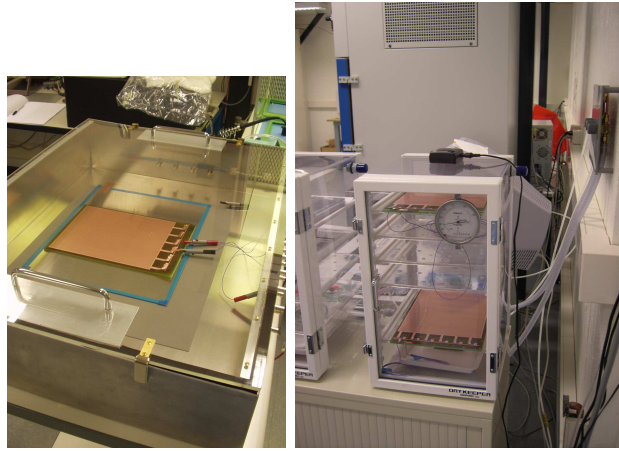


Figure 7.9: Test of the GEM glued on its frame (Left), storage in dry boxes (Right).



Figure 7.10: Spreading glue on the guard ring (Left), drying with weights (Right).

7.4 High Voltage Connections

7.4.1 Protections

To limit the current across the GEM foils (in case of a spark for example), flat rectangular ceramic protection resistors of $6,8M\Omega$ are soldered on each of the six sectors of the cathode faces (see Figure 7.12). During this operation, the frame is placed between two thin aluminum blocks on which is deposited an aluminum plate, and a long blue tape strip is used to fill the residual gap between the service area of the foil and the bottom edge of the plate. In this configuration, the aluminum plate covers the sensitive area of the GEM foil and there is no risk to damage the GEM with tin projections. The tin used for the soldering is a special tin without colophane, which is the compound responsible for the good liquefaction of the tin. The tin is first soldered on both edge on the back of the resistor, which is then placed in the right way on the foil. The resistor is thus soldered between the strip of the divider and the strip of the sector by pressing the soldering iron on each edge of the resistor until the tin melts. In this way, the solder is really limited at the edges of the resistor. After this first operation on the GEM foils, these ones are again individually tested according to the same procedure that was described before.

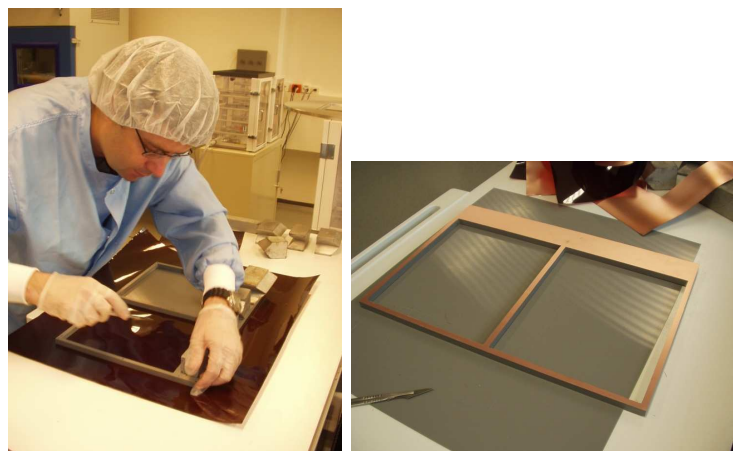


Figure 7.11: Cutting the kapton foil (Left), guard ring after the glueing (Right).

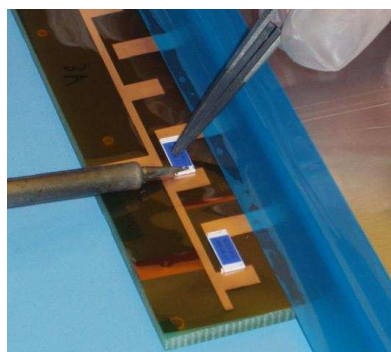


Figure 7.12: Soldering protection resistors.

7.4.2 Inner Connections

The inner connections are done by soldering cables on the copper strips respectively connected to both faces of the GEMs. These are special cables which can stand up to 8 kV. For the cathode face, the cable is directly passed through the hole of the frame and soldered on the strip. The solder should of course be as smooth as possible to fit correctly in the respective groove of the next upper frame. The task is a little bit more delicate for the anode face. For practical reasons, and to have all connections easily accessible, it is not convenient to solder under the kapton foil. To reverse the situation, an intermediate copper coated kapton strip was glued with araldite on the frame between the hole and the strip of the anode face. Thus, on one edge, the wire is directly soldered on this strip, and on the other edge, a drop of conductive glue is used to make the contact between the two copper pieces. Moreover, a point of araldite is used to glue the foil on the frame next to the strips to avoid breaking the connection by pulling on the foil. Finally a light weight is deposited on the all during 12 hours for the glue to dry. The glue that is used for the high voltage connections is called TRA-DUCT 2902 and is an electrically conducting silver-filled epoxy compound, recommended for electronic bonding and sealing applications that require a combination of good mechanical and electrical properties. This two-part, smooth paste

formulation of refined pure silver and epoxy is free of solvents and copper or carbon additives. It develops strong, durable, electrically and thermally conducting bonds and coatings between many different and dissimilar materials such as metals, ceramics, glass and plastic laminates. This glue cures at room temperature and can be used as a cold solder for heat-sensitive components where hot-soldering is impractical. Moreover, this adhesive complies with the requirements of NASA's Outgassing Specification.

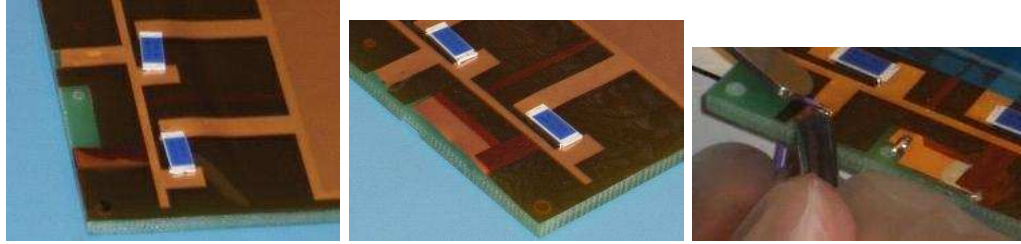


Figure 7.13: Cutting of the kapton foil (Left), placing and glueing the copper strip (Middle), soldering the high voltage cable on the strips (Right).

The GEM foils are first tested in the test bench after the preparation of the high voltage contact of the anode face, and tested another time after the soldering of the cables.

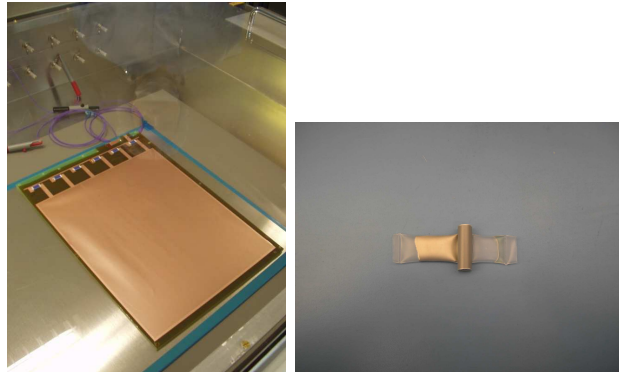


Figure 7.14: Testing the high voltage contacts (Left), the two-part conductive glue (Right).

For the guard ring, the connection is made by passing a cable through the whole tower (using the respective hole on the external side of each frame) and directly soldering it on top of the copper coated layer. This connection is only made on one side of the tower.

7.5 Stacking the Tower

The pad plane is placed under the laminar flux in such a way that the high voltage cables can be passed easily through the service area. Plastic pins are first introduced in the four central positioning holes and the first GEM is inserted via the pins on the pad plane, while the cables are pulled through the holes. For both sectors, the stacking is started with the two Left GEMs, that is the GEM foils with the high voltage strips on the left when seen from the service area. Once the first layer is placed on the pad plane, it is blown with the nitrogen ion gun and the two

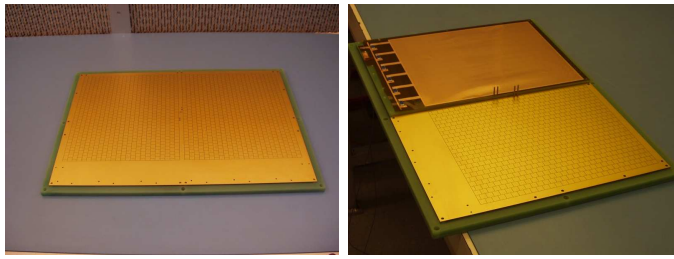


Figure 7.15: Pad plane and PCB support (Left), first GEM placed on the pad plane (Right).

next frames are piled up, passing the cables through the previous layer and PCB support, and checking that the soldered joints and resistors fit correctly in the service area of the frames.

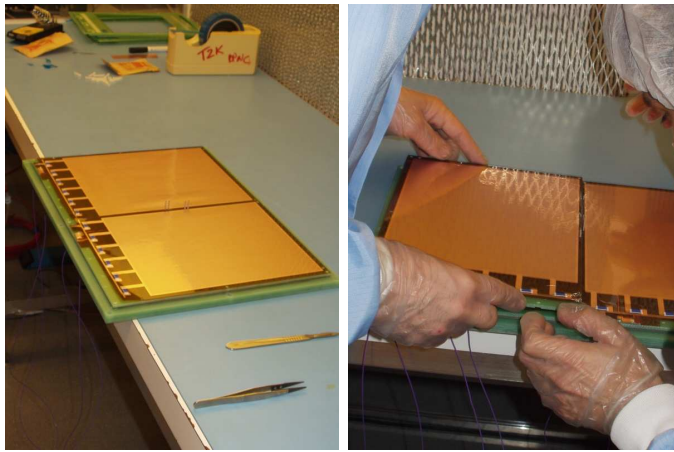


Figure 7.16: First layer on the pad plane (Left), piling up (Right).

The third layer is finally piled up passing the cables through the two previous layers.

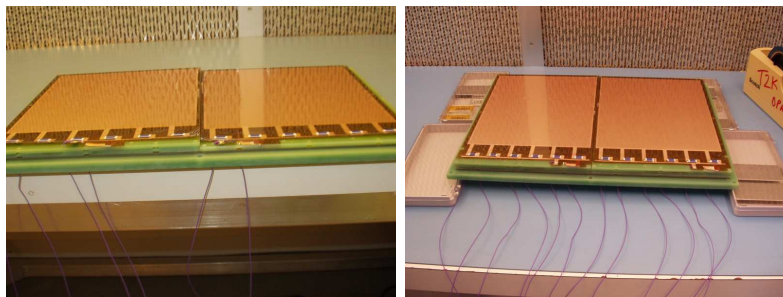


Figure 7.17: Second layer (Left) and complete stack (Right).

Once the three layers of GEMs are placed on the pad plane, the tower is introduced in the test bench and tested GEM by GEM. Afterwards, the guard ring is inserted via the plastic pins on top of the tower and fixed with the 2.5 mm diameter nylon screws, so that the all structure is

tightly fixed on the PCB support. After this last operation, the complete tower is tested again GEM by GEM.

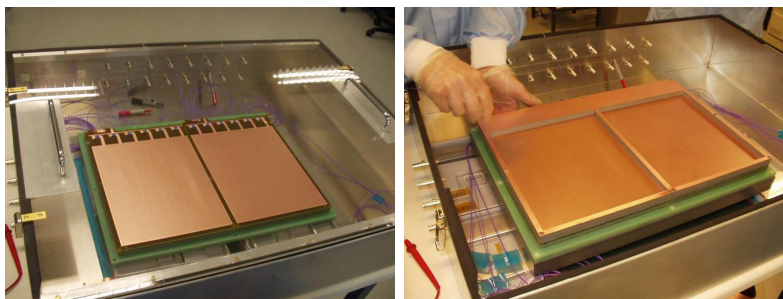


Figure 7.18: Testing the tower (Left), test of the tower with the guard ring (Right).

7.6 Mounting the Flanges

7.6.1 Mounting the Tower on the Detector Flange

The first step is to fix the PVC spacer on the detector flange. The respective o-ring of the flange is covered with vacuum grease and placed in the groove around the aperture. The PVC spacer is then positioned on the flange and screwed from the external face with 3 screws per side. Actually this number turned out not to be sufficient to provide an excellent gas tightness: the PVC has a certain flexibility and the o-ring can not be perfectly pressed over all its length with this number of screws.

Then, the o-ring of the spacer is also covered with vacuum grease and placed in its groove along the internal edge of the spacer. The GEM tower is positioned on the PVC spacer and the PCB support is fixed on it with three 3 mm diameter nylon screws per side. For the same reasons as before, this number should be increased.



Figure 7.19: The tower is fixed on the detector flange.

The top surface of the GEMs is finally protected with a PVC foil fixed on the tower with blue tape strips, and all the high voltage cables are grouped together and fixed on the backside of the PCB support. Figure 7.20 shows a drawing of the final stack.

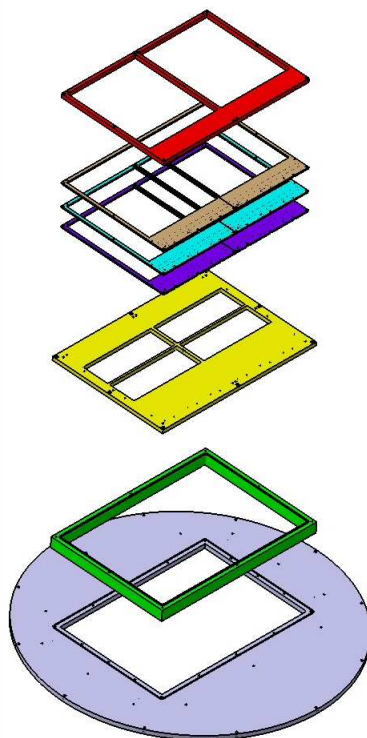


Figure 7.20: Complete stacking of the detector.

7.6.2 Mounting the Detector on the HARP Chamber

The transport of the detector to CERN is done by truck in one of the aluminum container used for the transport of the inner silicon tracker of the AMS experiment produced by the University of Geneva. The detector, fixed on its flange, is first wrapped in a teflon foil and then carefully placed on a thick layer of foam covering the bottom of the container.



Figure 7.21: Transporting the detector to CERN.

Once at CERN, the protection endcap of the chamber is removed and the o-ring of the adaptative ring is covered with vacuum grease before being lodged in the groove. The detector flange is then fixed on the ring: two persons are holding it on both sides and aligning the fixation holes, while a third person is screwing the flange. The flange should always be carried during this operation, so that the screws fit correctly in the holes.



Figure 7.22: HARP chamber with the endcap (Left), the field cage (Middle), fixation of the detector flange (Right).

After the fixation of the detector flange, it appeared that a drilling mistake was done during the manufacturing of the flange and the detector was finally deviated of 10° to 15° from the vertical position.

As for the gas inlets of the GEMs, the high voltage connectors of the anode faces could not be screwed in the PCB support and the holes were filled up with silicon paste around the cables. The chamber was finally flushed with gas in order to test and improve the gas tightness.

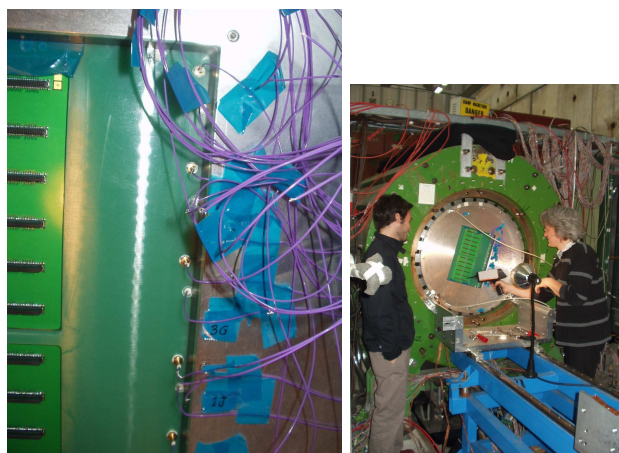


Figure 7.23: The high voltage connectors (Left), checking gas leakages with the sniffer (Right).

Chapter 8

Run Conditions

8.1 First Run Conditions

8.1.1 Gas Choice

The gas characteristics and properties to be fulfilled for the ND280m TPC have been abundantly discussed in many reports ([3], [13]) and are until now still under considerations. Really basic facts such that, the diffusion of drifting electrons can limit the intrinsic space point resolution and that the ND280m TPC will be operated at 0.2 T (or 0.15 T) magnetic field, highly recommend the use of low diffusion gases and rule out the use of pure fast gases. It appears then, that a gas mixture including CO_2 (slow gas with low transverse diffusion), is a natural baseline choice. For example, properties of $ArCO_2$ gas mixtures, are presented in Figure 8.11, where the drift velocity and transverse diffusion are plotted as functions of the electric field.

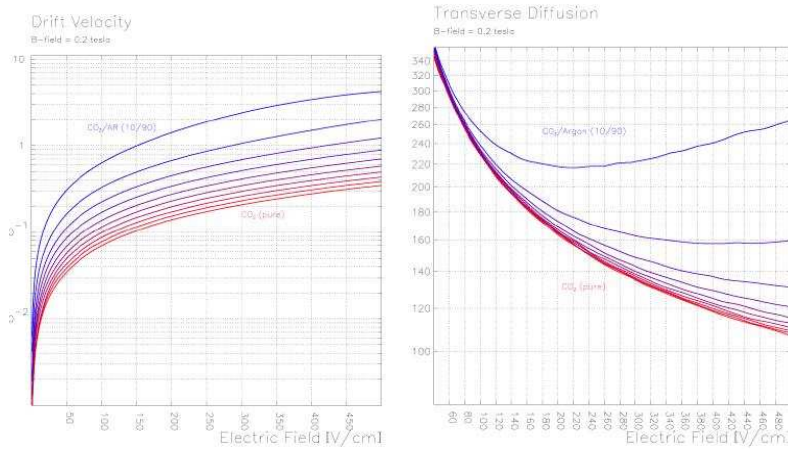


Figure 8.1: Drift velocity in $[cm/\mu s]$ (Left) and transverse diffusion in $[\mu m/\sqrt{cm}]$ vs the electric field at 0.2 T for different mixtures of $ArCO_2$ [3].

For the first measurements, it was decided to test a gas mixture of $ArCH_4$ (95 : 5), usually called P5, before testing commonly preselected gas mixtures (see Figure 8.2), since it is a quite simple gas, not very sensitive to attachment and magnetic field.

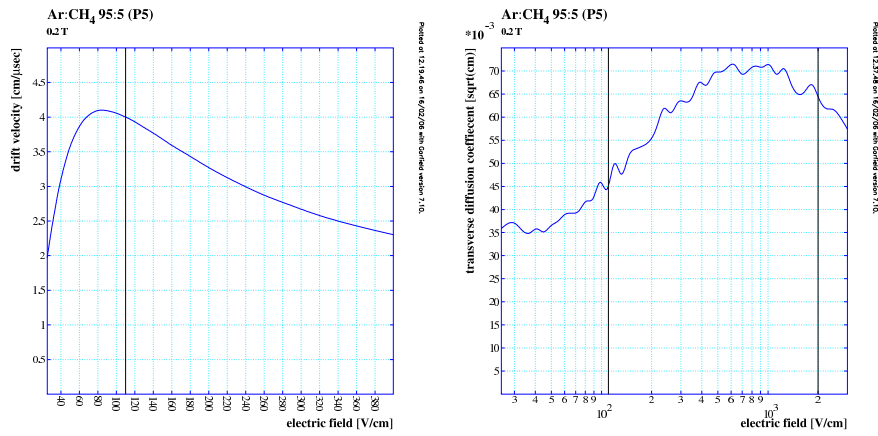


Figure 8.2: Drift velocity in [cm/ μ s] (Left) and transverse diffusion in [μ m/ \sqrt{cm}] vs the electric field for P5 at 0.2 T.

The vertical black line shows the drift field value (110 V/cm) used during the runs. Figure 8.3 also shows the transverse diffusion as a function of the electric field but on a smaller scale.

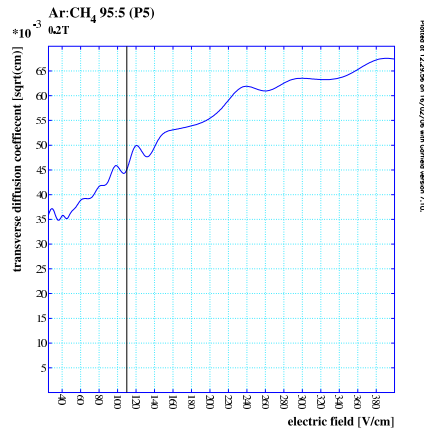


Figure 8.3: Transverse diffusion in [μ m/ \sqrt{cm}] vs the electric field for P5 at 0.2 T.

From Figure 8.2, it can be seen that the drift velocity is quite large (around 4 cm/ μ s) at the operating field value and located close to the maximum, so that it is not too sensitive to field fluctuations. The transverse diffusion is however quite large (around 450 μ m/ \sqrt{cm}).

8.1.2 Measurement Conditions

Nominal Settings of the Detector

Here we present the nominal settings of the detector. Before this final configuration was established, the GEMs have been slowly trained, increasing the operating voltages, induction, transfer and drift fields step by step. The geometrical setup is schematically described in Figure 8.4 and gives almost all informations to determine the relations between the voltages to apply to the cathode, first strip and the first GEM (face 3C) and the respective drift field.

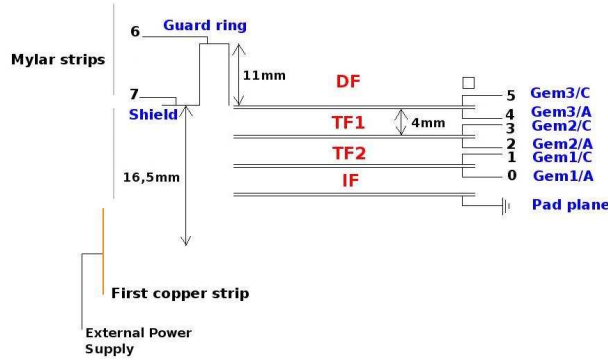


Figure 8.4: Nominal geometrical setting.

These relations are shown to be:

$$\begin{cases} HV_c = 155.1 \times DF + HV_{3C} \\ HV_{fs} = HV_{3C} - 1.65 \times DF \end{cases}$$

where, HV_c stands for high voltage on cathode, HV_{3C} for high voltage on GEM3C, HV_{fs} for high voltage on first strip and DF for drift field (given in $[\text{cm}/\mu\text{s}]$). For the voltage to apply to the guard ring, it can be shown that:

$$HV_{GR} = HV_{3C} + 1,1 \times DF \quad (8.1)$$

The numerical factors are coming from the geometry of the field cage (11 mm wide mylar strips) with 141 strips between the first GEM (3C) and the cathode and 1.5 strip between the first copper strip and the first GEM.

The nominal voltage setting in the *Data taking* working point is summarised in Table 8.1.2 and gives voltages and current limitations for each element of the detector.

In this table, the trip time is set to 0.2s for each channel of the SY127. I_C and I_{fs} are not current limitations but the real currents through the cathode and first strip respectively to the indicated voltages, and their sum should be equal to $430 \mu\text{A}$.

To avoid any permanent damage on the field cage, the voltage of the cathode is limited to 27 kV. Using the previous relation for the voltage of the first strip, we find that it should normally be 3.129 kV instead of 3 kV. The reason of this limitation will be explained in a following section. These voltage setting is more or less what the XTC program computes for each channel in order to satisfy the predefined GEM operating values, induction, transfer and drift field values, that are summarised in Table 8.1.2.

	Voltage [kV]	Current [μA]
Cathode	25	I_C
First strip	3	I_{fs}
GEM1A	0,8	1,2
GEM1C	1,11	1,2
GEM2A	1,91	1,2
GEM2C	2,22	1,2
GEM3A	3,02	1,2
GEM3C	3,33	1,2
Guard ring	3,451	1,2
Shield	3,33	1,2

Table 8.1: Nominal voltage setting in *Data taking* working point for P5.

ΔG	310V
Δ	800V
DF	110V/cm
TF1	2000V/cm
TF2	2000V/cm
IF	2000V/cm

Table 8.2: Nominal fields setting in *Data taking* working point for P5.

where ΔG is the voltage difference between the faces of the GEMs and Δ is the voltage difference between two successive GEMs. In the first run, ΔG was actually limited to 310 V, due to stability problems.

In the *Pedestal run* working point there must be no amplification in order to compute pedestals and noise of each channel. To avoid ramping down and up the all system, which is quite a long process ($v_r = 10$ V/s), this is simply done by applying a lower voltage difference to the first GEM (3 A/C). The respective voltages and field settings are summarised in Table 8.1.2 and Table 8.1.2.

Measurements with Magnetic Field

For this first run period, current was still available for the magnet and we took data with different field configurations:

- 0.2 T. For this mild field value, a plate was simply placed on the aperture of the magnet to avoid that any screws or metallic pieces hanging about in the area eventually damage the detector.
- 0.4 T. This field value requires the closing of the magnet. This is a very delicate operation since it requires a very meticulous cabling of the detector, so that no cable is severed when inserting the endcap in the aperture of the magnet with a crane.
- 0.7 T. Allmost no data were taken in this configuration. Actually, the chamber was not fixed to the structure of the magnet, and the presence of a few slightly magnetic screws on the detector flange and the electronics mechanical support, was enough to displace the

	Voltage [kV]	Current [μA]
Cathode	25	I_C
First strip	3	I_{fs}
GEM1A	0,8	1,2
GEM1C	1,11	1,2
GEM2A	1,91	1,2
GEM2C	2,22	1,2
GEM3A	3,02	1,2
GEM3C	3,12	1,2
Guard ring	3,241	1,2
Shield	3,12	1,2

Table 8.3: Nominal voltage setting in *Pedestal run* working point for P5.

$\Delta G1A/C$	310V
$\Delta G2A/C$	310V
$\Delta G3/AC$	100V
Δ	800V
DF	110V/cm
TF1	2000V/cm
TF2	2000V/cm
IF	2000V/cm

Table 8.4: Nominal fields setting in *Pedestal run* working point for P5.

all chamber in the magnet and press the electronics against the endcap generating a gas leakage.

8.1.3 First Results

Electric Field Distortions

This first run period produced very few exploitable data because of two main reasons:

- A lot of time and effort were devoted to debug the electronics and make the system run with 12 boards. This considerably reduced our data taking time to three days.
- The detector could not be operated in stable conditions. Actually, a quite regular rate of two to three trips per hour was observed, always located on the first layer of GEMs.

Nevertheless, it was possible to run the detector at the very first time, and to observe quite quickly the first tracks using the HARP Event Display.

As can be seen on the event displays of Figure 8.5, the electric field distortions in the xy plane are quite important and completely distort the tracks at the edges of the guard ring. These particular S-shaped distortions are mainly the result of geometrical effects:

- The asymetry of the guard ring: on the service side it has a width of 50 mm for only 8 mm on the other side.



- The guard ring has a rectangular geometry and is inserted in a field cage with a circular geometry.
- The guard ring is not centered on the anode plane of the chamber so that the active area of the detector is centered.

The screenshot shows the Run422 Event 32 interface. On the left is a control panel with various settings: Backdoor (Top), Lock (Right), Print (Dist), All Views, Background live, ZOOM in/out, Geometry ON, Axis OFF, Histo OFF, MCTraj ON, MCTrajectory OFF, MCTrajectory OFF, Trajectory OFF, TPC from Hist OFF, TPC Clusters ON, Dead OFF, Heavy OFF, Nuclear Cycle ON, Trigger Pattern ON, and Power/LIT. The main area displays a large grid of event data, likely a hit map or spectrum, with a red vertical line indicating a specific feature. The title bar at the top reads "Run422 Event 32".

Figure 8.6: S-shaped tracks in the xy plane (Left), C-shaped tracks in the z direction (Right).

In the usual course of an experiment, the simulation of the detector is an important aspect of the *R&D* in order to understand its performance and eventual problems. Due to a very tight schedule, this work was not of the highest priority and electric field simulations were performed after the event to get a better understanding of the distortions that were observed.

Master Thesis by N.Abgrall, February 2006

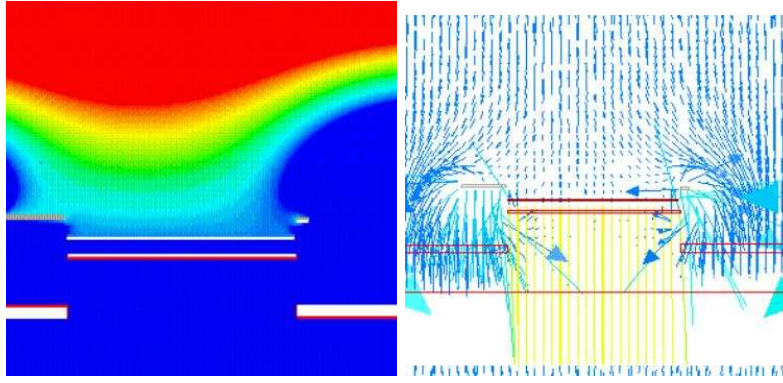


Figure 8.7: Potential (Left) and electric field simulations (Right).

ring which is much larger on the left side. The navy blue represents 3300 V and the red is for 3800 V.

In this initial configuration, the GEMs are positioned on the first mylar strip thanks to the PVC spacer and the detector flange is grounded: this means the field goes from 110 V/cm in the drift volume to approximately 600 V/cm over the last 5 cm. During this first run, only the first strip was actually connected to the external power supply and the two other strips were floating. As can be seen on the simulation for this configuration, the detector flange, which has direct view in the chamber, deeply influences the potentials in the drift volume next to the guard ring, thereby generating huge distortions, especially on the small side of the guard ring.

This directly results in the field lines distortions simulated on the right picture of Figure 8.7. It is clearly visible that, on each side of the guard ring, the field lines are deviated towards the huge ground that represents the detector flange. Only a very restricted central area on the GEMs is not affected by this effect, which can explain the two kinds of distortions mentioned before:

- When a track crosses a sector from one side to the other, charges follow the drift lines towards the GEMs where they are collected. However, charges that are drifting close to the edges of the guard ring follow lines that are deviated towards the ground plate (about 6 cm below) in such a way that the projection of this deviation on the xy plane is perpendicular to the edges of the guard ring. These effect results of course in a loss of charges for collection at the edges of the sector, and explains the S-shaped distortions of the tracks in the xy plane.
- The C-shaped distortions in time are directly related to this first effect. Actually, the charges that follow the deviated drift lines at the edges of the sectors are automatically collected later than the charges in the central region, since their drift distance is elongated. This delay in the collection of charges is then interpreted as a longer distribution of charges in the z direction during reconstruction.

8.2 Second Run Conditions

8.2.1 A Solution to Field Distortions

Potentials Simulations

The idea to eliminate the electric field distortions was to create a new plane of reference to define uniformly the potential at the level of the GEM surface, over the entire cross section of the chamber. This was first simulated with a 1 cm gap between the plane and the tower, as shown in Figure 8.8.

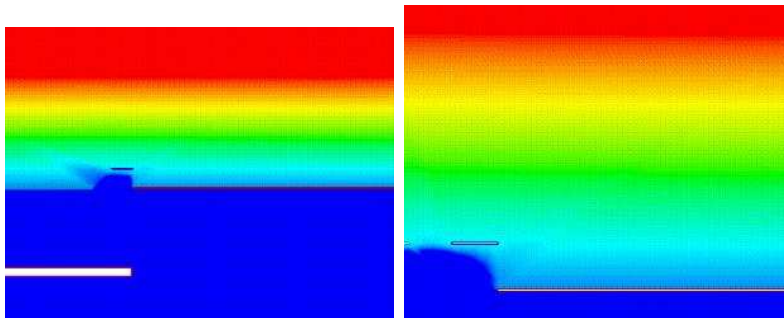


Figure 8.8: Potential simulations adding a new reference plane (Left). Detail of the simulation (Right).

In the simulation, the reference plane is placed at the level of the first GEM, but the relative position in z is not that much important, as long as the right potential is fixed. Slight potential anomalies can be observed near the guard ring: these are due to calculation artefacts of the underlying mesh and are not relevant. The electrostatic configuration is clearly improved by the presence of the reference plane.

The Guard Shield

In order to perform the required modifications, the detector was transported back to the University of Geneva in the clean room. The complete tower was tested again in the test bench, this time layer by layer, in order to keep the high voltage connections in the operating conditions. The new voltage reference plane, that we will from now on call the *shield*, is physically manufactured as a 3 mm width circular PCB with the upper face coated with 35 μm of copper. It has a rectangular apperture in order to be inserted around the tower, and covers almost the entire cross section of the drift volume: the gap between the internal edge and the tower has been reduced to 2 mm and the distance from the external edge to the respective mylar strip is less than 2 cm (see Figure 8.9).

In order to be placed at the level of the first Gems, the shield is fixed with nylon screws on four PVC bars of the respective height, fixed on the detector flange in such a way that the gas distribution flows as freely as possible.

A new hole has been drilled on the service side of the detector flange to lodge an SHV connector for the high voltage connection of the shield. A cable is first soldered on the connector, passed through a small hole in the shield and soldered on the copper coated face. After the installation of the shield, the detector was transported again to CERN to be mounted on the field cage.

It was realised then, that due to the small distance between the external edge of the shield and

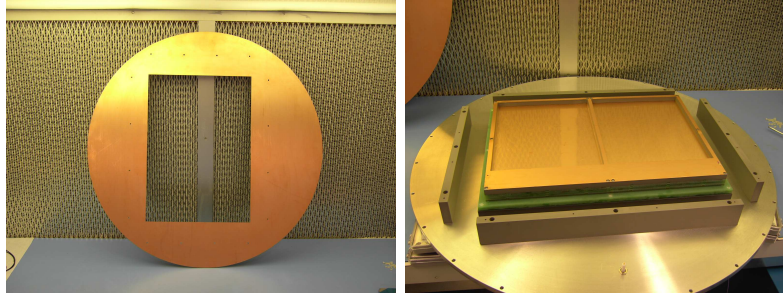


Figure 8.9: The shield (Left) and its support structure fixed on the detector flange (Right).

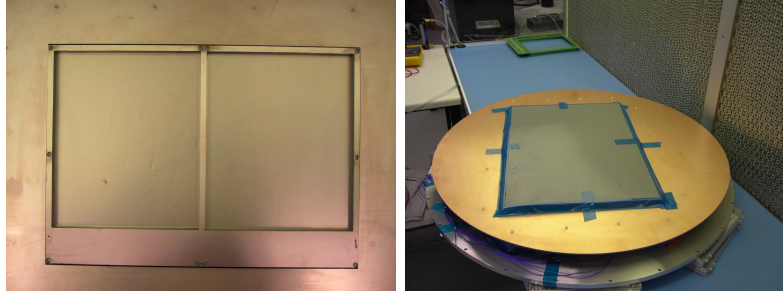


Figure 8.10: Top view of the tower with the shield (Left), GEMs are protected before transport to CERN (Right).

the mylar strips, there could be a risk of sparks in the case where the shield is at potential zero (all channels are set to zero when there is a trip for example) and the first strip remains at 3 kV. To resolve this problem, it was thought in a first time to connect the first copper strip to the power supply of the GEMs. This option actually has two main problems:

- All the copper strips are connected via the central rod and this represents a huge capacitance that can not be filled with the standard module (A431 8 kV/200 μA) used with the SY127. This has to be replaced by a module with higher current limitation such as Mod.A333, 4 – 3 kV/2 – 3 mA, with which the current was set to 2000 μA .
- With this setting, the power supply was able to ramp up the system, as long as there was no voltage on the cathode. Actually, as soon as the cathode is under voltage, the current backflow through the strips towards the power supply is too high to be automatically regulated, and every channel is just set to zero. In this configuration, the system could simply not be ramped up.

The only way to operate the system was to let the strips connected to the external power supply of the TPC. In this way, there would inevitably be a voltage difference of approximately 3 kV between the mylar strip and the shield in case of a trip. Though risky, it was finally decided to test the system, and ramp up the strips with the shield to ground. It appeared that the system could stand a difference of 3 kV without any problems, and this is the reason why the voltage is limited to this value in the nominal voltage setting of the detector.

8.2.2 Gas Choice

For this second run, it was decided to test one gas mixture of $ArCO_2$ (90 : 10). As can be seen on Figure 8.11, the drift velocity in this mixture at the operating field value is much lower (a bit less than $1\text{cm}/\mu\text{s}$) than in the $ArCH_4$ mixture.

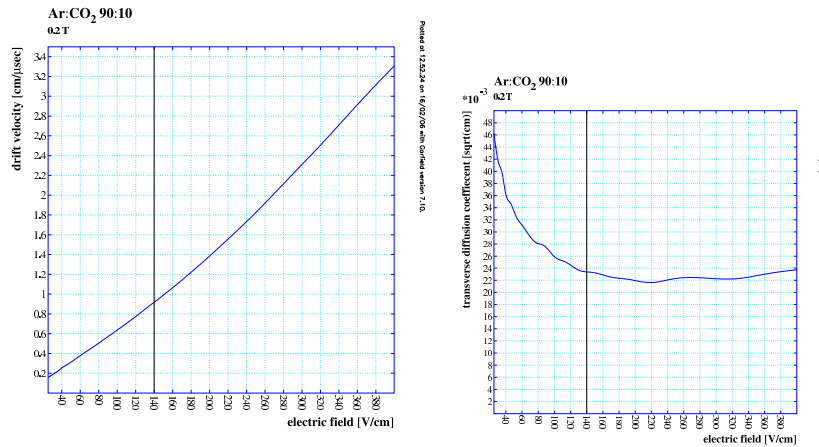


Figure 8.11: Drift velocity in $[\text{cm}/\mu\text{s}]$ (Left) and transverse diffusion in $[\mu\text{m}/\sqrt{\text{cm}}]$ (Right) vs electric field for $ArCO_2$ (90 : 10) at 0.2 T.

Figure 8.12 shows the transverse and longitudinal diffusions versus the electric field. One can see that $ArCO_2$ is a lower diffusion gas mixture than $ArCH_4$ (around $230 \mu\text{m}/\sqrt{\text{cm}}$). Another important difference between the two gas mixtures is the sensitivity to attachment, that is an extremely critical parameter in $ArCO_2$. With the first gas mixture, only 2 to 3 days were necessary to get a good gas quality, whereas almost 5 to 6 days are required for $ArCO_2$.

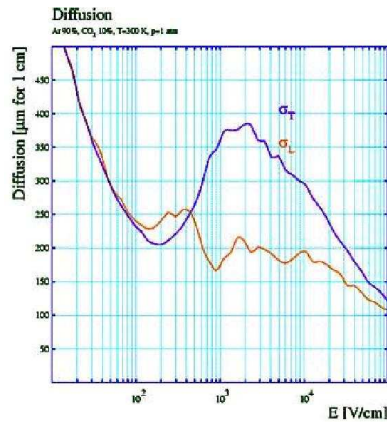


Figure 8.12: Longitudinal and transverse diffusion in $[\mu\text{m}/\sqrt{\text{cm}}]$ vs electric field at 0 T for $ArCO_2$ (90 : 10).

8.2.3 Nominal settings

The nominal voltage and filed settings in the *Data taking* working point are summarised in Table 8.2.3 and Table 8.2.3.

	Voltage [kV]	Current [μA]
Cathode	25	I_C
First strip	3	I_{fs}
GEM1A	0,8	1,2
GEM1C	1,12	1,2
GEM2A	1,92	1,2
GEM2C	2,24	1,2
GEM3A	3,04	1,2
GEM3C	3,36	1,2
Guard ring	3,514	1,2
Shield	3,36	1,2

Table 8.5: Nominal voltage setting in *Data taking* working point for $ArCO_2$.

ΔG	320V
Δ	800V
DF	140V/cm
TF1	2000V/cm
TF2	2000V/cm
IF	2000V/cm

Table 8.6: Nominal fields setting in *Data taking* working point for $ArCO_2$.

The nominal voltage and field settings in the *Pedestal run* working point are summarised in Table 8.2.3 and Table 8.2.3.

	Voltage [kV]	Current [μA]
Cathode	25	I_C
First strip	3	I_{fs}
GEM1A	0,8	1,2
GEM1C	1,12	1,2
GEM2A	1,92	1,2
GEM2C	2,24	1,2
GEM3A	3,04	1,2
GEM3C	3,14	1,2
Guard ring	3,294	1,2
Shield	3,14	1,2

Table 8.7: Nominal voltage setting in *Pedestal run* working point for $ArCO_2$.

$\Delta G1A/C$	320V
$\Delta G2A/C$	320V
$\Delta G3/AC$	100V
Δ	800V
DF	140V/cm
TF1	2000V/cm
TF2	2000V/cm
IF	2000V/cm

Table 8.8: Nominal fields setting in *Pedestal run* working point for $ArCO_2$.

8.2.4 Measurements with the Iron Source

During this second run, a $^{55}_{26}Fe$ source was placed at the center of the cathode plane. It is a small metallic disc of approximately 4 cm diameter, that can be placed in a central circular apperture of the aluminum endplate where the mylar foil is visible. The source emits photons of 5.9 keV and 6.49 keV. The analysis of the spectra of the source allows a good calibration of the detector. Results related to the iron source will be given in the third part of this report.

8.2.5 The Breakdown

Unfortunately, six days after the installation of the shield, a short circuit occurred after a trip on the first layer of GEMs. After inspection it appeared that the short was only on the upper sector of the detector. Due to a very tight schedule at this moment and the amount of time required for the fixation of such a problem, it was decided to continue data taking for ten more days with only one sector.

Afterwards, the detector was once again transported back to the clean room for a meticulous inspection. The trip that caused the short occurred while the system was ramping up the induction field; this means that the only voltage difference in the detector at this moment, was between the pad plane and the anode face of the first GEM. This last point restricted our investigations to this part of the tower. Anyway, the tower was carefully dismantled and every GEM has been tested again successfully in the test bench.

As far as the suspicious GEM (1F) is concerned (see Figure 8.13), a first test with the multimeter confirmed the short on the most right sided sector of the cathode face. The GEM was then placed in the test bench, and could actually be ramped up again and stand a voltage difference of 500 V. We suppose that a particle creating the short, was removed while handling the GEM.

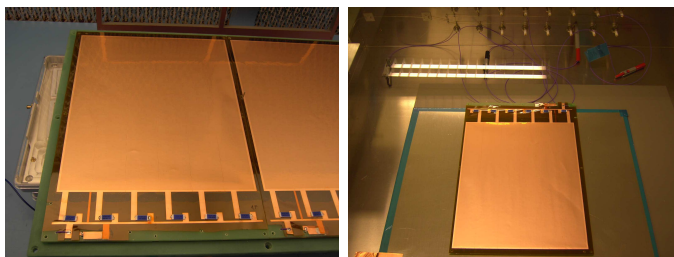


Figure 8.13: The suspicious GEM on the left sector of the pad plane (Left), test of the GEM in the test bench (Right).

An optical inspection revealed an area of a few square mm on the anode face, where the copper coating completely melted. It can also be seen in Figure 8.14 that a certain number of holes with abnormal diameters are distributed around this particular area, suggesting an original etching defect of the chemical process.

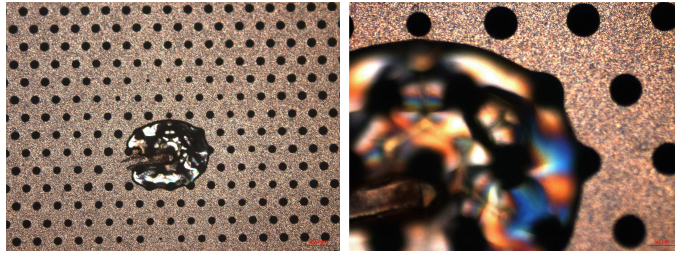


Figure 8.14: View of the anode face of the GEM with the microscope (Left), detail (Right).

As for the padplane (see Figure 8.15), an optical inspection showed a few damaged pads and one pad in particular with a more important hit on it.

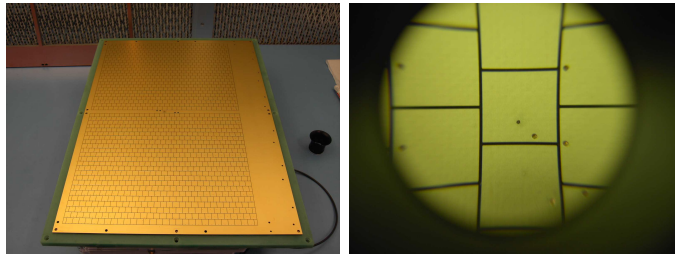


Figure 8.15: Pad plane without GEMs (Left), detail of a damaged pad (Right).

After these inspections, the suspicious GEM was replaced by a spare one for the same sector. Actually, the new GEM was an M-GEM and not an L-GEM so that the high voltage cables for this GEM and the next one have to pass through the same holes. The respective holes on the frame and the pad plane were then drilled again a little bit larger. Afterwards, the tower was pilled up again and tested once more layer by layer, before being fixed on the flange, equipped with the shield, protected and transported back to CERN. It appeared then, that the detector could be operated in perfectly stable conditions (no trips) with the GEMs ramped up to 320 V, demonstrating that GEM 1F was clearly the source of instability of the previous run.

It is quite difficult to draw clear conclusions from these investigations, but nevertheless, some assumptions can be advanced:

- The region of the GEM with the concentration of holes with abnormal diameters is not usual and could be related to the instability of the GEM, turning out to be critical in run conditions.
- For this reason, many repetitive sparks could have occurred in this particular region, leading to the observed damage. It seems actually a bit strange that only one spark can cause such damage. Moreover, a spark usually produces black spots that were not observed during the inspection.

- A particle could have been introduced between the GEM and the pad plane, either while stacking the tower or, more probably, via the gas system of the GEMs.

8.2.6 Improvements of the Testing Procedure

In any case, this incident can only urge us to draw a certain number of conclusions in order to improve our testing procedure for an eventual future production:

- A preliminary optical check of the foils should be systematically done, and the requirements clearly determined.
- The GEMs should be tested in Argon instead of Nitrogen, if an Argon mixture is to be the operating gas of the TPC.
- It should be possible to test the complete module at the same time in the test bench.
- It should be possible to test the tower with an iron source in the test bench in order to inject real charges in the system and eventually do calibration measurements.

A few last considerations seem essential to close this chapter:

- A very large amount of experimental studies with GEMs showed that the latter are **extremely stable systems** in proper conditions. After the replacement of the bad GEM, the tower was absolutely stable. The incident that occurred is certainly due to an omission in the testing procedure, and is not expected to happen again in a clearly defined large-scale production.
- The prototype has undergone a lot of handling, transport and modifications, and finally proved to be **very robust**.
- The prototype was designed to be as **light and modular** as possible, and these qualities turn out to be essential in case a fixing is necessary. Actually, **only two persons during two days** (not full day time) were required to repair and mount back the detector on the chamber after the incident.

8.3 Third Run Conditions

8.3.1 General conditions

- For this run, the field cage was still operated with the $ArCO_2$ (90 : 10) gas mixture.
- Most of the data acquisition was done with the iron source.
- Data were taken with three different delays of the trigger: 75, 85 and 95 μs .
- GEMs could be ramped up to 330V.

8.3.2 Improvements

Protection of the GEMs

To protect the anode faces of the GEMs, pairs of $1M\Omega$ resistances were soldered in the high voltage box on the respective SHV connectors, so that each GEM is connected to a resistance.

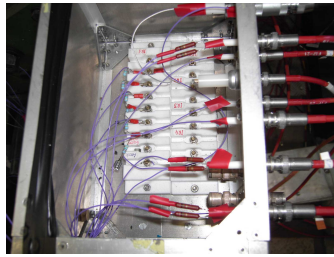


Figure 8.16: Protection resistors in the high voltage box.

Insulation of the Shield

To avoid any risk of sparks between the shield and the mylar strips, the external edge of the shield has been covered with a layer of blue tape.

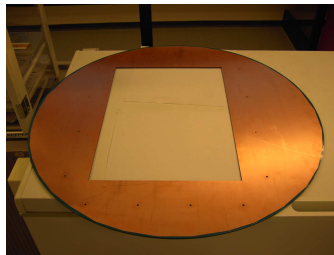


Figure 8.17: The external edge of the shield insulated.

Part III

Performance Study

Chapter 9

Overall Framework

9.1 The HARP Software

As we already mentioned, the running sessions of the prototype took place at CERN using the previous facilities of the HARP experiment, that is, the experimental area, the magnet and field cage, and the control rooms. The idea came about quite naturally then, that the HARP software could also be used for the data acquisition and reconstruction. These two parts of the software are the topics of the next sections. In this section, we briefly introduce the simulation part and try to stress out the possibilities to adapt the code for a full simulation of the T2K prototype.

9.1.1 The HARP TPC Simulation Software

The simulation of the HARP TPC is realised by using the GEANT4 toolkit within the GAUDI framework: a set of GAUDI algorithms create and act on various objects in the event model stored in the GAUDI transient store. The simulation consists more or less in two steps: first are simulated the physics processes, that is, from the generation of drift electrons along the track of a particle till the signal they will deposit in the wire chamber of the TPC, and second is simulated the readout electronics (sampling, digitisation and packing). Once the complete chain is performed, the simulated data are available in the same format as real data, and both sets are unpacked and reconstructed with the same software.

The HARP software is organised in various packages dedicated to different tasks. A rough schematic description of some packages interdependency is given in Figure 9.1. The *HarpDD* (for Detector Description) and *HarpEvent* packages contain the geometry and physics classes respectively. These classes are filled and acted on by different algorithms from the *DetRep* (for Detector Representation) and *DetResponse* packages, that respectively construct the geometry of the detector and the physics objects. All the parameters required by these algorithms are read from the *DataFile* package. The complete simulation chain, except the initial Geant4 steps and the packing of the data, is contained in the previous packages. The packing/unpacking and reconstruction of the data are respectively contained in the *ObjectCnv* (for Object Converter) and *Reconstruction* packages. The *HarpUI* (for HARP User Interface) package is dedicated to the visualisation of the detector and reconstructed events with the HARP Event Display. Finally, all the algorithms for the data analysis and Ntuples production are stored in the *Analysis* package.

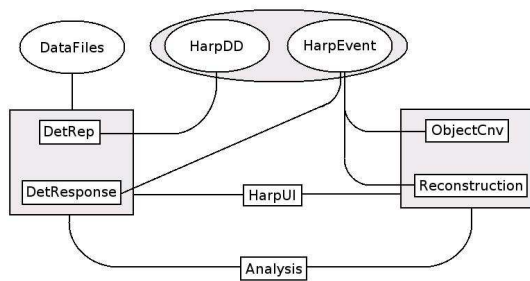


Figure 9.1: Schematic overview of the HARP software.

9.1.2 HARP Software and Prototype Simulation

The HARP software was designed for a more complex setup, but its organisation in many packages makes it easy to handle. Pieces of code can be modified more or less independently. This is an important aspect that can highly facilitate the adaptation of the code for the T2K prototype simulation.

The complete HARP simulation chain can be summarised in a few key points, as shown in Figure 9.2:

- Generation and propagation of drift charges
- Drift charges avalanche at the anode wires
- Pad Response Function (PRF)
- Electronics response and amplification
- Digitisation
- Packing of the data

The first point concerning generation and propagation of drift charges relies on the initial Geant4 steps and does not require any modifications. The only changes would concern gas parameters such as the mean energy required for the creation of an electron-ion pair, the drift velocity or the transverse and longitudinal diffusion coefficients that are just directly read from a parameter file.

The second point concerns the amplification of the drift charges through the avalanche at the anode wires. This part of the simulation obviously requires the complete modification of the amplification system implementation. The modification requires the clear understanding of the amplification process through a tripple GEM structure and could certainly be deeply inspired by the already advanced and remarkable work of the ILC TPC Group Aachen from the IIIrd Physics Institute of the RWTH Aachen. The pad PRF should be worked out in parallel with the amplification, since it may depend on the width of the charge cloud after amplification too.

For the fourth and fifth points, a few modifications are required, since the order, rising and shaping times of the transfer function of the HARP electronics can simply be replaced by the transfer function charateristics of the PASAs of the FECs, used for the T2K prototype electronics. Other modifications would only concern a few specific parameters such as the conversion gain, the output dynamic range or the ADC per volt number.

As far as the last point is concerned, mainly two aspects would require some modifications: on

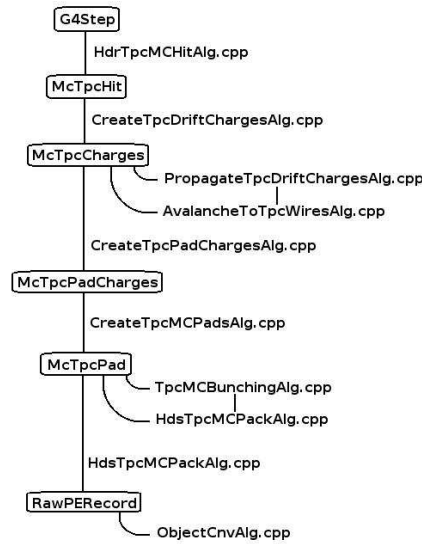


Figure 9.2: Schematic diagram of the HARP simulation chain.

one hand, the way the bunching of the ADC/time series is done (that is specifying some characteristics such as the ADC threshold, the minimal number of sample above threshold or the number of pre- and post-samples), and on the other hand the format of the packed data.

The adaptation of the HARP simulation code for the T2K prototype would require the modifications that we have just briefly described, and seems reasonably feasible. The full simulation of the prototype could be a useful tool in order to understand the data, and could even be compared to HARP independent simulations.

9.2 The Data Acquisition System, DAQ

9.2.1 Building the DAQ

The HARP DAQ software is actually based on the ALICE experiment data acquisition prototype software, called DATE. The main code is contained in the *equipementlist_TEST.c* file in the *date_site/readout* directory. In this file is defined the complete configuration of the data acquisition, calling specific functions of the Altro chip via the U2F communication protocol.

To speed up the data acquisition process, it is convenient to have the DAQ run in *push mode*. In this mode, the electronics sends the data to the readout when it is available. This implies changes in the DAQ code that has to run asynchronously with respect to events, and changes in the configuration of the boards. A large piece of memory is allocated in this mode: the electronics fills it with data and once the buffer is filled, it tells the DAQ that the data is available. The DAQ then copies the data into local memory.

To improve the performance, the time delay for the wait process in the driver was also changed (in the *altro_usb/u2f* directory). The main problem is that when the zero-suppression mode is used, the amount of data is small and, at a rate of a few Herz, it takes a long time to fill the buffer and publish it to the DAQ process. Sometimes the driver timed out before there was enough data to fill the temporary buffer. This problem led to a quite serious instability of the

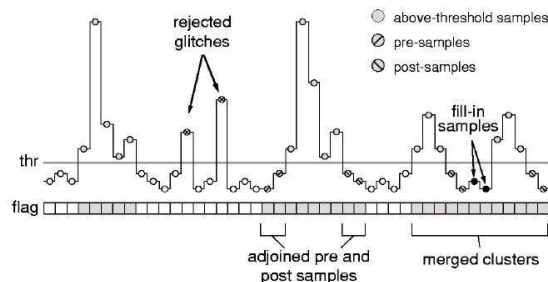


Figure 9.3: The zero-suppression scheme. The glitch filter and number of pre- and post-samples are set in the *equipementlist_TEST.c* file.

data acquisition when the gas conditions were not optimal. The principle of zero-suppression is shown in the Figure 9.3, where the minimal number of consecutive samples above threshold is to be fixed within the glitch filter function.

The data formatting is done in two steps in order to allow the proper decoding: first the cluster labeling and then the data packing. Each set of data is tagged with two words, its time stamp and its size. The time information corresponds to the time stamp of the last sample in the set, and the size represents the number of 10 bit words in the set, including the data samples, the time stamp and itself. Since the readout is originally done through a 40-bit-wide bus on the ALICE experiment, the 10 bit words must be formatted in 40 bit words. At the end of the acquisition, additional bytes are provided if needed to align to a 40 bit word. A 40-bit-trailer word is finally appended. It contains the total number of 10 bit words in the packet and the channel and chip addresses. The resulting data block has a back-linked structure and the decoding must be done starting from the end.

9.2.2 The Detector Monitoring

The detector global monitoring is schematically represented in Figure 9.4. The file and data servers are stored on the *pcoharp07* and the *pcoharp103* machines respectively in a sub-control room. In the main control room, the *pcoharp15* machine is used for the TPC visualisation and the electronics monitoring, while the *pcoharp14* machine is used for the data acquisition. The monitoring of the GEMs was initially done with the *pcoharp13* machine and then via the laptop. The U2F is connected to the *pcoharp02* machine, which is directly placed in the experimental area next to the magnet.

For the visualisation of the TPC with the HARP software, the following points should be done:

- To visualise events on the HARP Event Display, go to the `/home/tpctest/Software/offline/DEV/v7r7/Analysis/v7r7a1/src/T2kTpcAnalysis` directory, and use the *TpcAnalysisUI* executable with the *jobOptions.t2k.debug* jobOption, typing the `../slc3-gcc323/TpcAnalysisUI.exe jobOptions.t2k.debug` command. The run number should be previously declared as a property of the *LoadRawFromDAQAlg.cpp* algorithm in the jobOption with the line `LoadRawFromDAQAlg.RawDataSource = "/tpctest/run/xxx.001.dat"`.
- Attention should be paid that the correct board configuration is implemented for the detector representation. In case of any change in the order of the boards, the respective modifications should be exported to the *LoadTpcCAAlg.cpp* algorithm in the `/home/tpctest/Software/offline/DEV/v7r7/DetRep/v7r7/DetRep/CalibAlign` directory; that is, the board configuration is to be given from bottom to top with the `int cardOrder[N_ADC_CARDS_GEM]`

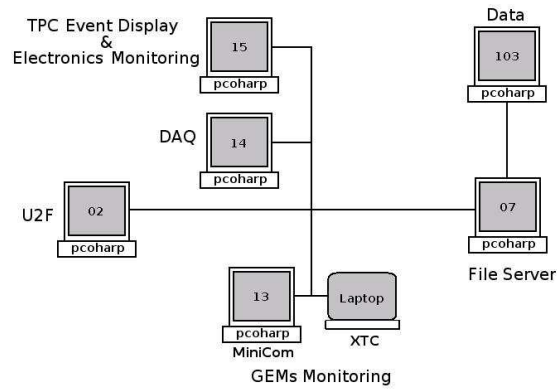


Figure 9.4: Schematic overview of the detector monitoring.

= 14, 13, 12, 11, 9, 8, 7, 6, 5, 3, 2, 0 line (for this particular configuration), and the number of the first board is to be given with the line *card* =14. The last point is required because only the first card is loaded to perform the mapping; the same structure is then copied to the other boards.

- The zero-suppression can also be done offline. In this case the pedestal file number and the pedestal computation option should also be declared as properties of the *ObjectCnvAlg.cpp* algorithm in the jobOption with the lines *ObjectCnvAlg.PedestalsFile* = *"/tpctest/Pedestals/pedestal:xxx.ca"* and *ObjectCnvAlg.ComputePedestals* = *true* respectively.

9.2.3 Data Acquisition Operation

The standard sequence used for the data acquisition is the following:

1. Start the Altro and the U2F drivers in the *Altro_usb* directory
2. Start the respective daemons if you want to use the information browser afterwards, using the */date/.commonScripts/dateSiteDaemons start* and the *infoBrowser* commands respectively.
3. Use the *startdaq* command to launch the DAQ system.
4. Switch ON the GEMs power supply before launching XTC.
5. Ramp up the GEMs in the *Pedestal run* working point.
6. Switch the trigger logic ON.
7. Switch ON the readout electronics.
8. Ramp up the field cage.
9. Use the *runOpts 0* alias to set the non zero-suppression mode in the *equipementlist TEST.c* file.
10. Reset the U2F before starting the acquisition.

11. At the DAQ user interface: first use the *unlock* icon to start a session, then follow the different icons that will load the *equipementlist.TEST.c* file. After *Starting processes*, just press *Start* to launch the acquisition.
12. Take a few triggers (about 100).
13. In the */home/tpctest/monitoring* directory, use the *TPCMonitor_peds* programme with the *TPCMonitor_peds -r xxxx -n k* command, where *xxxx* stands for the run number and *k* for the number of events to process, to see the mean RMS per board with the *plot board* option.
14. In the */home/tpctest/monitoring* directory, use the *tpc_pedestals* programme with the *tpc_pedestals/tpctest/runxxxx.001.dat test.ca* command to compute the pedestal file and then copy it to the pedestals directory with the *cp test.ca tpctest/Pedestals/pedestalxxxx.ca* command.

After step 5, steps 9 to 14 should be repeated each time a pedestal run is needed. The following sequence is for data taking:

15. Ramp up the GEMs in the *Data Taking* working point.
16. Use the *runOpts 1 xxxx* alias to set the zero-suppression mode with the pedestal file number *xxxx*.
17. Reset the U2F before pressing the *Starting processes* icon.

The last point is to be repeated for each run.

9.3 The Data Reconstruction

9.3.1 The Reconstruction Chain

The reconstruction chain is contained in the *ObjectCnv* and the *Reconstruction* packages. It consists first in the unpacking of the data, second in the reconstruction of events and third in the fitting of the tracks.

The Clustering and Track Fitting

The clustering algorithm has been adapted to the new pad geometry which is represented on Figure 9.5. As mentioned before, the default method implemented in the HARP software for the clustering is the computation of the charge centroid. A cluster is defined as a collection of adjacent pads in a row that receive a signal at the same time. In the reconstruction software, the ADC/time serie is checked sample by sample, and a hit is defined as a certain number of successive samples that satisfy some conditions (basically being above a given threshold). In this way it is possible to get more than one hit per pad. The clustering is done for each row and associates hits that are in the same time window for the respective pads. The pads associated in a same cluster will also be referred to as *hits* in the following.

The track fitting is implemented with a least squares method.

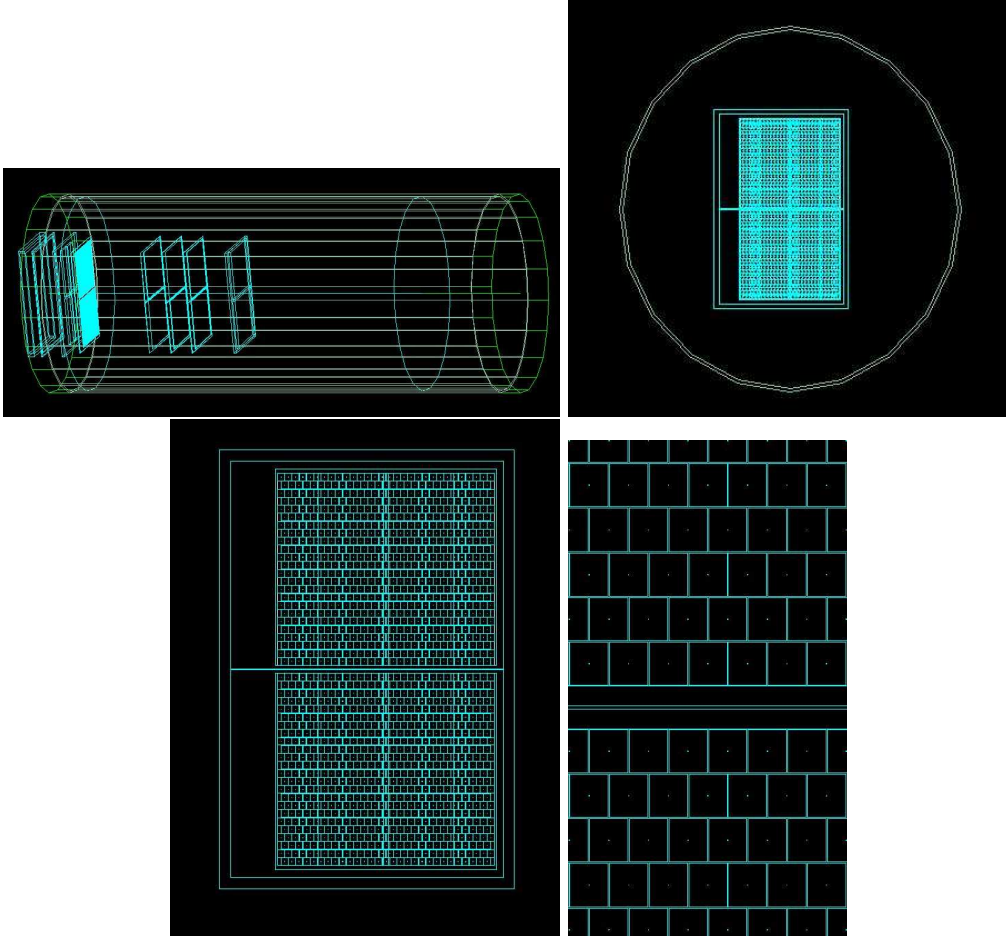


Figure 9.5: Different views of the new implemented geometry of the readout plane in the HARP TPC.

Ntuples production

The ntuples are produced in the last step of the reconstruction chain. They contain a collection of 30 variables for each event, giving full information on the tracks. A few variables such as the χ^2 of the fit or the number of clusters per track are one dimensional parameters. All the other variables are declared as vectors which are labelled by the cluster number, e.g. number of hits per cluster, x and y position of the cluster, x position of the fit for each cluster, etc.

Chapter 10

Data Analysis

The analysed data are taken from the first $ArCO_2$ measurement session without magnetic field. The idea is to show different methods to determine the point resolution of the prototype. Due to the conditions of data acquisition during the last session, this brief and preliminary study will just focus on spatial resolution and more general topics such as drift velocity measurements or charge attenuation. A more elaborated version of this study should follow soon and include also a dE/dx resolution study. The analysis presented in this chapter is not intended to be a detailed and complete data analysis, but is giving the general baseline that will be followed for further investigations.

10.1 Basic Distributions

In this section are presented some raw information from the electronics monitoring and a few event displays. Figure 10.1 shows the mean RMS for two different boards as measured at the *Pedestal run* working point. The mean value is around 1.8 ADC counts which is the expected noise from a rough extrapolation from the ALICE electronics results. Among the 12 boards, 3 to 4 boards have some more noisy channels. This is due on one hand to the position of the board (external boards are usually more noisy) and to some interferences between the flex and ribbon cables, which are sometimes in contact with each other. Some channels can have a mean RMS up to 4 to 4.5 counts but are usually reduced around 2.5 counts by adjusting the cables.

Figure 10.2 shows typical pulses in ADC counts for 2 pad clusters. In the *Data taking* working point, during the $ArCO_2$ measurement session, saturation could even be observed sometimes for events with high ionisation.

Figure 10.3 shows a display of the available sector during the $ArCO_2$ measurements. It seems that a few channels are not working correctly over the sector (732 pads). The pads on the edges clearly collect less charges than the other pads, and this should require more investigations.

Figure 10.4 shows two nice event displays from the $ArCO_2$ measurements. The displays from Figure 10.5 are from the second $ArCO_2$ measurement session of March 2006.

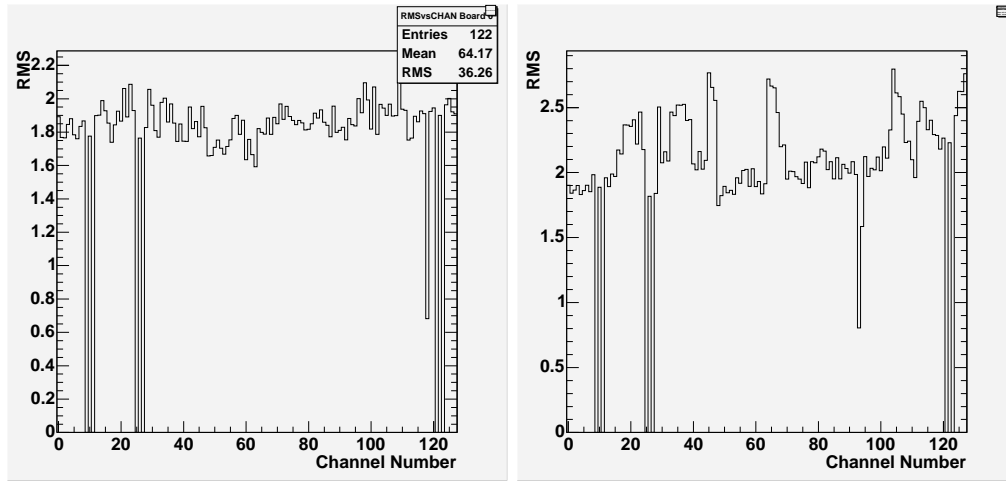


Figure 10.1: Mean RMS per channel on board 0 (Left) and board 14 (Right). The channels without signals are grounded channels.

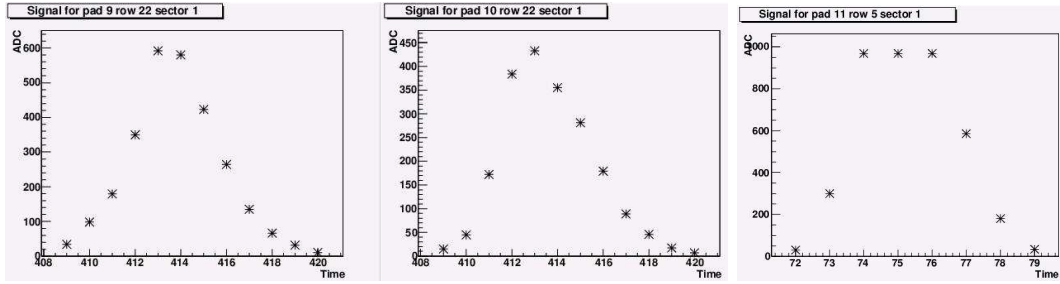


Figure 10.2: Typical pulses in a two pad cluster (Left), saturation of the signal in an event with high ionisation.

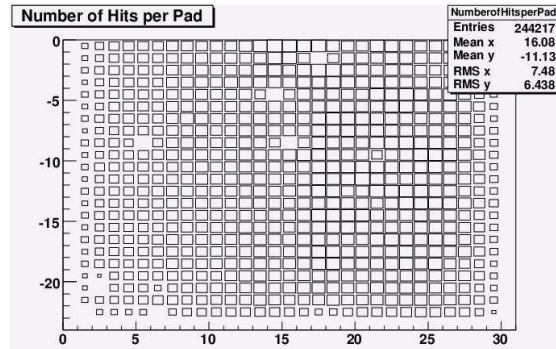


Figure 10.3: Number of hits per pad for the lower sector of the prototype over the run 1369.

10.2 Drift Velocity Measurements

10.2.1 P5 Measurements

It is possible to get a first estimation of the drift velocity when observing the end of the chamber. During the P5 measurements, it was possible to see the complete chamber in the first 480 time Master Thesis by N.Abgrall, February 2006

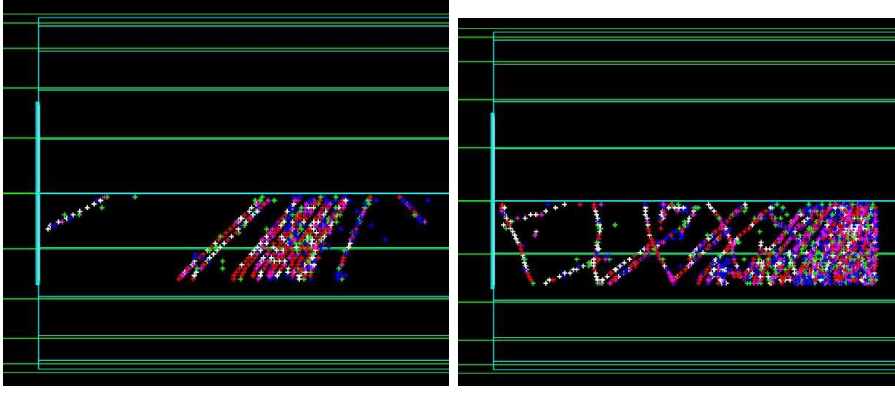


Figure 10.4: Particle showers resulting possibly from the interaction of a proton in the iron yoke of the magnet.

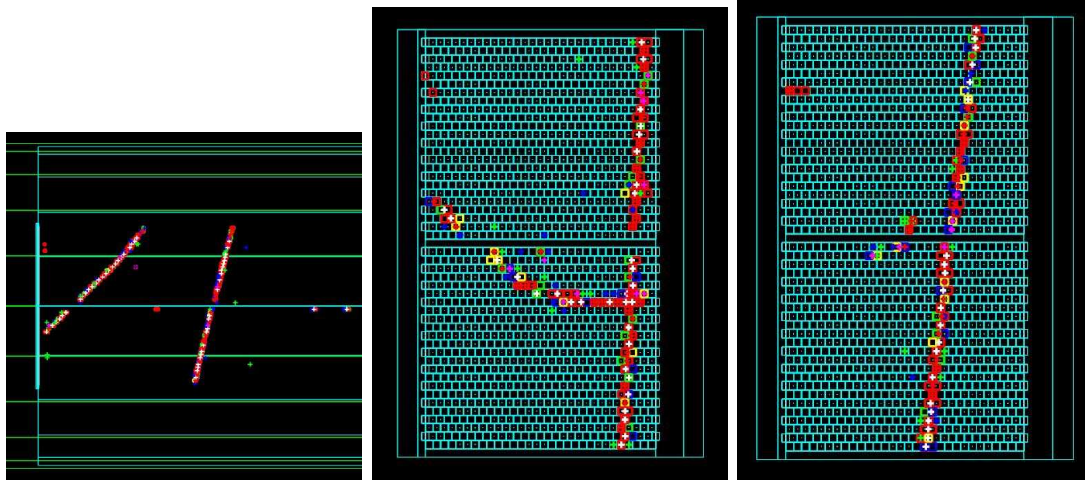


Figure 10.5: Side view of the chamber with a double-track event (Left), front view with the emission of a δ -electron (Middle), front view with the visible signal of the iron source in the middle of the pad plane (Right).

bins. Figure 10.6 shows the z distribution of the clusters for the first six boards from the top of the detector. A drop of the signal is observable around 400 time bins. A rough estimation gives a drift velocity of $3.9 \text{ cm}/\mu\text{s}$, that is really closed to the theoretical value which is between 4 and $4.1 \text{ cm}/\mu\text{s}$.

The signal of the ^{55}Fe source located on the central axis of the chamber, is also visible on Figure ?? for the fifth and especially sixth board. Figure 10.7 shows the spectrum of the iron source from the P5 measurement session. The escape peak from Argon is clearly visible.

10.2.2 ArCO_2 Measurements

During the ArCO_2 measurements, it was not possible to see the end of the chamber in the first 960 time bins, but the trigger could be delayed to divide the chamber in two parts. Figure 10.8 shows the z distribution of the clusters for two different delays. Using these informations, the

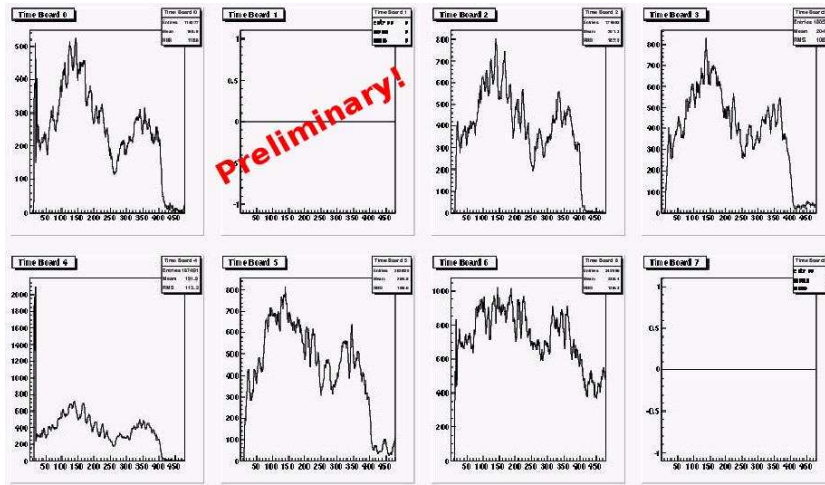


Figure 10.6: ADC counts distribution in time for different boards.

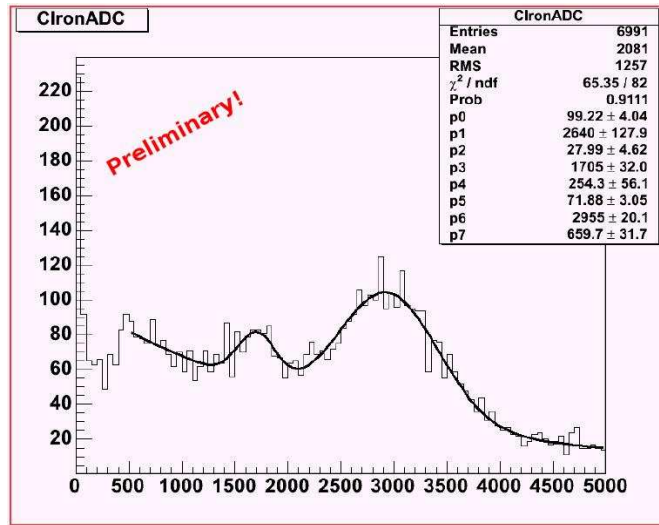


Figure 10.7: Energy spectrum of the iron source from the P5 measurements.

drift velocity could be estimated to 1 cm/ μ s.

10.3 Tracks Parameters

The ntuples produced with the reconstructed data from the HARP software are filled event by event, where an event is defined to contain only one track. Each track is characterised by a collection of variables and a set of fit parameters, which in the scope of this study, are the parameters of a straight line. The tangent of the ϕ angle defines the slope of the track in the xy plane, so that for vertical tracks in this plane, $\phi = 0$; the tangent of the θ angle defines the slope in the yz plane in the same way. Figure 10.9 and Figure 10.10 show some basic parameters

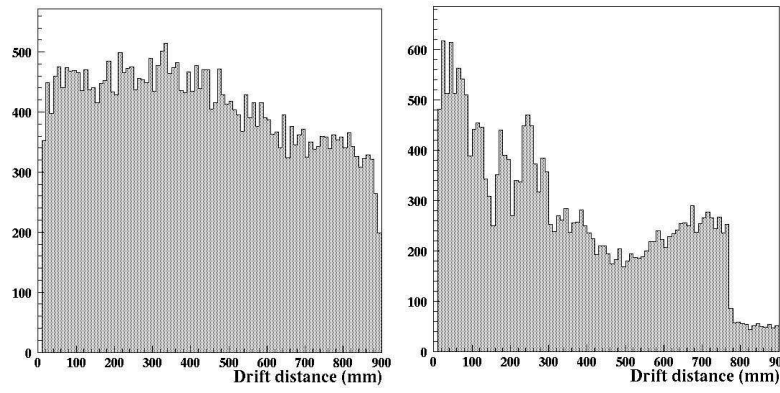


Figure 10.8: z distribution of the clusters with a 75 μs delay (Left) and a 85 μs delay of the trigger.

of a track: track angles, number of cluster per track, number of hits per cluster, charge per track. All these distributions are extracted from run 1369, which was taken with a single sector.

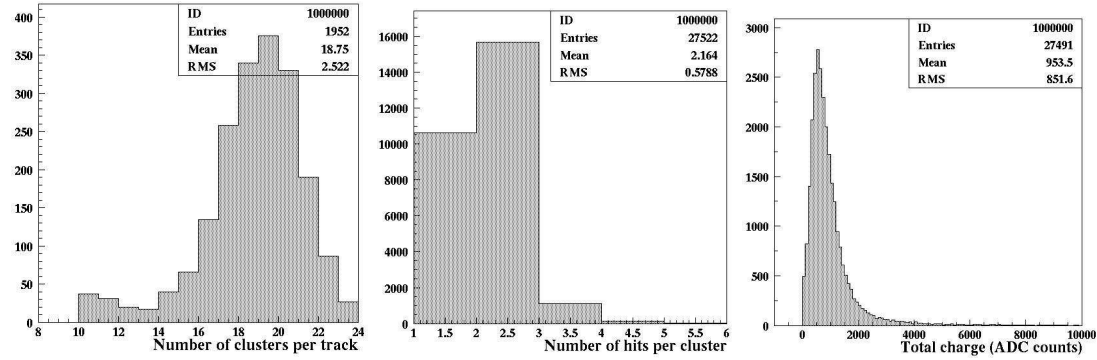


Figure 10.9: Distributions of the number of clusters per track (Left), number of hits per cluster (Middle) and total charge per track (Right).

The χ^2 of the track fit is computed as,

$$\chi^2 = \sum_{i=1}^N \left(\frac{x_i - x_i^t(\vec{v})}{\sigma_{x_i}} \right)^2 \quad (10.1)$$

where $x_i^t(\vec{v})$ is the theoretical value of the observable x_i (position of the cluster) dependent on a vector of track parameters, and σ_{x_i} is the error on x_i . The χ^2 distribution will more or less depend on the value of σ_{x_i} that is initially fixed and, since the clustering is done before fitting the tracks, it is also intrinsically dependent on the way the clustering is implemented.

In the HARP software, the clustering can be done by using six different methods where the estimate is determined with different charge, time and number configurations of the respective hits. For this study, the default method has been used, estimating the position of the signal by the simple centroid computation. The error on x_i is initially fixed to 0.05 mm, that is far too small to be achieved by the centroid method. This is the reason why on Figure ??, the χ^2 distribution is centered around 1 but larger and centered around 2. After refitting the tracks

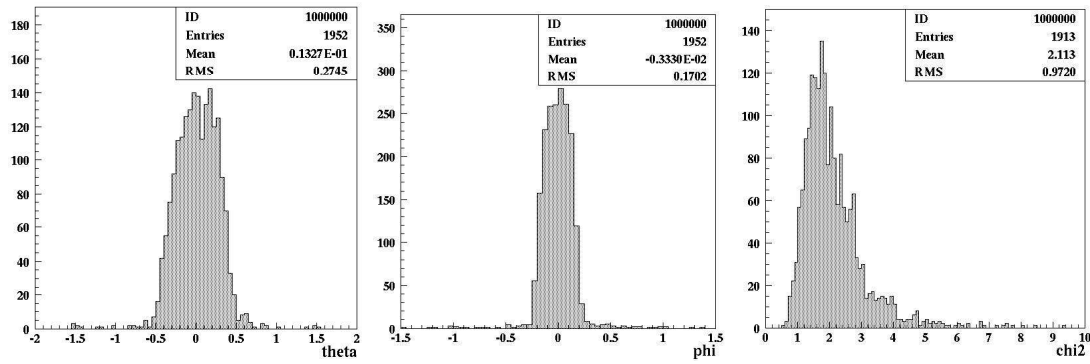


Figure 10.10: Tracks distributions for the θ (Left) and ϕ (Middle) angles. χ^2 distribution (Right).

with the corrected centroids, the distribution should be centered around 1, what is expected for a χ^2 distribution per number of degrees of freedom ($N - p$), where N is the number of points to fit and p is the number of parameters of the fit.

It is shown in Figure 10.11, that the ratio of the number of clusters with more than one pad over the number of clusters with only one pad, is minimal at small drift distances. Actually, for small drift distances, the diffusion in the gas is not large enough to sufficiently spread the charges over more than one pad. The ratio then increases linearly until 500 mm drift, where it reaches a plateau due to the effect of charge attenuation compensating for large diffusion. Afterwards, the ratio drops again since the number of 1 pad clusters increases because of the larger attachment.

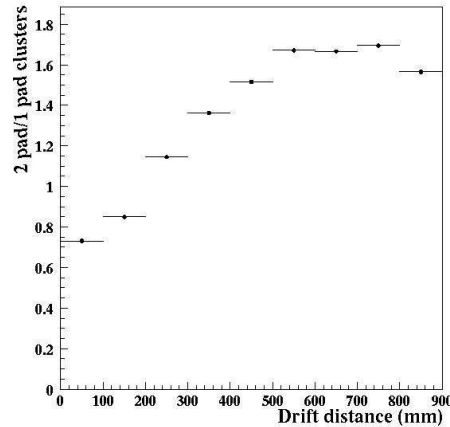


Figure 10.11: Ratio between the numbers of 2 pad clusters and 1 pad clusters as a function of the drift distance.

10.4 Charge Attenuation

$ArCO_2$ is very sensitive to electron attachment [14]. The value of the attachment can be computed plotting the collected charge per cluster as a function of the z coordinate. The charge attenuation is then computed assuming an exponential dependency on the drift length:

$$N(z) = N_0 e^{-\frac{z}{\lambda}} \quad (10.2)$$

where N_0 is the initial charge of the cluster and λ is the attenuation length. Figure 10.12 shows the charge of the clusters as a function of the drift distance for run 1369 and vertical tracks ($abs(\phi) < 0.05$). The slope of the exponential fit gives an attenuation length of approximately 1148 mm.

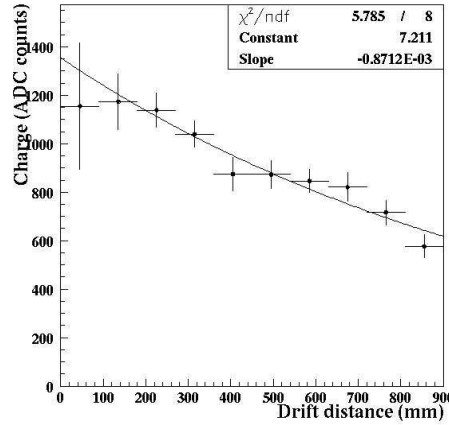


Figure 10.12: Total charge as a function of the drift distance.

Figure 10.13 shows the attenuation length as a function of the run number. As can be seen, attachment is a really critical parameter and is prone to large fluctuations in time, here between about 0.5 to 3m. It is nevertheless possible to stabilize this effect for $ArCO_2$. The fluctuations observed on Figure 10.13 are also mainly due to low statistics per run. It can be seen that these fluctuations are highly reduced for run numbers between 1410 and 1440 which have more statistics.

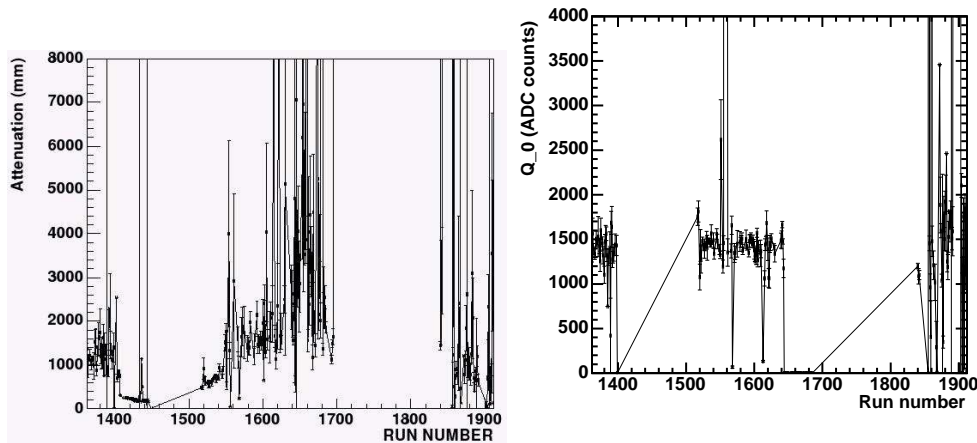


Figure 10.13: Attenuation in mm (Left) and charge at zero drift (Right) as functions of the run number.

Figure 10.13 also shows the mean amount of charge extrapolated to zero drift distance, where minimal attenuation is expected. This amount of charge is very stable and independent on the attenuation length variations over the different runs.

10.5 Analysis

10.5.1 Resolution Determination Methods

In the following study, the point resolution is determined with the standard computation of the residuals,

$$x_r = x - x_f \quad (10.3)$$

where x is the position of the cluster and x_f is the respective position of the fit. The resolution is then directly given by the variance of the residual distribution since the error on the fit is usually respectively small:

$$\sigma_r^2 = \sigma_x^2 + \sigma_f^2 \approx \sigma_x^2 \quad (10.4)$$

The Pad Response Function (PRF) Method

The computation of the cluster center of gravity is not a reliable reconstruction method (see Figure 10.14). Actually, the sampling of a gaussian distribution in different bins is not linear, and this directly induces a bias of the computed centroid position with respect to the true position of the center of the charge cloud.

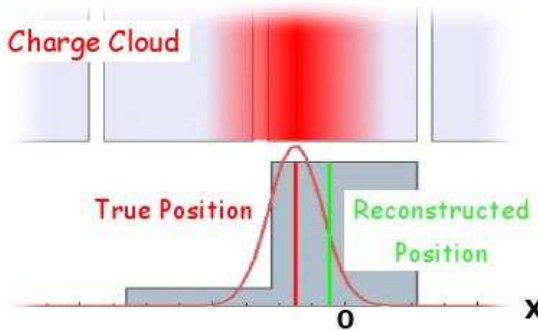


Figure 10.14: The centroid position does not reflect the true position of the charge cloud.

This effect can be corrected by computing analytically the correction function which depends on the computed center of gravity and the sigma of the charge cloud. This last parameter can be predicted by a simulation or given by other fits as it will be explained in the following sections. In a simple model to compute the PRF, the charge distribution is supposed to be a gaussian of mean x_t (the true position of the cluster) and standard deviation σ^2 :

$$G(x, x_t, \sigma) = \frac{1}{\sqrt{2\pi}\sigma} e^{-\frac{1}{2} \frac{(x-x_t)^2}{\sigma^2}} \quad (10.5)$$

The charge collected by the pad i is then given by the integration of the distribution over the width, w , of the pad:

$$\begin{aligned}
Q_i &= \int_{x_i}^{x_i+w} G(x, x_t, \sigma) dx \\
&= \int_{x_i}^{x_i+w} \frac{1}{\sqrt{2\pi}\sigma} e^{-\frac{1}{2} \frac{(x-x_t)^2}{\sigma^2}} \\
&= \int_{\frac{x_i-x_t}{\sigma}}^{\frac{x_i+w-x_t}{\sigma}} \frac{1}{\sqrt{2\pi}} e^{-\frac{1}{2} z^2} dz \\
&= -\operatorname{erf}\left(\frac{x_i-x_t}{\sigma}\right) + \operatorname{erf}\left(\frac{x_i+w-x_t}{\sigma}\right)
\end{aligned} \tag{10.6}$$

where x_i is the position of the border of pad i from a cluster of n pads. The reconstructed centroid position is then given by:

$$x_c = \frac{\sum_{i=1}^n Q_i x_i^c}{Q_{tot}} \tag{10.7}$$

where x_i^c is the center position of pad i and Q_{tot} is the total charge of the cluster. The result of the computation is plotted in Figure 10.15 for different values of σ .

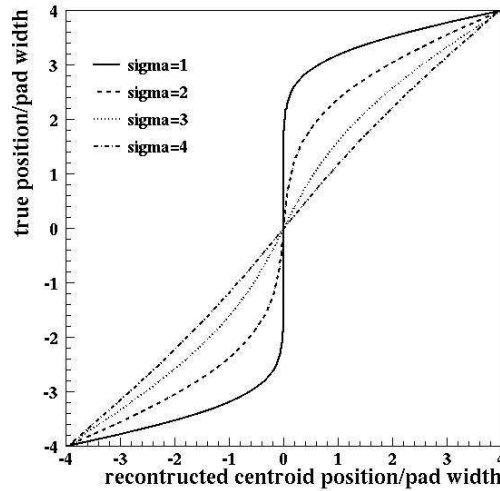


Figure 10.15: Correction function of the reconstructed centroid position for different values of σ .

One complication of the TPC is that the charge cloud width depends on the z origin of the electrons. This implies that the σ is actually a function of the z (time) coordinate of the cluster. The correction is therefore applied to the clusters as a function of z , where the z dependency of the σ of the charge cloud has to be measured with an alternative method. The residuals are then computed with the corrected positions of the centroid and the track is fitted using the standard χ^2 minimisation. Figure 10.16 shows the correction function for every z and the resulting residuals distribution over the pad width.

Figure 10.17 shows the resolution as a function of z for two different run sessions. The tracks are selected such that $|\phi| < 0.05$ and with a charge attenuation length $\lambda > 1m$. The black line without points represents the RMS for the 2 pad clusters, in black is represented the resolution

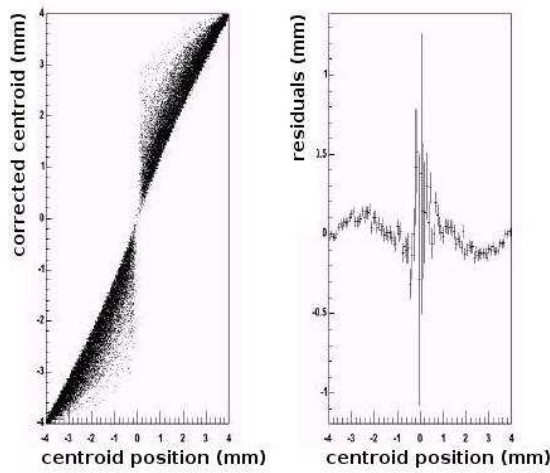


Figure 10.16: Correction function for every z (Left), residuals over a pad width after the correction (Right).

for 2 pad clusters and in red is represented the resolution for 1 pad clusters only. It can be seen that it is actually less than $8/\sqrt{12}$ since 1 pad clusters occur only when there is no 2 pad clusters, thus narrowing the acceptance region of the signal over a region centered on the pad and of smaller width. The resolution for 2 pad clusters is smaller than $400\ \mu\text{m}$ for $200\ \text{mm}$ drift.

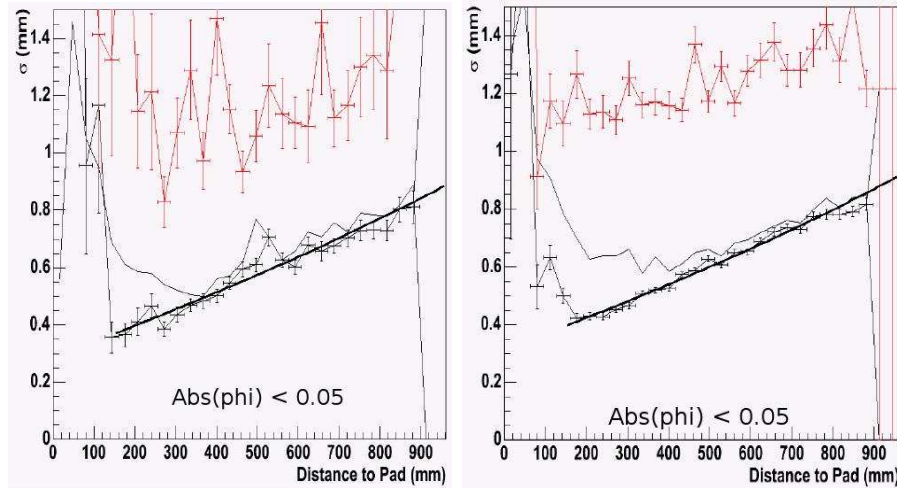


Figure 10.17: Resolution as a function of z for runs 1362 to 1369 (Left) and runs 1517 to 1538 (Right). In red is the 1 pad cluster resolution, in black the 2 pad cluster resolution and the line is the RMS for the 2 pad cluster resolution.

The Charge Per Pad Fit Method

Here is described a method that was worked out to correct the reconstructed centroid position independently of any given external sigma of the charge cloud. The results are extracted from

run 1369 without magnetic field. The statistics, although sufficient to give the general baseline of the analysis, is therefore quite limited. The method consists in two algorithms written in *FORTRAN* to read and act on the ntuples provided by the HARP software. The first algorithm is computing analytically the z dependency of the sigma of the charge cloud, and the second one is computing the resolution as a function of z .

The first 900 mm of the chamber are divided into N z -slices. Using the previous expression for the PRF, a subroutine (*q_fit*) is called for k iterations to fit the charge distribution of the cluster (see Figure 10.18). The fit is a step function that depends on the position of the pad in the cluster. For a given σ it computes the theoretical charge collected by each pad of the cluster. The fit has two free parameters, the normalisation constant and the mean position of the charge cloud, which is then used from the fit to compute the residuals.

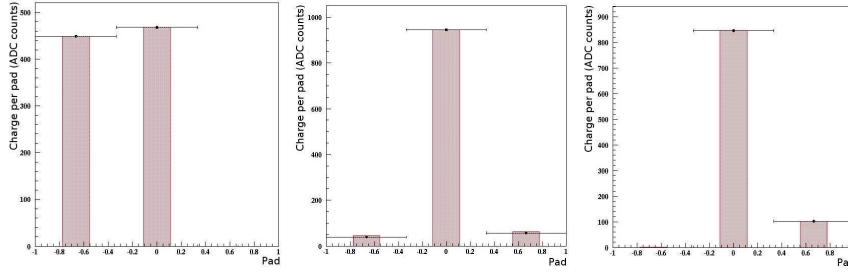


Figure 10.18: The charge per pad is fitted for 2 pad and 3 pad clusters configurations.

The sigma of the charge cloud is initially fixed to a plausible value and incremented over the k iterations so that $N \times k$ residual distributions are finally obtained (for this study $N = 10$ and $k = 20$). Each distribution is fitted with a gaussian and the third parameter of the fit is giving the resolution for the respective z -slice and sigma of the charge cloud (see Figure 10.19 and Figure 10.20).

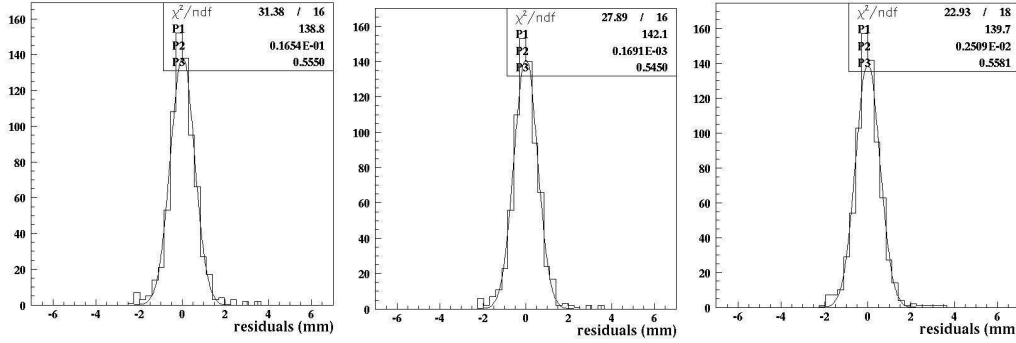


Figure 10.19: Residual distributions for three different values of the sigma of the charge cloud between 300 and 400 mm.

The resolution per z -slice can then be plotted as a function of the sigma of the charge cloud, and the expected sigma is taken to be the one that minimises the resolution (see Figure 10.21 and Figure 10.22). The plots of Figure 10.19 and Figure 10.20 are centered around the minimising value of σ for the respective z -slices.

As can be seen, the value of the sigma of the charge cloud that minimises the residuals, is increasing with the distance in the drift volume as expected.

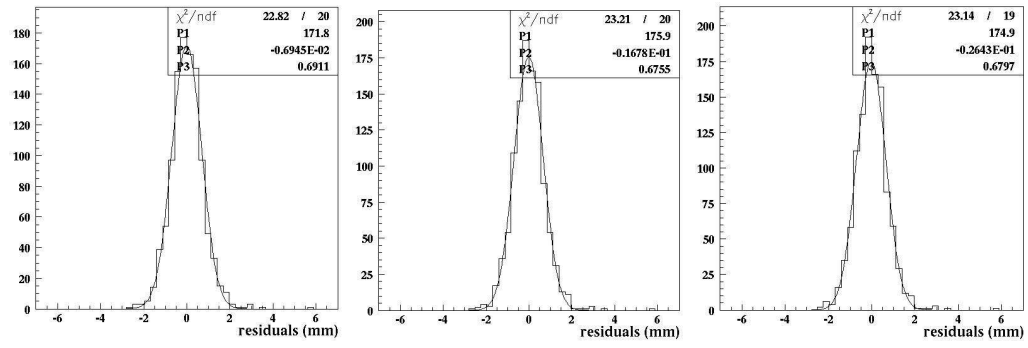


Figure 10.20: Residual distributions for three different values of the sigma of the charge cloud between 500 and 600 mm.

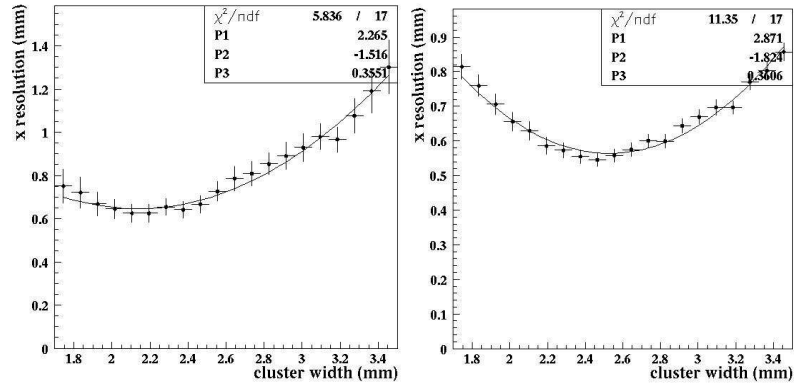


Figure 10.21: x resolution (mm) vs the sigma of the charge cloud for two different z-slices: 100 to 200 mm (Left) and 300 to 400 mm (Right).

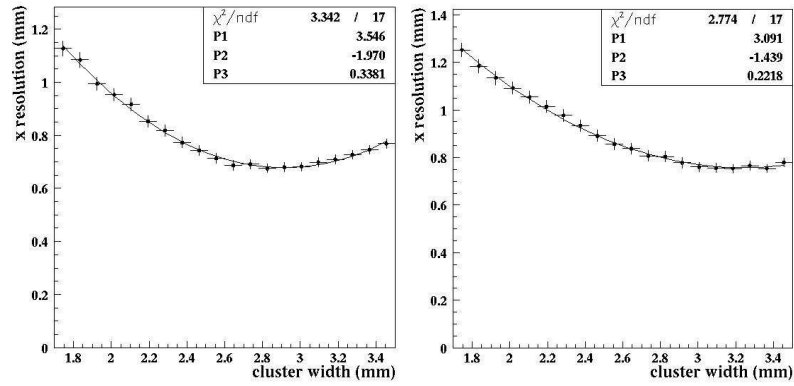


Figure 10.22: x resolution vs the sigma of the charge cloud for two different z-slices: 500 to 600 mm (Left) and 700 to 800 mm (Right).

Using the values that minimise the residuals, the sigma of the charge cloud can be finally plotted as a function of z, and the dependence analytically computed, as shown in Figure 10.23.

At this level, it should be pointed out that the method that is described here, is based on a very simple model for the pad response function that is just supposed to be dependent on the charge cloud width. This model is a kind of a baseline and should certainly be improved, so that the results that we present here are obviously biased from the true expected parameters. In this analysis, such parameters as the charge cloud width or the resolution in x, are not to be taken as true values but are parameters determined to get the best results for this model.

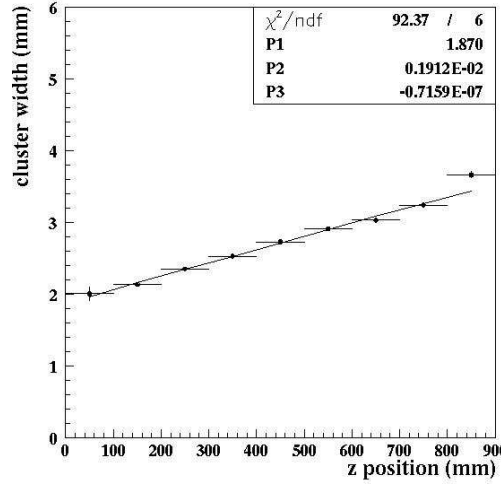


Figure 10.23: Cluster width (mm) as a function of the drift distance.

If the GEMs individually provide a gain g (with negligible variance), the defocussing in the respective GEMs structure adds a variance term σ_0^2 to the x distribution of the n_p electrons arriving at the GEM plane. The variance of the mean x coordinate is then given by [15]:

$$\sigma_x^2 = \frac{1}{n_p}(\sigma_d^2 + \frac{\sigma_0^2}{g}) \quad (10.8)$$

where σ_d^2 comes from the diffusion in the drift volume. To achieve the diffusion limit, the GEM term should be much smaller than the diffusion term. The x coordinate of each electron is not measured in the TPC, but rather the charge collected and shared by neighbouring pads is used to deduce the mean x coordinate. It can be shown analytically that for a gaussian charge distribution of mean μ and variance σ^2 , the estimate, $\hat{\mu}$, determined from the observed fraction of charge, $\langle F \rangle$, in one pad of a 2 pad cluster, has a variance,

$$\sigma_{\hat{\mu}}^2 = 2\pi\sigma^2 e^{\mu^2/\sigma^2} \sigma_F^2 \quad (10.9)$$

where the variance of F is binomial, $\sigma_F^2 = \langle F \rangle (1 - \langle F \rangle)/n$, and n is the number of electrons. Thus, when the charge cloud is centered between the two pads, the variance reduces approximately to $\sigma_{\hat{\mu}}^2 \approx 1.6\sigma_x^2$. As the mean moves away from the border of the pads, the variance gets larger and to limit the GEMs contribution to the resolution, the width of the pads should not exceed 3 to 4σ .

It can be seen on Figure 10.23 that the width of the charge cloud at zero drift is not negligible, around 1.8mm. This behaviour can not easily be explained by only physical reasons and probably stresses out an underlying problem in the way the method is implemented. Nevertheless, the probable intrinsic bias of the method is certainly intensified by two other facts: on one hand, for

the results presented here, the method is implemented for 2 pad clusters only; that is, the charge cloud width is artificially forced to be large at zero drift distance. On the other hand, as shown in Figure 10.10, the ratio of 2/1 hit clusters decreases at small drift distances.

A last thing to point out about Figure 10.23 is the dependency on z^2 of the charge cloud width. Actually, this behaviour might be due to the attenuation: since the amount of collected charges decreases with the drift distance, the effective width of the charge cloud seems smaller at large drift distances.

Afterwards, the other algorithm computes again a residual distribution for each z-slice with the *q_fit* subroutine (see Figure 10.24), taking the z dependency of the sigma of the charge cloud computed by the previous algorithm as third parameter of the fit.

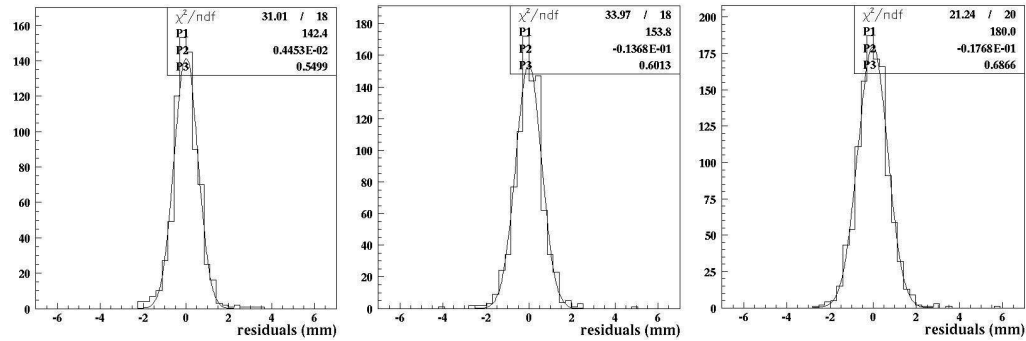


Figure 10.24: Residual distributions after the centroids correction for clusters between 300 and 400 mm (Left), 400 and 500 mm (Middle) and 500 and 600 mm (Right).

The centroids are thus corrected with the expected value of the charge cloud width for each z-slice. Figure 10.25 shows the distribution of the residuals over a pad width before and after correction. The bias due to the simple centroid method is clearly reduced, but for the correction to be improved, the sigma of the charge cloud has still to be tuned more precisely.

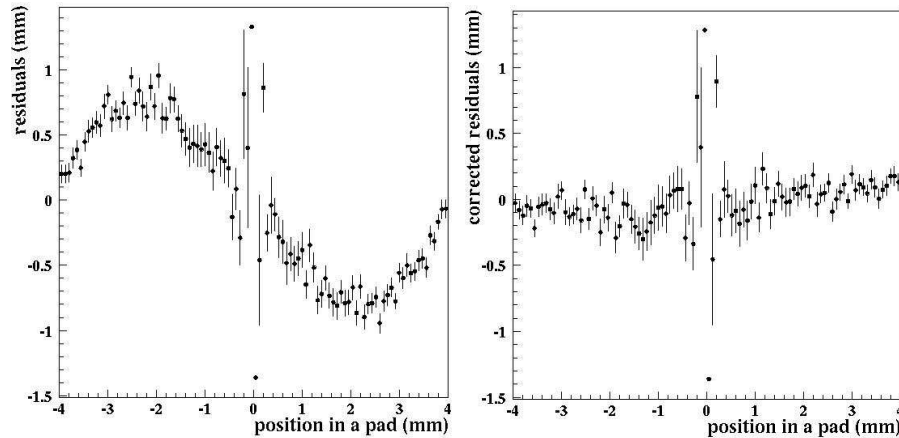


Figure 10.25: Residuals over a pad width before (Left) and after (Right) correction of the centroids.

The gaussian fit of the residual distribution for each z-slice finally enables to plot the resolution

as a function of z (see Figure 10.26).

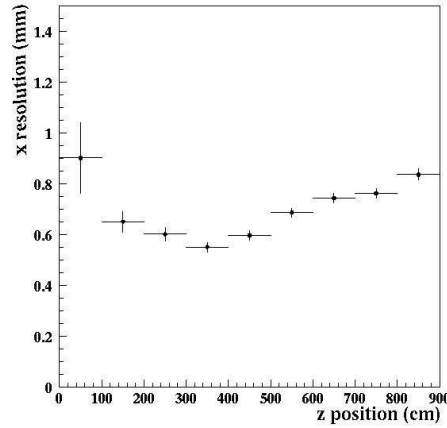


Figure 10.26: x resolution as a function of the drift distance.

The Likelihood Fit

This method is based on a more elaborated model as far as the charge distribution is concerned. The considered gaussian distribution about the projection of the track on the readout plane is actually a convolution between the two-dimensional isotropic probability density function due to diffusion in the drift volume, and the approximative gaussian distribution of the ionisation electrons along the track (supposed to be uniform at the level of a row).

One advantage of this method is that the σ of the gaussian can be itself a parameter of the fit, thus giving an estimate of the diffusion for each event (the other possibility is to give it as an external input from a simulation). The z dependency of the charge cloud width can then directly be given as a result of the fit. Another improvement is that the angle ϕ of the track with respect to the pad is taken into account to evaluate the charge sharing between adjacent pads. The other parameters are the horizontal distance, b , between the pad center and the track, and the local azimuthal angle, ϕ , and can be expressed for a given row, as functions of the reference coordinates and of the radius of curvature. For simplicity, σ is supposed to be constant along the length of the track, which is reasonable for vertical tracks (see tracks selection criteria in [15]) if ionisation fluctuations are neglected. Another initial assumption of the model is that the height of the pads is much smaller than the radius of curvature, so that a track is considered to be straight within the vertical extent of a row. The likelihood is computed for each row, and an overall likelihood function is given by the product of all these subfunctions.

The pad response function is given by the integration of the charge distribution over the physical extent of the pad

$$I(b, \phi, \sigma, h, w) = \int_{-w/2}^{w/2} \int_{-h/2}^{h/2} \frac{dx dy}{\sqrt{2\pi}\sigma} \times \exp\left(-\frac{[(x-b)\cos\phi + y\sin\phi]^2}{2\sigma^2}\right) \quad (10.10)$$

$$+ \eta(b, \phi, \sigma, -h, -w) - \eta(b, \phi, \sigma, h, -w) \quad (10.11)$$

where

$$\eta(b, \phi, \sigma, -h, w) = \frac{1}{\cos\phi \sin\phi} \xi\left(\left(b + \frac{w}{2}\right)\cos\phi + \frac{h}{2}\sin\phi, \sigma\right) \quad (10.12)$$

and

$$\xi(u, \sigma) = \frac{u}{2} \operatorname{erf}\left(\frac{u}{\sqrt{2}\sigma}\right) + \frac{\sigma}{\sqrt{2\pi}} \exp\left(-\frac{u^2}{2\sigma^2}\right) \quad (10.13)$$

The log-likelihood function is given by

$$\log \mathcal{L}_{row} = \sum_i n_i \log p_i + \text{constant} \quad (10.14)$$

where n_i is the number of primary electrons and p_i is the probability that a primary electron of the track is associated to pad i

$$p_i = I(b_i, \phi_i, \sigma, h_i, w_i) / \sum_j I(b_j, \phi_j, \sigma, h_j, w_j) \quad (10.15)$$

where j runs over all pads of the respective row.

Figure 10.27 shows the charge cloud width as a function of the drift distance for different run sessions directly obtained from the likelihood fit. The linear term of the fit is of the order of $0.00550 \text{ mm}^2/\text{mm}$, that is $0.234 \text{ mm}/\sqrt{\text{cm}}$, which is compatible with the Magboltz predictions for two of the run sessions. The non-linear term is probably due to the attachment in a similar way the 2/1 pad ratio is affected (see Figure 10.10). The way attachment is reducing the size of the charge cloud is equivalent to cutting the gaussian distribution of charges above a certain height: in this way, tails are cutted and the RMS of the distribution is smaller and the sigma is reduced. Thus, the attachment with the pedestal cut tend to reduce the sigma. This could be the reason for the z^2 dependency.

As far as the point resolution is concerned, the likelihood fit method is not based on any centroid computation, and *residuals* are defined in a slightly different way. Actually, the track is first fitted as a reference over all rows of pads, let's say N . Then it is refitted successively over $N-1$ rows keeping every parameters fixed with respect to the reference except the transverse position; residuals are computed as the transverse position difference with the reference fit, and the distribution over all the events of a data set is fitted to a gaussian to determine the standard deviation σ_w . In this way, σ_w will underestimate the true resolution since the data from the single row is already used in the reference. Therefore, the procedure is repeated without including the single row in the reference fit, and the respective standard deviation, σ_{wo} , will this time overestimate the true resolution since the reference is now not perfectly measured. It can be shown that equivalent results on the estimate of the resolution for a single row for the standard least squares fit, are obtained using the geometric mean of these two standard deviations, $\sigma = \sqrt{\sigma_w \sigma_{wo}}$.

PRF vs Likelihood fit

Figure 10.28, Figure 10.29 and Figure 10.30 show the point resolution computed with the PRF and the likelihood methods for 2, 1 and 3 pad clusters respectively and for three different run sessions. The resolution is computed for vertical tracks ($\phi < 0.05$) to avoid the problem of charge sharing when the track is crossing several pads per row.

To allow the comparison of the two methods, the same prediction for sigma is used in both cases, which is probably not the optimal choice, and the parameters are kept constant over the three

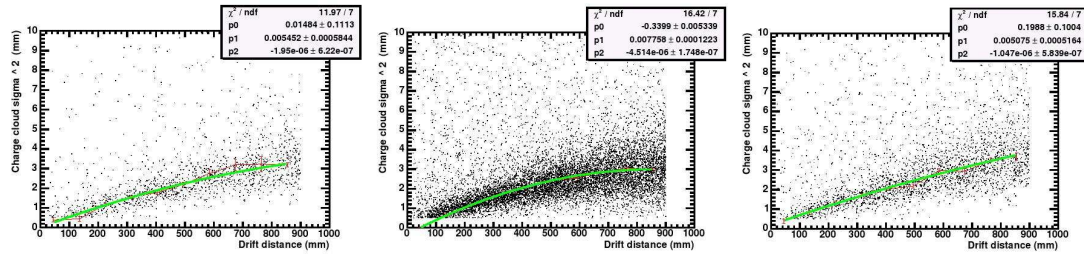


Figure 10.27: The square of the charge cloud width as a function of the drift distance as it is obtained from the likelihood fit. The mean values come from the gaussian fit and are fitted with a second order polynomial. Runs 1362 to 1399 (Left), 1517 to 1538 (Middle) and 1592 to 1640 (Right).

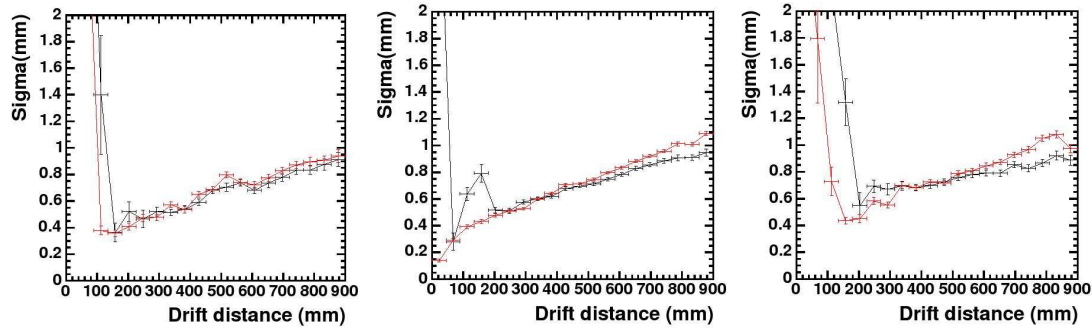


Figure 10.28: 2 pad cluster resolution obtained with the PRF method (black) and the likelihood method (red). For both cases, the geometric mean of the fitted sigma to the residuals is shown for runs 1362 to 1399 (Left), 1517 to 1538 (Middle) and 1592 to 1640 (Right).

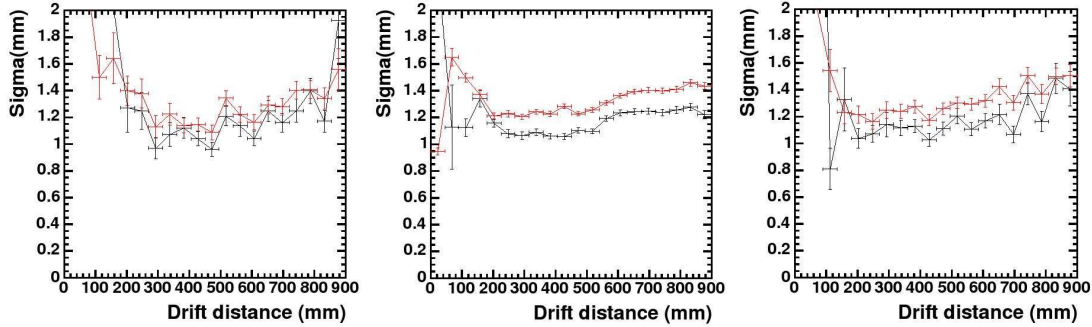


Figure 10.29: 1 pad cluster resolution obtained with the PRF method (black) and the likelihood method (red). For both cases, the geometric mean of the fitted sigma to the residuals is shown for runs 1362 to 1399 (Left), 1517 to 1538 (Middle) and 1592 to 1640 (Right).

run sessions. It can be seen that the results are quite similar for both methods, as expected for vertical tracks.

It is not clear for the moment, how to compare these results with the expectation for T2K. The main requirement is that the relative momentum resolution should be less than 10% for 1 GeV

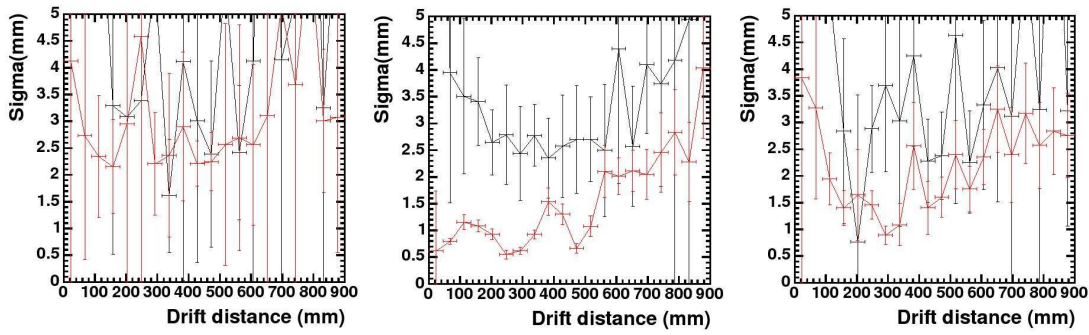


Figure 10.30: 3 pad cluster resolution obtained with the PRF method (black) and the likelihood method (red). For both cases, the geometric mean of the fitted sigma to the residuals is shown for runs 1362 to 1399 (Left), 1517 to 1538 (Middle) and 1592 to 1640 (Right).

muons, which is already good enough to measure the muon momenta in the relevant energy range. From the *Gluckstern formula* [1],

$$\frac{\delta k_{res}}{k} = \frac{p \cos \lambda}{0,3zB} \frac{\epsilon}{L'^2} \sqrt{\frac{720}{N+4}} \quad (10.16)$$

it can be seen that it depends on L^2 (the projected length of the track onto the pad plane), the number of pads and the point resolution. The point resolution itself depends on the transverse diffusion coefficient of the gas and is also affected by the pad size. The attenuation also has effects on the point resolution. As shown in [16], with large pad sizes of the order of $8 \times 8 \text{ mm}^2$, the point resolution is not dominated by diffusion but by pad size effects. For example, for 1 m drift in $ArCO_2$, where a MIP would release around 80 electrons per cm, the theoretical point resolution is given by:

$$\sigma_x = (220 \mu m / \sqrt{cm} \cdot 10 \sqrt{cm}) / \sqrt{80} \approx 260 \mu m \quad (10.17)$$

which is far below the result we obtain of $800 \mu m$ for 1 m drift.

Chapter 11

Conclusion

This master thesis reports the combined R&D efforts from the groups of Geneva, Barcelona and Bari, for a TPC based on GEMs for the ND280m detector at the T2K experiment. For the first time, a TPC is operated with GEMs of this size. The R&D project was started in April 2005 and only 6 months later, the detector was successfully operated. The main goals of this common effort were:

- **Design and construction of a prototype.**
- **Operation of the prototype.**
- **Proof that a T2K TPC with GEMs would fulfil the physics requirements.**

For the first point, a possible design of the detector has been proposed and developed. It was then successfully constructed. A set of GEM foils has been retrieved from the LHCb experiment, tested and integrated in a tower structure based on individual frames. Some problems occurred at the beginning of the construction but were understood and resolved, and a lot has been learned from them. We showed that we can build complete amplification modules based on GEMs. Moreover, a complete testing procedure of the GEM foils has been developed for a possible future large scale production of the modules.

The prototype has been fully integrated to the HARP TPC. It was successively operated during two different measurement sessions at CERN. An answer has been found to every problem that occurred while operating such a device, and a lot of experience has been accumulated. This success shows that we are able to construct and operate such GEM modules. We think that this experience in operating GEM modules is a clear advantage in the perspective of a full size detector construction and operation.

Data have been successfully taken and analysed. The results of this study are still preliminary, but indicate that the GEM option as amplification device fulfils the requirements for the T2K TPC. But more cross checks are necessary. For example, it is planned for the near future to measure the point resolution dependency as a function of the track angle, and the point resolution dependency as a function of the gas quality (attenuation). Some aspects such as the pad size and gas choice, have still to be defined and understood in order to give a detailed comparison of the performance of the GEM based prototype with respect to the T2K requirements. Data will therefore be taken in the next months to investigate different gas mixtures.

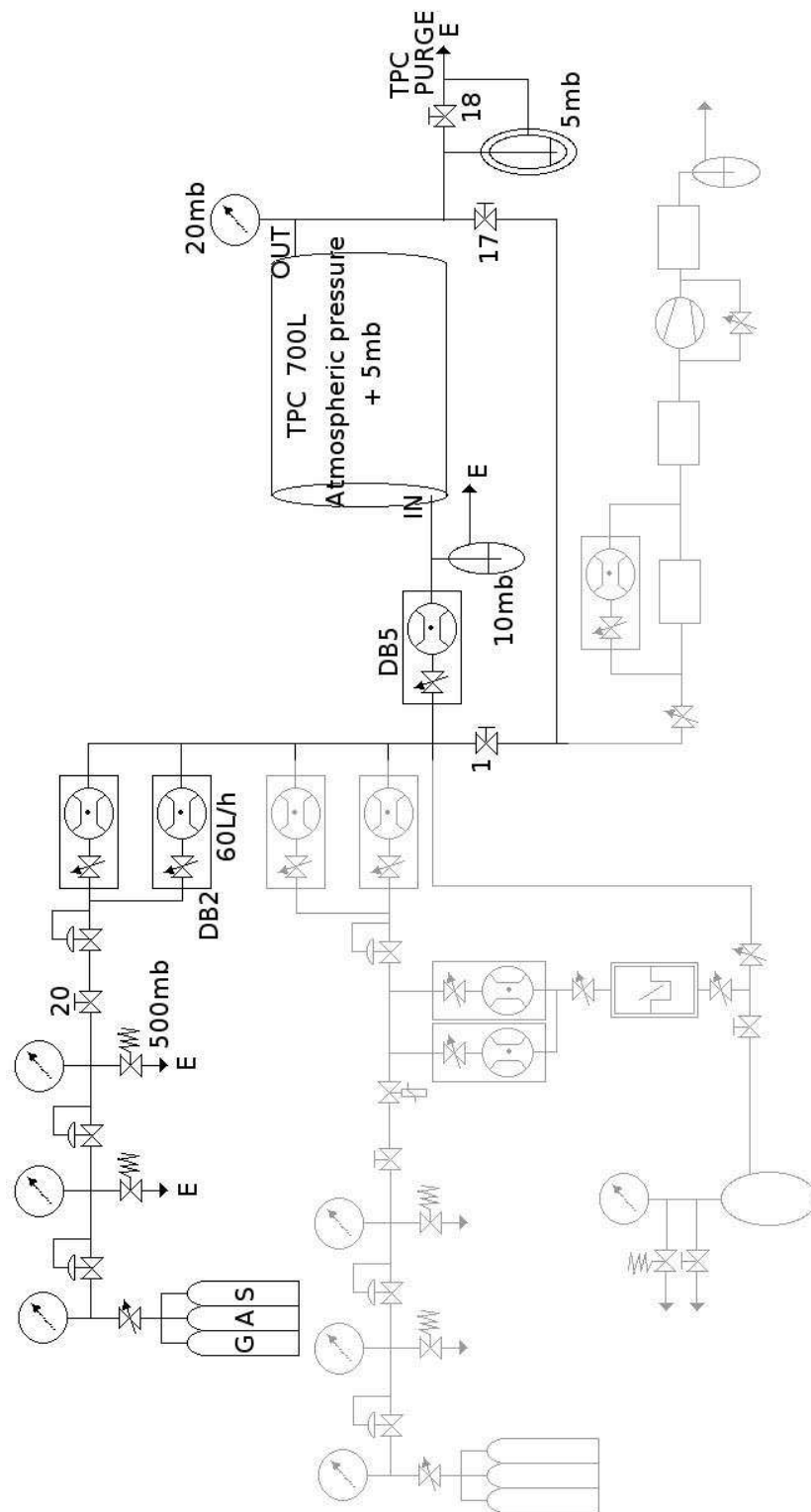
To conclude, it is important to stress again that the collaboration gained a lot of experience during this intense R&D period. Within this effort, we understood the different aspects of operating GEMs, and proposed and developed design concepts and GEM testing procedure that could be easily extrapolated to a large scale production. We are absolutely convinced that we could contribute actively to the construction and operation of the ND280m TPC detector based on GEMs.

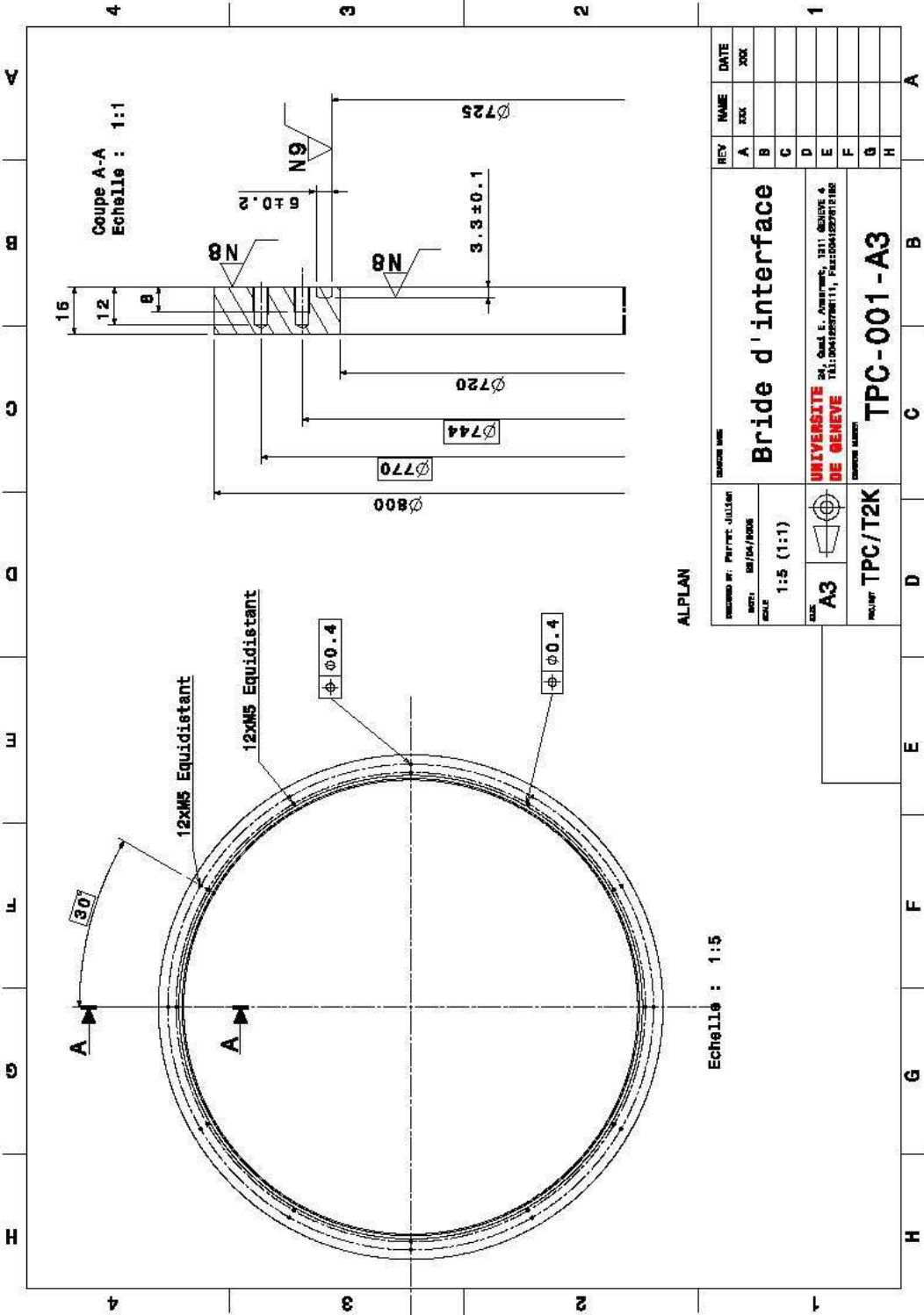
Appendix A

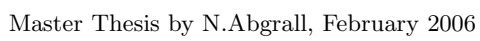
The TPC

A.1 The HARP Gas System

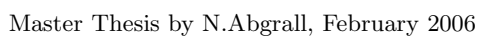
A.2 Technical Drawings













TETRABOARD**Proposal 9**

H. Pitch: 8.0 mm
 V. Pitch: 8.3 mm
 Gap: 0.25 mm
 Pads: 732

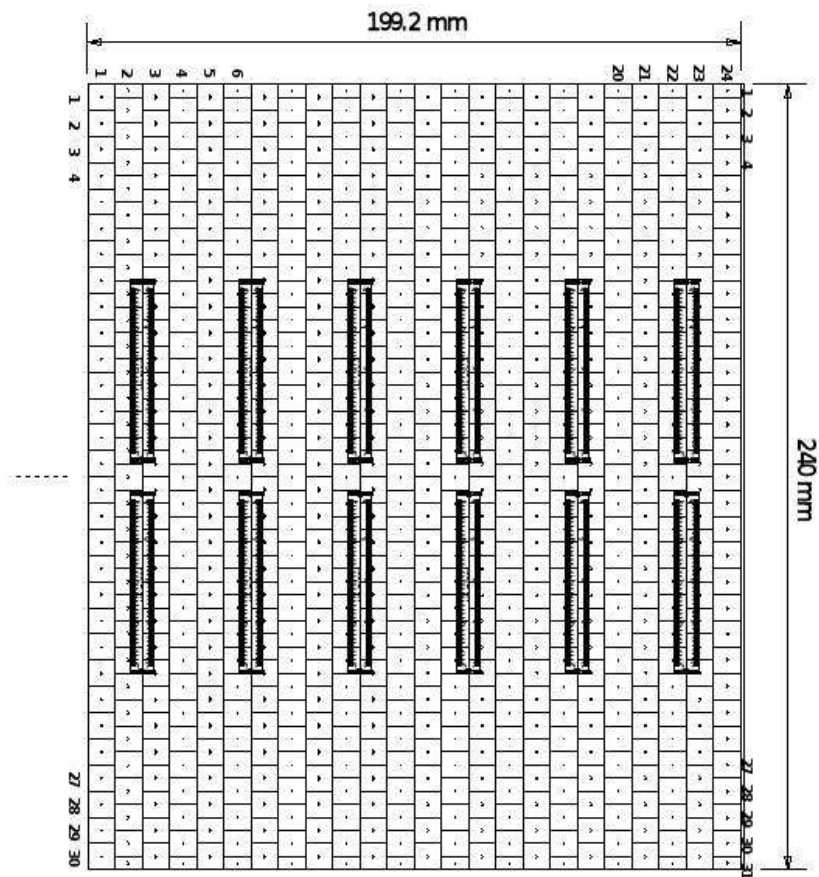


Figure A.7: Tetraboard.

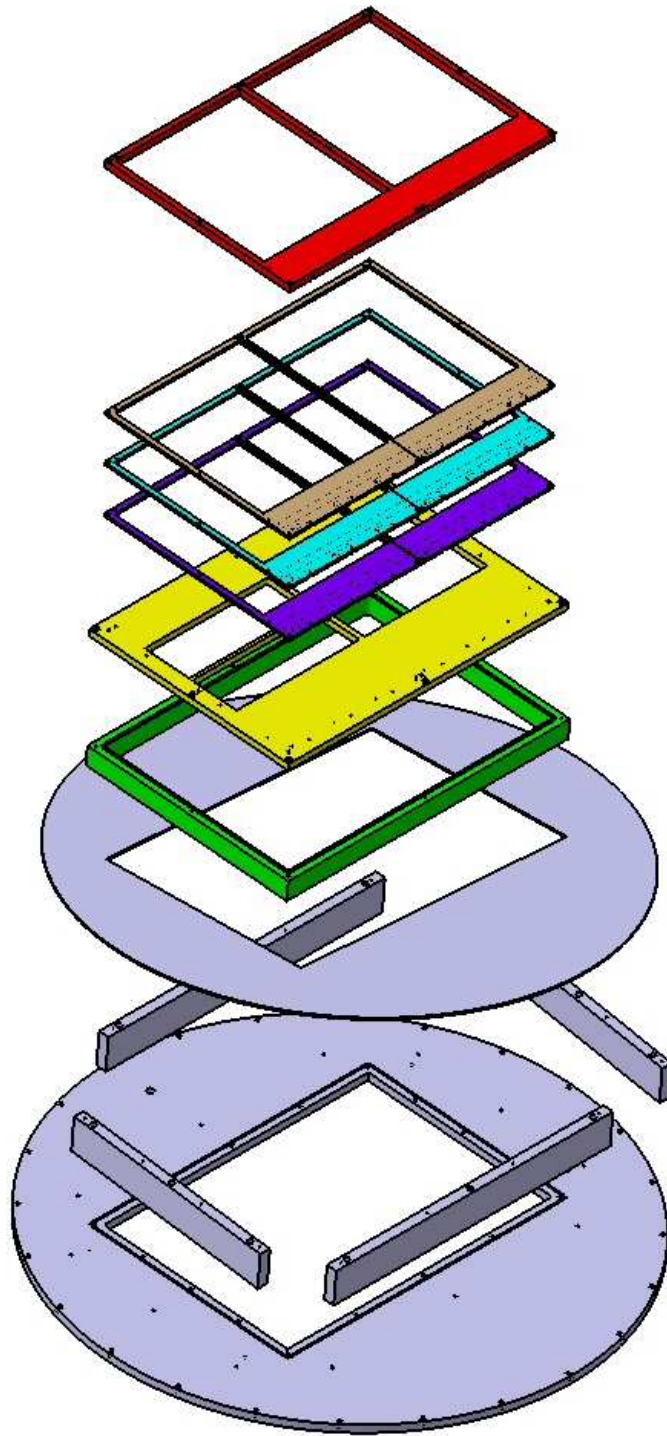


Figure A.8: Complete stacking.

Appendix B

The Electronics

B.1 Mapping File

ADC CARD				PAD PLANE				PROT CARD		INVERT CARD	
*****				*****				*****		*****	
card	-- chan	-- sector	-- row	-- pad	-- conn	-- pin	-- pin	conn	-- pin	conn	-- pin

TPC_MAPPING											
C	11	115	1	2	8	J16	A5	J1	A5	J2	5
C	11	114	1	2	7	J16	A6	J1	A6	J2	4
C	11	113	1	2	6	J16	A7	J1	A7	J2	10
C	11	118	1	2	9	J16	A8	J1	A8	J2	9
C	11	124	1	2	5	J16	A9	J1	A9	J2	15
C	11	125	1	2	4	J16	A10	J1	A10	J2	14
C	11	120	1	2	10	J16	A11	J1	A11	J2	20
C	11	121	9999	9999	9999	J16	A12	J1	A12	J2	19

C	11	107	1	2	3	J16	A13	J1	A13	J13	5
C	11	106	1	2	2	J16	A14	J1	A14	J13	4
C	11	111	1	2	1	J16	A15	J1	A15	J13	10
C	11	110	1	1	1	J16	A16	J1	A16	J13	9
C	11	100	1	2	11	J16	A17	J1	A17	J13	15
C	11	101	1	1	2	J16	A18	J1	A18	J13	14
C	11	96	1	1	3	J16	A19	J1	A19	J13	20
C	11	97	1	1	4	J16	A20	J1	A20	J13	19

C	11	83	1	1	5	J16	A21	J1	A21	J5	5
C	11	82	1	1	6	J16	A22	J1	A22	J5	4
C	11	87	1	2	12	J16	A23	J1	A23	J5	10
C	11	86	1	1	7	J16	A24	J1	A24	J5	9
C	11	92	1	1	8	J16	A25	J1	A25	J5	15
C	11	93	1	1	9	J16	A26	J1	A26	J5	14
C	11	88	1	1	10	J16	A27	J1	A27	J5	20
C	11	89	1	1	11	J16	A28	J1	A28	J5	19

C	11	75	1	1	12	J16	A29	J1	A29	J14	5
C	11	74	1	1	13	J16	A30	J1	A30	J14	4
C	11	79	1	1	13	J16	A31	J1	A31	J14	10
C	11	78	1	2	14	J16	A32	J1	A32	J14	9
C	11	68	1	1	14	J16	A33	J1	A33	J14	15
C	11	69	1	2	15	J16	A34	J1	A34	J14	14
C	11	64	1	1	15	J16	A35	J1	A35	J14	20
C	11	65	1	2	16	J16	A36	J1	A36	J14	19

C	11	113	1	3	8	J16	B5	J1	B5	J2	2
C	11	112	1	3	7	J16	B6	J1	B6	J2	1
C	11	117	1	3	6	J16	B7	J1	B7	J2	7
C	11	116	1	3	9	J16	B8	J1	B8	J2	6
C	11	126	1	3	5	J16	B9	J1	B9	J2	12
C	11	127	1	3	4	J16	B10	J1	B10	J2	11
C	11	122	1	3	10	J16	B11	J1	B11	J2	17
C	11	123	9999	9999	9999	J16	B12	J1	B12	J2	16

C	11	105	1	3	3	J16	B13	J1	B13	J13	2
C	11	104	1	3	2	J16	B14	J1	B14	J13	1
C	11	109	1	3	1	J16	B15	J1	B15	J13	7
C	11	108	1	4	1	J16	B16	J1	B16	J13	6
C	11	102	1	3	11	J16	B17	J1	B17	J13	12
C	11	103	1	4	2	J16	B18	J1	B18	J13	11
C	11	98	1	4	3	J16	B19	J1	B19	J13	17
C	11	99	1	4	4	J16	B20	J1	B20	J13	16

C	11	81	1	4	5	J16	B21	J1	B21	J5	2
C	11	80	1	4	6	J16	B22	J1	B22	J5	1
C	11	85	1	3	12	J16	B23	J1	B23	J5	7
C	11	84	1	4	7	J16	B24	J1	B24	J5	6
C	11	94	1	4	8	J16	B25	J1	B25	J5	12
C	11	95	1	4	9	J16	B26	J1	B26	J5	11
C	11	90	1	4	10	J16	B27	J1	B27	J5	17
C	11	91	1	4	11	J16	B28	J1	B28	J5	16

C	11	73	1	4	12	J16	B29	J1	B29	J14	2
C	11	72	1	4	13	J16	B30	J1	B30	J14	1
C	11	77	1	3	13	J16	B31	J1	B31	J14	7
C	11	76	1	4	14	J16	B32	J1	B32	J14	6
C	11	70	1	3	14	J16	B33	J1	B33	J14	12
C	11	71	1	4	15	J16	B34	J1	B34	J14	11
C	11	66	1	3	15	J16	B35	J1	B35	J14	17
C	11	67	1	4	16	J16	B36	J1	B36	J14	16

C	11	51	1	1	16	J15	A5	J2	A5	J7	5
C	11	50	1	2	17	J15	A6	J2	A6	J7	4
C	11	55	1	1	17	J15	A7	J2	A7	J7	10
C	11	54	1	2	18	J15	A8	J2	A8	J7	9
C	11	60	1	1	18	J15	A9	J2	A9	J7	15
C	11	61	1	1	19	J15	A10	J2	A10	J7	14
C	11	56	1	2	19	J15	A11	J2	A11	J7	20
C	11	57	1	1	20	J15	A12	J2	A12	J7	19

C	11	43	1	1	21	J15	A13	J2	A13	J15	5
C	11	42	1	1	22	J15	A14	J2	A14	J15	4
C	11	47	1	1	23	J15	A15	J2	A15	J15	10
C	11	46	1	1	24	J15	A16	J2	A16	J15	9
C	11	36	1	1	25	J15	A17	J2	A17	J15	15
C	11	37	1	1	26	J15	A18	J2	A18	J15	14
C	11	32	1	2	20	J15	A19	J2	A19	J15	20
C	11	33	1	1	27	J15	A20	J2	A20	J15	19

Figure B.1: Mapping file.

C	11	19	1	1	28	J15	A21	J2	A21	J10	5
C	11	18	1	1	29	J15	A22	J2	A22	J10	4
C	11	23	1	1	30	J15	A23	J2	A23	J10	10
C	11	22	1	2	21	J15	A24	J2	A24	J10	9
C	11	28	1	2	31	J15	A25	J2	A25	J10	15
C	11	29	1	2	30	J15	A26	J2	A26	J10	14
C	11	24	1	2	29	J15	A27	J2	A27	J10	20
C	11	25	9999	9999	9999	J15	A28	J2	A28	J10	19

C	11	11	9999	9999	9999	J15	A29	J2	A29	J16	5
C	11	10	1	2	22	J15	A30	J2	A30	J16	4
C	11	15	1	2	28	J15	A31	J2	A31	J16	10
C	11	14	1	2	27	J15	A32	J2	A32	J16	9
C	11	4	1	2	26	J15	A33	J2	A33	J16	15
C	11	5	1	2	25	J15	A34	J2	A34	J16	14
C	11	0	1	2	24	J15	A35	J2	A35	J16	20
C	11	1	1	2	23	J15	A36	J2	A36	J16	19

C	11	49	1	3	16	J15	B5	J2	B5	J7	2
C	11	48	1	3	17	J15	B6	J2	B6	J7	1
C	11	55	1	4	17	J15	B7	J2	B7	J7	7
C	11	52	1	3	18	J15	B8	J2	B8	J7	6
C	11	62	1	4	18	J15	B9	J2	B9	J7	12
C	11	63	1	4	19	J15	B10	J2	B10	J7	11
C	11	58	1	4	20	J15	B11	J2	B11	J7	17
C	11	59	1	4	21	J15	B12	J2	B12	J7	16

C	11	41	1	4	22	J15	B13	J2	B13	J15	2
C	11	40	1	4	23	J15	B14	J2	B14	J15	1
C	11	45	1	3	19	J15	B15	J2	B15	J15	7
C	11	44	1	4	24	J15	B16	J2	B16	J15	6
C	11	38	1	4	25	J15	B17	J2	B17	J15	12
C	11	39	1	4	26	J15	B18	J2	B18	J15	11
C	11	34	1	4	27	J15	B19	J2	B19	J15	17
C	11	35	1	4	28	J15	B20	J2	B20	J15	16

C	11	17	1	3	20	J15	B21	J2	B21	J10	2
C	11	16	1	4	29	J15	B22	J2	B22	J10	1
C	11	21	1	4	30	J15	B23	J2	B23	J10	7
C	11	20	1	4	31	J15	B24	J2	B24	J10	6
C	11	30	1	3	30	J15	B25	J2	B25	J10	12
C	11	31	1	3	29	J15	B26	J2	B26	J10	11
C	11	26	1	3	21	J15	B27	J2	B27	J10	17
C	11	27	9999	9999	9999	J15	B28	J2	B28	J10	16

C	11	9	9999	9999	9999	J15	B29	J2	B29	J16	2
C	11	8	1	3	28	J15	B30	J2	B30	J16	1
C	11	13	1	3	27	J15	B31	J2	B31	J16	7
C	11	12	1	3	26	J15	B32	J2	B32	J16	6
C	11	6	1	3	25	J15	B33	J2	B33	J16	12
C	11	7	1	3	24	J15	B34	J2	B34	J16	11
C	11	2	1	3	22	J15	B35	J2	B35	J16	17
C	11	3	1	3	23	J15	B36	J2	B36	J16	16

TPC_END											

Appendix C

Analysis

C.1 The Likelihood Function

The multinomial distribution is the generalisation of the binomial distribution in the case where there are more than 2 possible outcomes. The standard example is the distribution of N independent events in an histogramme. If p_i represents the probability that an individual event is in the i th bin of the histogramme, then the probability to get r_i events in the i th bin for each i is given by:

$$p(r_1, \dots, r_n) = \frac{N!}{r_1! \dots r_n!} p_1^{r_1} \dots p_n^{r_n} \quad (\text{C.1})$$

The expected value, variance and correlation coefficients are given by:

$$\begin{cases} E(r_i) = Np_i \\ V(r_i) = Np_i(1 - p_i) \\ \rho_{ij} = -\sqrt{p_i p_j (1 - p_i)(1 - p_j)} \end{cases}$$

where the correlation coefficient result from the normalisation relations, $\sum_{i=1}^n p_i = 1$ and $\sum_{i=1}^n r_i = N$. In the case where the primary number of electrons n_i (that is the collected number of electrons over the gain N_i/g) associated to pad i is not too large, the likelihood for observing a given serie of charges in a respective serie of pads can be expressed by the multinomial distribution:

$$\mathcal{L} = C \prod_{i=1}^k p_i^{n_i} \quad (\text{C.2})$$

where C is just the combination constant that depends on data only, k is the number of pads, and p_i is the probability that n_i primary electrons are collected in pad i . The sum actually runs over $k-1$ pads since the k th term is fixed by the normalisation as

$$\left(1 - \sum_{i=1}^{k-1} p_i\right)^{N - \sum_{i=1}^{k-1} n_i} \quad (\text{C.3})$$

The log-likelihood function per row is then given by

$$\log \mathcal{L}_{row} = \sum_{i=1}^k n_i \log p_i + \log C \quad (\text{C.4})$$

where

$$p_i = I(b_i, \phi_i, \sigma, h_i, w_i) / \sum_j I(b_j, \phi_j, \sigma, h_j, w_j) \quad (\text{C.5})$$

Bibliography

- [1] Particle Data Group. Particle physics booklet, July 2004.
- [2] Gabriel Vidal Sitjes. The harp time projection chamber. Master's thesis, Universidad de Valencia, 2003.
- [3] T2K-TPC Group. T2k tpc feasibility report. Technical report, December 2004. T2K-TPC Note-001.
- [4] T2K Collaboration. T2k nd280 conceptual design report. Technical report, September 2005. DRAFT: Version 1.0.
- [5] W.R.Leo. *Techniques for Nuclear and Particle Physics Experiments*. Springer-Verlag, 2 edition, 1994.
- [6] S.Bachmann, A.Bressan, L.Ropelewski, F.Sauli, A.Sharma, and D.Moermann. Charge amplification and transfer processes in the gas electron multiplier. *Nuclear Instruments & Methods in Physics Research, Section A*, A 438:376–408, June 1999.
- [7] M.Killenberg, S.Lotze, J.Mnich, S.Roth, R.Schulte, B.Sobloher, W.Struczinski, and M.Tonutti. Modelling and measurement of charge transfer in multiple gem structures. *Nuclear Instruments & Methods in Physics Research, Section A*, A 489:369–383, December 2002.
- [8] S.Lotze RWTH Aachen. Ladungstransfer von gem-strukturen in hohem magnetfeldern. Graduiertenseminar, September 2004.
- [9] S.Lotze. Aufbau eines teststandes und messungen zum betrieB einer tpc mit gems. Master's thesis, RWTH Aachen, 2001. available at <http://www.physik.rwth-aachen.de/group/IIIphys/TESLA/>.
- [10] B.Mota, J.Baechler, R.Bramm, R.Campagnolo, R.E.Bosch, A.Jiménez de Parga, and L.Musa. Performance of the altro chip on data acquired on a alice tpc prototype. *Nuclear Instruments & Methods in Physics Research, Section A*, A 535:500–505, August 2004.
- [11] CERN-PH/ED. *ALICE TPC Readout Chip, User Manual*, June 2002. Draft 0.2.
- [12] M.Capeans, B.Ketzer, A.Placci, L.Ropelewski, F.Sauli, and M.van Stenis. Construction of gem detectors for the compass experiment-production guide. Technical note TA1/00-03, December 2001.
- [13] E.Radicioni INFN-Sezione di Bari/Italy. Design considerations on a tpc for t2k-nd280m. Technical report, December 2004. T2K-TPC Note-002.
- [14] H.Kuroiwa and al. The influence of oxygen contamination on the performance of a mini-jet-cell-type drift chamber for the jlc-cdc. KEK-PREPRINT-2003-41.

- [15] D.Karlen, P.Poffenberger, and G.Rosenbaum. Tpc performance in magnetic fields with gem and pad readout. *Nuclear Instruments & Methods in Physics Research, Section A*, A 555:80–92, September 2005.
- [16] D.Karlen University of Victoria and TRIUMF. Study of momentum resolution in the t2k tpc with full simulations. Technical report, March 2005. T2K-TPC Note-003.
- [17] Rabindra N.Mohapatra and Palsh B.Pal. *Massive Neutrinos in Physics and Astrophysics*. World Scientific, 2 edition, 2004.
- [18] F.Sánchez UAB/IFAE. Motivations for a nd280m tpc. Presentation of the T2K Collaboration Meeting at KEK, Japan, January 2006.
- [19] O.Bouianov, M.Bouianov, R.Orava, P.Semenov, and V.Tikhonov. Progress in gem simulation. *Nuclear Instruments & Methods in Physics Research, Section A*, A 450:277–287, January 2000.
- [20] V.Tikhonov and R.Veenhof. Gem simulation methods development. *Nuclear Instruments & Methods in Physics Research, Section A*, A 478:452–459, 2002.
- [21] F.Sauli. Gem: A new concept for electron amplification in gas detectors. *Nuclear Instruments & Methods in Physics Research, Section A*, A 386:531–534, November 1996.
- [22] F.Sauli. Gas electron multiplier detectors. LBL TPC Workshop-Berkeley, October 2003.
- [23] R.Bramm. Altro and tpc performance of alice. Dissertation Draft, 2005.
- [24] R.Campagnolo, J.Baechler, R.Bramm, C.Engster, R.E.Bosch, C.Gonzales Gutierrez, A.Jiménez de Parga, A.Junique, B.Mota, and L.Musa. Performance of the alice tpc front end card. Amsterdam, September 2003. ninth Workshop on Electronics for LHC Experiments.
- [25] R.Campagnolo. The alice tpc readout bus-status report. available at <http://cern.ch/ep-ed-alice-tpc/>, December 2001.
- [26] H. Boutamine, R. Campagnolo, C. Gonzalez, M. Joos, A. Junique, B. Mota, and L.Musa. *U2F 1.1, USB to FEC interface card, User Manual*. CERN-PH/ED, March 2004. Draft 1.3.
- [27] Lara Howlett. *Simulation and Correction of Crosstalk in the HARP Time Projection Chamber*. PhD thesis, University Sheffield, 2004.
- [28] Alexander Grossheim. *Particle Production Yields induced by Multi-GeV protons on Nuclear Targets*. PhD thesis, University of Dortmund, 2003.